Some Aspects of Hadron Hadron Collisions in High Energy Interactions (B_s^0 mixing oscillations in semileptonic decay at DØ Experiment)

THESIS SUBMITTED TO THE UNIVERSITY OF DELHI
FOR THE DEGREE OF

DOCTOR OF PHILOSOPHY

MD. NAIMUDDIN

SUPERVISOR: PROF. R. K. SHIVPURI
PROF. D. S. KULSHRESHTHA

DEPARTMENT OF PHYSICS & ASTROPHYSICS
UNIVERSITY OF DELHI
DELHI 110 007
INDIA

2006

Dedicated To

My Parents and family of which I am an integral part & to my late brother-in-law Md. Shaifuzzama whom we all miss

ACKNOWLEDGMENTS

I never thought that one day I would be writing these acknowledgments as part of my dissertation. Being from a small place and rural background I hardly ever imagined that some day I would be working in one of the best lab and with best minds in the world and that I would be scratching my head to find the answers to the most fundamental questions that we have in front of us today.

And the one person who got me into this business is my mentor, teacher and supervisor Prof. R. K. Shivpuri. I wish to express my heartfelt thanks to him. At each and every stage of my M.Sc. days he always encouraged and motivated me to join the research and he was always there to help me out with any problem. I learned the basics of high energy and nuclear physics from him. I was really impressed by his deep understandings of the subject and his magnificent style of teaching. His way of explaining the most difficult and complicated things in simple and lucid way surprises everyone. There used to have a Que of students in front of his office to get a chance to work in his lab and I consider myself lucky that I got the opportunity to work with him. I have seen very few people who work so selflessly and always think best for his students. I seldom have seen the parallels of the magnanimous character that he possesses. I am inspired by his tremendous energy, patience and utmost care for his students. And above all he is a marvelous human being and a great soul. I share a special relationship and a great bond of trust with him. I am also grateful to him for reading and correcting my thesis.

I would also like to express my sincere thanks to my thesis adviser Prof. D. S. Kulshreshtha. Without his help and support this thesis would not have completed. He is the person from whom I have always learned something new. His relationship with me is more than that of teacher and a student. I do not find the words to thank him as it is simply impossible to return his favors in thanks. Good times, bad times he was always a call away and has patience to listen to my complicated problems and then to solve them. It was a privilege and pleasure to work with him as he has given me the complete freedom to do my research. I had even the privilege to disturb him at his home whenever I needed him. I consider myself fortunate to have him as my supervisor.

I wish to express my special thanks to the Head of the Department of Physics, Prof. M. P. Srivastava for providing the necessary facilities in the department. I met and worked with many wonderful people during my stay at Fermilab. It would not be possible to thank everyone of them individually here and I just wish that I could reciprocate whatever I earned from them.

First and foremost my sincere thanks to my local supervisor at Fermilab, Dr. Gene Fisk. He is one person who never let me felt away from home. From the first day, he took care of all my needs and always motivated me to work hard and excel in life. It was his motivation and unconditional support that I was able to contribute whatever little I could in so less time. Despite being incredibly busy, the doors of his office was always open to me and I had the privilege to bother him anytime. He always has time to listen to my problems and trying to find the solutions. I greatly benefited from the long discussions we used to have on my analysis, detector, etc. I am really fortunate that I found Gene as my local supervisor at Fermilab. Thanks a lot Gene for all your help and personal care.

The other person who was not less than my supervisor at DØ is Prof. Jerry Blazey. He always encouraged and motivated me to take the challenges and got me involved in the interesting and right projects. It was his personal care that I got a chance to work on hardware and software projects along with my physics analysis which helped me develop myself as a complete high energy physicists. Thank you very much Jerry for all your guidance and care and for reading the proofs of my thesis and correcting the same despite being incredibly busy those days.

I also consider myself fortunate to have Prof. Brajesh Choudhary as my local guardian during my stay at Fermilab. His support, help and care for me was invaluable. I remember how worried he was when I had to go for the US visa and how happy he felt when I got it. I share a great relationship with him and he is more like an elder brother and a friend. Thank you very much sir for all your help and care all along these years and for the long discussions we used to have on variety of topics.

I would also like to thank Prof. Feroz Ahmed for his guidance and support during the troubled days and always encouraging me to do best in life. A special thanks to Prof. Brad Abbott for working with me all along my stay at Fermilab and guiding me through my analysis and always taking care of my interests. I would also like to thanks Vivek Jain who encouraged me to work on B_s^0 mixing and also for motivating me to work on the development of electron tagging. Many thanks to B physics group conveners Brendan Casey and Guennadi Borissov for working with me on mass fitting and always encouraging me to get the results and present in the meetings. I always used to turn to Brendan for basic B physics questions and to clear my doubts. Working with Guennadi was a wonderful and enriching experience for me. He is full of new ideas and tremendous energy. I also owe lot of thanks to the previous B Physics convener Rick Van Kooten for providing me the opportunity, freedom and infrastructure in the group to carry out my analysis. My sincere thanks to Mixing

convener Sergey Burdin for his help throughout the mixing analysis. I would also like to thank Tania Moulik for working with me on electron tagging and helping me out with the softwares during my initial days at DØ. I am grateful to Prof. Terry Wyatt for his continuous support and motivation in all my work.

I am very thankful to Hal Evans and Nikos Varelas for supporting and encouraging me during my stunt with L1 calorimeter upgrade project. I really enjoyed and learned a lot while working on l1cal upgrade. I am thankful to Mike Mulhearn and Sabine Lammers for providing a wonderful and stimulating environment during l1cal work and for the extraordinary understanding we had in carrying out our task so efficiently and also for assisting me in my testings of the systems even in the middle of night or in the early morning. I am also thankful to Darien Wood and George Ginther for their encouraging words because of which we could finish our l1cal work in time. Thanks also to Alan Stone, Lyn Bagby, Dan Edmonds, Dean Schamberger and Todd Adams for the useful discussions we had on various l1cal issues.

I would also like to thank my Global Monitoring colleagues who always helped me running the GM efficiently. A lot of thanks to Elliott Cheu for sharing the responsibility of GM with me. Thanks also to Michiel Sanders for helping me get acquainted with the GM tools. I also owe thanks to Matthew Ford and Dennis Mackin for helping me in keeping GM running without problems. I would also like to thank DØ run coordinators Bill Lee and Taka Yasuda for their cooperation in proper running of GM.

A big thanks to my Delhi colleagues Kirti and Ashish for a wonderful and memorable time we had during our stay at Delhi House. For their consistent encouragement and support in all my endeavors and for never letting me feel bored and away from home. And also for the useful and stimulating physics discussions we used to have in our leisure time.

I owe a lot of thanks to my friend and colleague Burair for getting me acquainted with the DØ data structure during my initial days and helping me whenever I had any problem with my Linux box. And also for the long overnight discussions we had on physics and beyond which sometimes used to end only with the beginning of the day. I am also thankful to B physics colleagues and friends Cano and Dan for working with me on mixing and the useful discussions we used to have on the various analysis issues. Thanks to my friend Ralf for the wonderful time we had at Moriond and for taking care of my Monte Carlo samples. I would also like to express my thanks to my B physics colleagues Rick jesik, Alberto, Dmitri and others for the useful discussions.

I would also like to thank Shekhar and Tanuja Mishra for the continuous en-

couragement and the wonderful dinners. Thanks also to Vishnu Zutshi and family, Mrinmoy and Barnali, Harpareet and Geeti and Shailesh and Vandana for their invitations for dinners, meaningful discussions and classical jokes.

Many thanks to Mr. P.C. Gupta ji for his consistent support and care. He is a great soul with extraordinary conviction and utmost humility. Thanks to my Delhi Colleagues Ashutosh Bhardwaj, Namrata, Sudeep, Manoj, Ajay, Ashutosh Srivastava, Sushil and Pooja for a wonderful time and company during my Delhi days. Thanks also to Mr. G.D. Sharma, Rajendra, Yunus and Dinesh for their continuous assistance.

Many thanks to my friends at DØ Avdhesh, Venkat, Tulika, Wade, Miruna, Peter, Piyali, Jyotsana, Supriya, Subhendu, Prolay and Miroslav. Thanks also to Ariel, Christos, Peier Petroff, Laurent Duflot for helping me out in need. A special thanks to Jan Stark for taking interest in my electron tagging analysis and for helping me with em-ID and softwares and for the stimulating and long discussions we had on variety of physics and detector issues.

I am also thankful to my old friends Ehtesham, Nadeem, Hema, Pradeep, Kopal, Pranav, Arijeet, Raksha, Hemant, Ravi, Mrinal, Noor Rahman, Riyaz, Ashraf, Asad, Farhat and Riyaz Hashmi for their continuous love and support.

I would also like to thank Council of Scientific and Industrial Research (CSIR), Govt. of India for the financial support. Thanks also to Universities Research Association (Fermilab) for their support during my stay at Fermilab.

And finally I would like to express my gratitude to my parents and family who were always with me in my bad and good times and for their unconditional love. They are the source of inspiration and the reason for me to do good in life. My Abba being raised in difficult times and having spent most of his life in hardship has never let me felt the hardships and did everything to help me achieve my goals. My Amma always wanted me to go for higher studies and inculcated in me whatever good values I possess. My parents are my ideals and I am nothing without them. Even If I adopt half the good values they possesses I would consider my life to be successful. I would also like to thank my elder sister for her continuous prayers and utmost support and love for me. I thank to my other sisters, brothers and nieces for all the support and happiness they provided me during these years.

MD. NAIMUDDIN

LIST OF PUBLICATIONS

1. "*Direct Limits on the B_s^0 Oscillation Frequency*", DØ Collaboration (V. M. Abazov, ..., Md. Naimuddin, et. al.), **Phys. Rev. Lett. 97, 021802 (2005)**.

2. "*Study of B_s^0 Mixing at the Tevatron*", Md. Naimuddin, **Proceedings of** 41^{st} **Moriond QCD Conference (2006), hep/ex-0605057**.

Conference & DØ Notes

1. "*B-Flavor Tagging with Soft electrons*", Md. Naimuddin et. al., DØ Note 4713 (2005).

2. "*B_d Mixing measurement using semileptonic sample and combined opposite side tagging*", G. Borrisov, ..., Md. Naimuddin, et al., DØ Note 4828 (2005), Submitted to PRD.

3. "*B_s^0 mixing in semileptonic B_s decays using $D_s^- \to \phi\pi^-$ decay mode*", C. Ay, ..., Md. Naimuddin, et. al., DØ Note 4842 (2005).

4. "*B-Flavor tagging with opposite-side soft electrons*", Md. Naimuddin et al., DØ Note 4848, (2005) (**Conference Note for 2005 Summer Conferences**).

5. "*Study of Trilepton triggers*", Md. Naimuddin et al., DØ Note 4849 (2005).

6. "*A search for B_s^0 oscillations at DØ using $B_s^0 \to D_s^-\mu^+X$ ($D_s^- \to K^{*0}K^-$)*" C. Ay, ..., Md. Naimuddin, et. al. DØ Note 4863 (2005).

7. "*Combined Opposite-side Flavor Tagging*", C. Ay, ..., Md. Naimuddin, et. al., DØ Note 4875 (2005) (**Conference Note for 2005 Summer Conferences**).

8. "*A search for B_s^0 oscillations at DØ using $B_s^0 \to D_s^-\mu^+X$ ($D_s^- \to K^{*0}K^-$)* ", C. Ay, ..., Md. Naimuddin, et. al., DØ Note 4878 (2005) (**Conference Note for 2005 Summer Conferences**).

9. "*Mixing in the B_s^0 System Using $B_s^0 \to D_s^-\mu^+X$, $D_s^- \to \phi\pi^-$ decay mode and opposite side flavor tagging*", C. Ay, ..., Md. Naimuddin, et al., DØ Note 4881 (2005) (**Conference Note for 2005 Summer Conferences**).

10. "*B_s^0 Mixing measurement at DØ Using $B_s^0 \to D_s^-\mu^+X$ ($D_s^- \to K^{*0}K^-$)*", B. Abbott, ..., Md. Naimuddin, et al., DØ Note 5015 (2006).

11. "*Global Monitoring at DØ*", Md. Naimuddin et. al., DØ Note 5141 (2006).

12. "B_s^0 *mixing studies in Semileptonic* B_s^0 *decays with* $D_s^- \to K^{*0}K^-$ *and Unbinned fit*", B. Abbott, ..., Md. Naimuddin, et. al., DØ Note 5149 (2006)

13. "B_s^0 *mixing studies in Semileptonic* B_s^0 *decays with* $D_s^- \to K^{*0}K^-$ *and Unbinned fit*", B. Abbott, ..., Md. Naimuddin, et. al., DØ Note 5172 (2006) (**Conference Note for 2006 Summer Conferences**).

14. "*A combination of* B_s^0 *Oscillations Results from DØ*", G. Borrisov, ..., Md. Naimuddin, et. al., DØ Note 5207 (2006) (**Conference Note for 2006 Summer Conferences**).

Contents

List of Figures

List of Tables

Chapter 1

Introduction

From the very beginning of their existence, human beings have tried to understand and explore the things surrounding them. This is the unique feature of human beings which makes them an altogether completely different and superior species. In order to understand any natural phenomenon, a systematic study is needed. As an example, If we are trying to understand the cause of a certain problem in the human body then a systematic study of the human body is required. Similarly if we are trying to understand the nature and surroundings around us then we need to explore it right at its roots. This is what we do at a high energy physics lab like Fermilab. Aided with big machines and state of the art technology we try to understand fundamental questions: How did the Universe came to its present form. What happened at the time of Big Bang. Where has all the anti-matter has gone.

The concept of a 'particle' is a natural idealization of our everyday observation of matter. Dust particles or baseballs, under ordinary conditions, are stable objects that move as a whole and obey simple laws of motion. However, neither of these is actually a structureless object. That is, if sufficiently large forces are applied to them, they can readily be broken into smaller pieces. The idea that there must be some set of smallest constituent parts, which are the building blocks of all matter, is a very old one. In the 1930s, it seemed that protons, neutrons, and electrons were the smallest objects into

which matter could be divided and they were termed "elementary particles". The word elementary then meant "having no smaller constituent parts", or "indivisible" – the new "atoms", in the original sense.

Again, later knowledge changed our understanding as physicists discovered yet another layer of structure within the protons and neutrons. It is now known that protons and neutrons are made of quarks. Over 100 other "elementary" particles were discovered between 1930 and the present time. These elementary particles are all made from quarks and/or antiquarks.

Once quarks were discovered, it was clear that all these so called "elementary particles" particles were no longer elementary but were composite objects. Leptons, on the other hand, still appear to be structureless. Today, quarks and leptons, and their antiparticles, are the natural candidates for the fundamental building blocks from which all else is made. Particle physicists call them the "fundamental" or "elementary" particles – both names denoting that, as far as current experiments can tell, they have no substructure.

Elementary particle physics

There are four kinds of forces in nature, strong, weak, electromagnetic and gravitational. Elementary particle physics is governed by the strong, weak and electromagnetic forces. The important numbers for comparing these three forces are called coupling constants, whose value measures the strength of the respective force. For electromagnetism, the coupling constant is called the fine structure constant α_{EM} and is formed by the electron charge, Planck's constant and the speed of light. For example α_{EM} can be obtained as,

$$\alpha_{EM} = \frac{e^2}{\hbar c} = \frac{1}{137.04} = 7.3 \times 10^{-3} \tag{1.1}$$

Notice this constant ends up being just a plain number. That is what is meant by

a dimensionless coupling constant. The combination of Planck's constant with the speed of light and the electron charge reveals something about the quantum relativistic physics of electromagnetism, that is, it tells us something about electromagnetism at distance scales where quantum mechanics and special relativity are both important. There are also dimensionless coupling constants for the strong and weak nuclear interactions. The table below compares their relative strengths and ranges.

Table 1.1: Different forces and their relative strengths.

Force	Symbol	Strength	Range
Strong nuclear force	α_s	$1/3$	10^{-15} m
Weak nuclear force	α_W	$1/30$	10^{-16} m
Electromagnetic force	α_{EM}	7×10^{-3}	∞

The weak nuclear force isn't actually that weak when measured by α_W, but it has the shortest range, because the gauge bosons are very heavy and have short lifetimes, so they can't travel very far without decaying into lighter particles. The strong nuclear force binds quarks into neutrons, protons and other hadrons, and binds protons and neutrons into the nuclei of atoms, but because of quark confinement, the strong force has a very small range as well. At the DØ experiment at Fermilab, we are trying to understand the behavior of these elementary particles and the forces acting between them.

In this thesis, we report the study on one such particle called the B_s^0 meson made up of a bottom and a strange quark. B_s^0 mesons are currently produced in a great numbers only at the Tevatron and we report a study done to measure the mixing parameter Δm_s between the B_s^0 meson and its anti-particle $\overline{B}_s^0$. Mixing is the ability of a very few neutral mesons to change from their particle to their antiparticle and vice versa. Until recently there existed only a lower limit on this measurement, here we report an upper bound and a most probable value for the mixing parameter. In the following chapter, we discuss the theoretical motivation behind this study. The measurement technique and the different factors that effect the measurement are

also given. In Chapter 3, we provide an overview of the experimental setup needed to perform the study. In Chapter 4, we present a new initial state flavor tagging algorithm using electrons and measurement of the B_d^0 mixing parameter Δm_d with the new technique. Details of the combined initial state tagging used in the B_s^0 mixing study are also given. A detailed description of the B_s^0 mixing analysis and the results are covered in Chapter 5. And finally the results from all the three channels and a bound on the mixing parameter are presented in Chapter 6.

Chapter 2

Theoretical Overview

2.1 The Standard Model

The Standard Model is a theory that explains physical phenomena with quite remarkable precision. It is the only theory to date which explains almost all the physical phenomena that we observe at the quantum level. It is a simple and comprehensive theory that explains all the hundreds of particles and complex interactions among the fundamental particles. Experiments have verified predictions to incredible precision, and almost all the particles predicted by this theory have been found. But it does not explain everything. For example, gravity is not included in the Standard Model.

According to the Standard Model, elementary particles can be grouped into two classes: bosons (particles that transmit forces) and fermions (particles that make up matter). The bosons have particle spin that is either 0, 1 or 2. The fermions have spin 1/2. Table 2.1 lists the elementary particles in the Standard Model that transmit the four forces observed in Nature [1]. The graviton isn't technically part of the Standard Model and has not been observed. The Standard Model is from a technical standpoint incompatible with gravity, and that's one reason string theory became an active field of theoretical physics.

When we say that quarks and gluons are observed "indirectly", we mean that

evidence of their existence inside hadrons exists but these particles have not been observed singly. In the theory of quarks and gluons, they are believed to be confined inside hadrons and unobservable as single particles, except possibly at extremely high temperatures (or energies) such as could be found very early in the Big Bang.

Table 2.1: Particles that transmit forces.

Name	Spin	Electric charge	Mass	Observed?
Graviton	2	0	0	Not yet
Photon	1	0	0	Yes
Gluon	1	0	0	Indirectly
W+	1	+1	80 GeV	Yes
W-	1	-1	80 GeV	Yes
Z0	1	0	91 GeV	Yes
Higgs	0	0	$> 114\ GeV$	Not yet

In the Standard Model, fermions are particles that make up matter, seem to be grouped into three generations. Notice in Table 2.2 that the quarks with charge 2/3 come in a group of three, as do the quarks with charge -1/3, as do the electron, muon and tau, and the electron, muon and tau neutrinos. Theoretical physics has not explained why there are three generations of particles.

Table 2.2: Particles that make up matter.

Name	Spin	Electric charge	Mass	Observed?
Electron	1/2	-1	0.0005 GeV	Yes
Muon	1/2	-1	0.10 Gev	Yes
Tau	1/2	-1	1.8 Gev	Yes
Electron neutrino	1/2	0	0?	Yes
Muon neutrino	1/2	0	$< .00017\ GeV$	Yes
Tau neutrino	1/2	0	$< .017\ GeV$	Yes
Up quark	1/2	2/3	0.005 GeV	Indirectly
Charm quark	1/2	2/3	1.4 GeV	Indirectly
Top quark	1/2	2/3	174 GeV	Indirectly
Down quark	1/2	-1/3	0.009 GeV	Indirectly
Strange quark	1/2	-1/3	0.17 GeV	Indirectly
Bottom quark	1/2	-1/3	4.4 GeV	Indirectly

We know of four fundamental forces in the universe: gravitational, electromag-

netic, weak and strong. Forces in gauge theories [2, 3] arise from certain *local* symmetry invariances in the Lagrangian, and are each proportional to a constant, or "charge". In the electromagnetic interaction, this is the usual Coulomb electric charge, whereas in the strong interaction it is called "color". Each quark carries one of three colors, conventionally called "red", "green", "blue". Quantum Chromodynamics (QCD) and the Electroweak Theory (EWK), which unifies the electromagnetic and the weak interactions, constitute the Standard Model of particle interactions. The remaining force is gravity, which is mediated by the *graviton*. The gravitation is described by the classical general theory of relativity [4] and, at present, there is no quantum version. However, since gravity is much weaker than all the other three forces, it can be ignored in high energy experiments.

2.1.1 The Electroweak Theory

Electroweak theory is a unified field theory that describes two of the fundamental forces of nature, electromagnetism and the weak interaction. In the Standard Model, electroweak interactions are described by a local gauge theory based on the $SU(2)_L \times U(1)_Y$ symmetry group, with four interaction mediators, or gauge bosons: the photon, W^-, W^+ and Z boson. Quarks and leptons, which transform as specific representations under $SU(2)_L$, are mass-ordered into three generations of two particles each. The bottom and top quark belong to the most massive quark generation.

2.1.2 The b Quark

The b quark, also referred to as the "beauty" or "bottom" quark is the second heaviest quark among the six quarks. It was discovered in 1977 at Fermilab, in a fixed target experiment [5]. The experiment showed an enhancement in the rate of $\mu^+\mu^-$ pair production with an invariant mass $\sim 9.5\ GeV/c^2$ which was interpreted as a $b\overline{b}$ bound state called ψ, now known to be the first of a family of the bottonium $b\overline{b}$ bound states,

the strong force analog of the electromagnetically bound positronium.

2.1.3 $b\overline{b}$ Production Mechanism

The b quarks in $p\overline{p}$ collisions are produced predominantly in pairs, as a result of the strong interaction between one parton from proton and another from anti-proton. The cross section for producing a b quark in a $p\overline{p}$ collision is calculated by convoluting the perturbative parton cross section with the proton distribution functions:

$$\frac{d^2\sigma}{dp_T d\eta}(p\overline{p} \to bX) = \sum_{ij} \int dx_i dx_j f_i^p(x_{i,\mu_F}) f_i^{\overline{p}}(x_{j,\mu_F}) \frac{d^2\sigma(ij \to bX, \mu_F)}{dp_T d\eta} \qquad (2.1)$$

where i and j are the incoming partons, $f_{i,j}^{p,\overline{p}}$ the proton and anti-proton parton distribution functions (PDFs), and $d^2\sigma(ij \to bX, \mu_F)/dp_T d\eta$ is the parton-level cross section for the $ij \to bX$ process. The cross section is calculated perturbatively in powers of the strong coupling constant $\alpha_s(\mu_R)$ at renormalization and factorization scales μ_R and μ_F, usually chosen of the order of the energy scale of the event. Figure 2.1 shows the leading order (LO) Feynman diagram for $b\overline{b}$ pair production and Fig 2.2 illustrates some of the processes entering the next-to-leading order (NLO) QCD calculations.

The contribution to the total $b\overline{b}$ cross section from higher order production mechanisms is comparable to that of direct production. This can be qualitatively understood because, for instance, the $gg \to gg$ cross section is about a factor 100 larger than $gg \to b\overline{b}$, and the rate of gluon splitting to bottom quarks ($g \to b\overline{b}$) is proportional to α_s, which is of the order of 0.1. The gluon-gluon initial states dominate the $b\overline{b}$ production cross section since the gluon PDF is higher than the quark PDF at low momentum fractions. In hadron colliders, the $b\overline{b}$ production mechanism have been traditionally grouped into three categories: direct production, flavor excitation, and gluon splitting. In perturbation theory, the three processes are not independent due

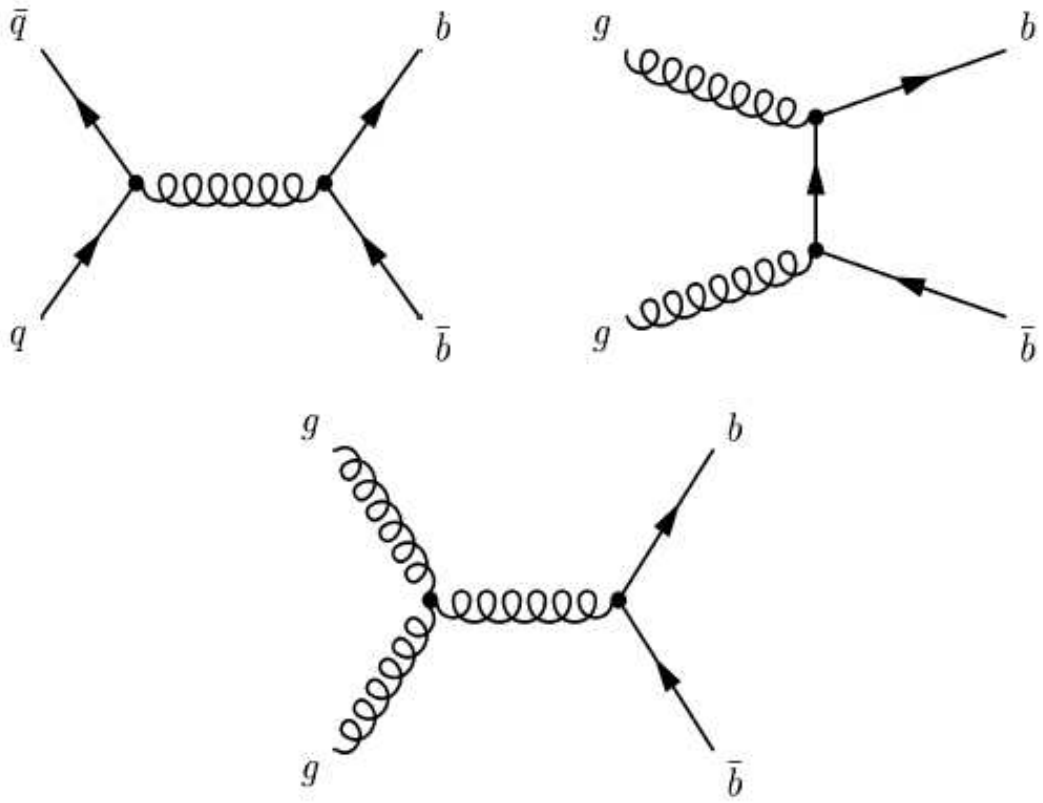

Figure 2.1: Leading order diagrams for $b\overline{b}$ production.

to interference between them. At next-to-leading order, direct production is basically a $2 \rightarrow 2$ parton subprocess with the addition of gluon radiation in the final state. Flavor excitation consists of an initial state gluon splitting into a $b\overline{b}$ pair before interacting with a parton from the other hadron. In gluon splitting, a gluon in the final state splits into a $b\overline{b}$ pair.

In the Monte Carlo, direct production, flavor excitation and gluon splitting, are defined by the number of b quarks entering and leaving the leading-order matrix element. Direct production has no b quarks in the initial state and two of them are in the final state. Flavor excitation has one b quark in both the initial and final states. The initial b quark belongs to the proton sea and is described by the parton distribution function. Gluon splitting has no b quarks in neither the initial nor final

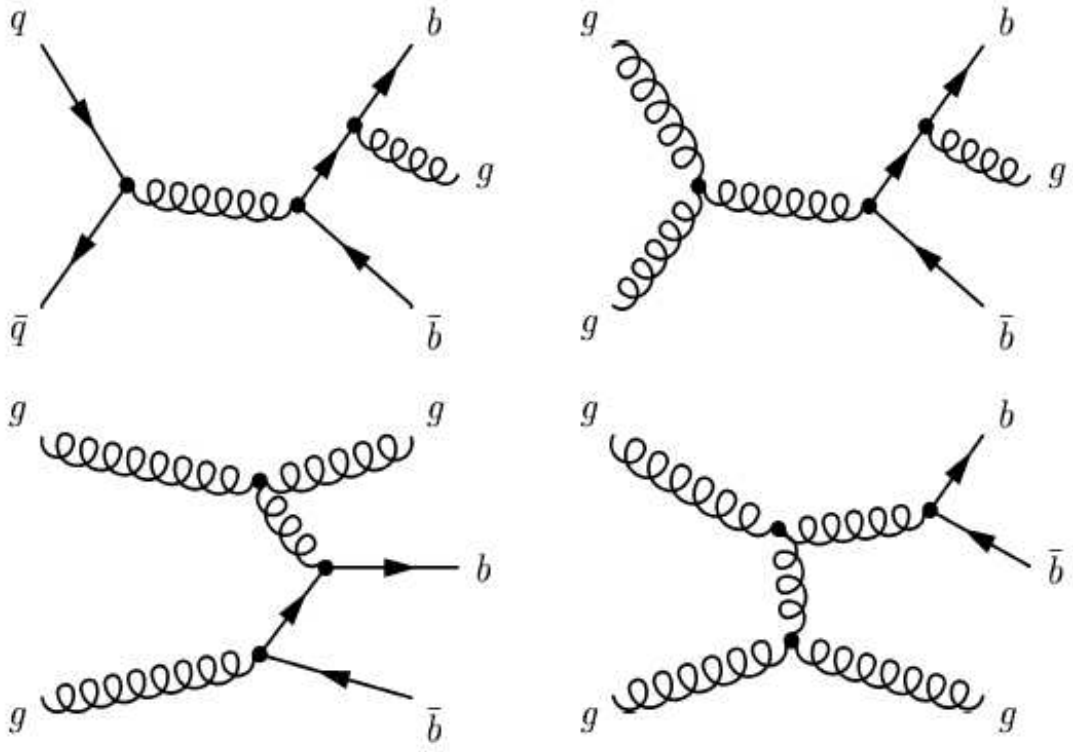

Figure 2.2: Next-to-Leading order diagrams for $b\overline{b}$ production.

state. The $b\overline{b}$ pair is created during the parton showering process. Final state b quarks hadronize into B hadrons. During the fragmentation process, other particles will also be produced along with the B hadron, giving rise to b-jets[1].

The partons from the proton and anti-proton remnants, not directly involved in the b quark production, also undergo hadronization generating the so-called *underlying event*, confirmed by low p_T particles which tend to have small angles with respect to the beam pipe. In general, the momentum of the underlying particles are uncorrelated with the final B hadron direction.

Directly produced b-jets are p_T balanced and back-to-back in the azimuthal angle ϕ. However they are not momentum balanced because b-jets may be boosted in the

[1]A jet is a narrow cone of hadrons and other particles produced by the hadronization of a quark or gluon

z direction due to the different proton momentum fractions carried by the initial partons. In the flavor excitation process, the b quark which does participate in the hard scattering belongs to the underlying event, resulting in a forward (large η) b-jet. The angular $\Delta\phi$ separation between the two b-jets is therefore expected to be flat. Gluon splitted b-jets are expected to be collinear since they originate from the splitting of a gluon and will tend to be identified as as same hadronic jet. The azimuthal separation between the two gluon splitted b-jets thus peaks at small angles.

2.2 Heavy Flavor Hadrons

B hadrons are produced as a result of the hadronization process of b quarks. Since the probability for quark-antiquark creation from the vaccum depends on the quark-antiquark mass, the most common B hadrons are $B^+(\overline{b}u)$ and $B^0(\overline{b}d)$ which involve light quarks. Each comprises approximately 38% of the produced B hadrons. $B_s^0(\overline{b}s)$ is the next most common B meson, comprising about 10% of the cases. The B_c^+ meson is made of a c and a b quark and, the c quark being much more massive than the $u-d-s$, they amount to only about $\sim$ 0.001% of the B hadrons produced in $p\overline{p}$ collisons. The remaining hadrons are basically comprised of Λ_b baryons. The hadronization process for the c quark is similar to that of the b quark, the resulting mesons are generically called D mesons Λ_c being the most common baryon. Table 2.3 summarizes the important B and D hadrons with some of their properties.

B hadrons decay via the weak interaction. The simplest decay description is provided by the *spectator* model, in which the heavy quark decays via an electroweak diagram into a virtual W and a c quark, and the lighter quark (the spectator) plays no role, see Fig. 2.3. B hadron decays are classified as semileptonic or hadronic depending on the W decay, which can respectively give rise to a charged lepton and its associated neutrino, or a quark-antiquark pair.

Table 2.3: Properties of some baryons and mesons [1].

Hadron	Constituents	Mass (MeV/c^2)	Lifetime (ps)
B^+	$b\overline{u}$	5279.1 ± 0.5	1.674 ± 0.018
B^0	$b\overline{d}$	5279.3 ± 0.7	1.542 ± 0.016
B_s^0	$b\overline{s}$	5369.6 ± 2.4	1.461 ± 0.057
B_c^+	$b\overline{c}$	6400.0 ± 520	0.46 ± 0.21
Λ_b^0	bud	5624 ± 0.9	1.229 ± 0.080
D^+	$c\overline{d}$	1869.4 ± 0.5	1.051 ± 0.013
D^0	$c\overline{u}$	1864.1 ± 1.0	0.474 ± 0.028
D_s^+	$c\overline{s}$	1969.0 ± 1.4	0.490 ± 0.09
Λ_c^+	cud	2284.9 ± 0.6	0.200 ± 0.006

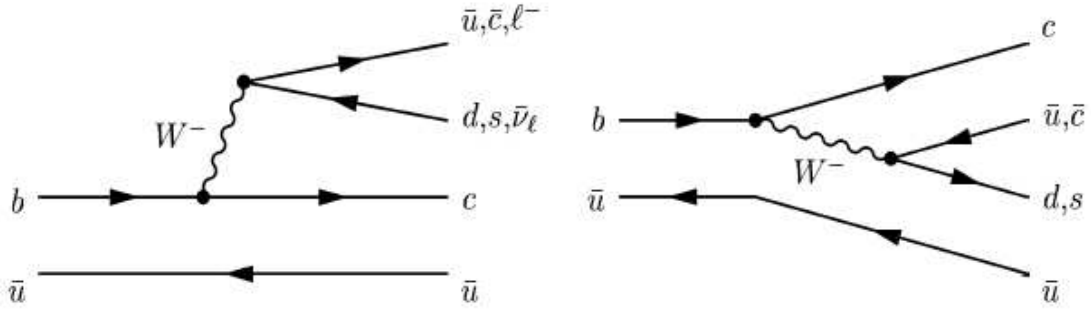

Figure 2.3: Feynman diagrams for B^- decays in the spectator model.

2.3 Quark Mixing

Mixing is the process whereby some neutral mesons change from their particle state to their anti-particle state, and vice versa. This kind of oscillation of flavor eigenstates into one another was first observed in the K^0 meson system [6]. Since weak interactions need not conserve the flavor quantum number, transitions between K^0 and $\overline{K}^0$ with opposite strangeness are permitted. K^0 and $\overline{K}^0$ are not the mass eigenstates; they do not have definite masses and definite lifetimes since weak interactions do not conserve strangeness. Their linear combinations K_S^0 and K_L^0 are associated with particles of definite and distinct mass M_S and M_L and mean lifetimes Γ_S^{-1} and Γ_L^{-1} respectively. The mass difference between these states ΔM results in a time-dependent phase difference between the K_S^0 and K_L^0 wave functions and a consequent

periodic variation of the K^0 and $\overline{K}^0$ components [7]. Thus the K^0 and $\overline{K}^0$ oscillations are observed with a period given by $2\pi/\Delta M$. The short-lived K_S^0 only decays significantly to $\pi^+\pi^-$ and $\pi^0\pi^0$, each with CP eigenvalue equal to +1. The K_L^0 particle decays into many modes including $\pi^+\pi^-\pi^0$, all of which are eigenstates of CP with eigenvalue equal to -1.

Cross-generational coupling (in the quark sector) was first introduced in 1963 by Cabibbo [8]. He suggested that the d $\rightarrow$ u + W^- vertex carries a multiplicative factor of $\cos\theta_c$, whereas the s $\rightarrow$ u + W^- vertex carries a factor of $\sin\theta_c$. The second one is weaker and hence θ_c is small ($\theta_c = 12.7^0$ experimentally). This was a fairly successful model except for the fact that it allowed the $K^0 \rightarrow \mu^+\mu^-$ decay. According to Cabibbo's model, the width should be $\Gamma(K^0 \rightarrow \mu^+\mu^-) \approx \sin\theta_c \cos\theta_c$. However, this was considerably larger than the experimentally set limit. Glashow, Iliopolos and Maiani came to the rescue of the Cabibbo model in 1970 by postulating the GIM mechanism [9]. This was an extension of the Cabibbo model and included the fourth quark called the *charm* (or $c-quark$) that formed a doublet with the strange quark. In this model the $d \rightarrow c + W^-$ and $s \rightarrow c + W^-$ vertices were associated with factors of $-\sin\theta_c$ and $\cos\theta_c$, respectively, such that the superposition of the Feynman diagrams with the virtual u and c quarks cancel, and the width $\Gamma(K^0 \rightarrow \mu^+\mu^-) \approx 0$. In general, the GIM mechanism suggested that instead of the physical quarks d and s, the states to use for weak interactions are d' and s', given by

$$d' = (\cos\theta_c)d + (\sin\theta_c)s, \tag{2.2}$$

$$s' = (-\sin\theta_c)d + (\cos\theta_c)s. \tag{2.3}$$

The phenomena is called quark mixing and Eqs. 2.2 and 2.3 can then be rewritten using the so called "mixing" matrix which is simply a rotation of the quark basis by

the Cabibbo angle θ_c:

$$\begin{pmatrix} d' \\ s' \end{pmatrix} = \begin{pmatrix} \cos\theta_c & \sin\theta_c \\ -\sin\theta_c & \cos\theta_c \end{pmatrix} \begin{pmatrix} d \\ s \end{pmatrix} \tag{2.4}$$

The W's then couple to the "Cabibbo rotated" states

$$\begin{pmatrix} u \\ d' \end{pmatrix} \text{ and } \begin{pmatrix} c \\ s' \end{pmatrix}, \tag{2.5}$$

and decays that involve a factor of $\sin\theta_c$ are known as 'Cabibbo suppressed' decays.

2.4 CKM Matrix

In the Standard Model quarks and leptons are coupled to the W-boson field via the charged current J^{μ}_{cc}. The Lagrangian for charged current processes is given by

$$\mathcal{L}_{cc} = -\frac{g}{\sqrt{2}}(J^{\mu}_{cc}W^{+}_{\mu} + J^{\mu\dagger}_{cc}W^{-}_{\mu}) \tag{2.6}$$

where

$$J^{\mu}_{cc} = \sum_k \overline{\nu}_k\gamma^{\mu}\frac{1}{2}(1-\gamma^5)e_k + \sum_{i,j}\overline{u}_i\gamma^{\mu}\frac{1}{2}(1-\gamma^5)V_{ij}d_j \tag{2.7}$$

and the sums (i, j, k) are over the 3 generations. The 3×3 unitary matrix V is the so called CKM matrix [8] which describes the coupling of the charge 2/3 quarks with the charge $-1/3$ quarks and is given as:

$$V = \begin{pmatrix} V_{ud} & V_{us} & V_{ub} \\ V_{cd} & V_{cs} & V_{cb} \\ V_{td} & V_{ts} & V_{tb} \end{pmatrix} \tag{2.8}$$

The CKM matrix is typically parameterized in some specific way to incorporate unitary constraints. In general an $n \times n$ complex matrix has $2n^2$ parameters. However, unitary requires $V^\dagger V = 1$ which halves the number of independent parameters. Therefore, only n^2 free parameters are left. As the phases are arbitrary, 2n-1 of them can be absorbed by phase rotations. We are then left with $(n-1)^2$ physically independent parameters. Furthermore, a unitary matrix is a complex extension of an orthogonal matrix, therefore n(n-1)/2 parameters are identified with rotation angles, leaving (n-2)(n-1)/2 complex phases. Hence, for three generations (n=3), the CKM matrix has four independent parameters. Three of them are identified with the real Euler angles, leaving a single complex phase. This complex phase allows for the accommodation of CP violation. Note that if $n < 3$, as in the original GIM model, there is no phase left in the matrix and consequently no CP violation. This was the original motivation behind Kobayashi and Maskawa's [10] proposals for a third generation of quarks.

It should also be noted that CP is not necessarily violated in the three generation SM. If two quarks of the same charge have equal masses, one mixing angle and phase could be removed from CKM matrix. This leads to a condition on quark mass differences being imposed for CP violation:

$$F_u \neq 0; \quad \text{and} \quad F_d \neq 0, \tag{2.9}$$

where

$$\begin{aligned} F_u &= (m_u^2 - m_c^2)(m_c^2 - m_t^2)(m_t^2 - m_u^2), \\ F_d &= (m_d^2 - m_s^2)(m_s^2 - m_b^2)(m_b^2 - m_d^2). \end{aligned} \tag{2.10}$$

Another useful way of representing the above is by re-writing the commutator of the

mass matrices, C = [$\mathcal{M}_u\mathcal{M}_u^\dagger, \mathcal{M}_d\mathcal{M}_d^\dagger$], as

$$C = U_{uL}^\dagger[(m_u)^2, V(m_d)^2V^\dagger]U_{uL} \tag{2.11}$$

which shows that det C depends on the physical masses and V.

The determinant det C illustrates several essential features of CP violation in the SM:

- det C is imaginary, implying that CP violation originates from a complex coupling.
- There is no CP violation unless F_u and F_d are non-zero.
- Non-zero F_u and F_d impose conditions on the quark masses. (Eq. 2.10).

The CKM matrix has four quantities having physical significance with three mixing angles and one CP violating phase. These can be parameterized in many different ways. The Particle Data Group favors the Chau-Keung parameterization[11]:

$$V = \begin{pmatrix} c_{12}c_{13} & s_{12}c_{13} & s_{13}e^{-i\delta_{13}} \\ -s_{12}c_{23} - c_{12}s_{23}s_{13}e^{i\delta_{13}} & c_{12}c_{23} - s_{12}s_{23}s_{13}e^{i\delta_{13}} & s_{23}c_{13} \\ s_{12}c_{23} - c_{12}c_{23}s_{13}e^{i\delta_{13}} & -c_{12}s_{23} - s_{12}c_{23}s_{13}e^{i\delta_{13}} & c_{23}c_{13} \end{pmatrix} \tag{2.12}$$

where $c_{ij} = \cos\theta_{ij}$ and $s_{ij} = \sin\theta_{ij}$ control the mixing between the families and δ_{13} is the CP violating phase also called the KM phase.

A convenient parameterization of the CKM matrix was developed by Wolfenstein [12]. He exploited the hierarchy observed in the measured values of the matrix, with diagonal elements close to one, and progressively smaller elements away from the diagonal. This hierarchy was formalized by defining λ, A, ρ and η such that

$$\lambda \equiv s_{12},\ A \equiv s_{23}/\lambda^2,\ \rho - i\eta \equiv s_{13}e^{-i\delta_{13}/A\lambda^3}. \tag{2.13}$$

From experiment $\lambda \approx 0.22$, $A \approx 0.90 \pm 0.12$, and $\sqrt{\rho^2+\eta^2} \approx 0.39 \pm 0.07$, so every element of the CKM matrix, V, was expanded as a power series in the small parameter $\lambda = |V_{us}|$. Neglecting terms of $o(\lambda^4)$ resulted in the famous "Wolfenstein parameterization":

$$V = \begin{pmatrix} 1-\frac{1}{2}\lambda^2 & \lambda & A\lambda^3(\rho - i\eta) \\ -\lambda & 1-\frac{1}{2}\lambda^2 & A\lambda^2 \\ A\lambda^3(1-\rho-i\eta) & -A\lambda^2 & 1 \end{pmatrix} + o(\lambda^4). \tag{2.14}$$

λ, A and $\sqrt{\rho^2+\eta^2}$ are real while the phase in question is given by $\arg(\rho, \eta)$. This parameterization allows for CP violation if $\eta \neq 0$. The experimentally allowed values [13] for the matrix elements, allowing for the possibility of more than three generations are

$$\begin{pmatrix} 0.9720-0.9752 & 0.217-0.223 & 0.002-0.005 & ... \\ 0.199-0.234 & 0.818-0.975 & 0.036-0.046 & ... \\ 0-0.11 & 0-0.52 & 0-0.9993 & ... \\ . & . & . & . \\ . & . & . & . \\ . & . & . & . \end{pmatrix} \tag{2.15}$$

Using the unitarity property of the CKM matrix one obtains the following six equations:

$$V_{ud}V_{us}^* + V_{cd}V_{cs}^* + V_{td}V_{ts}^* = 0, \tag{2.16}$$

$$V_{us}V_{ub}^* + V_{cs}V_{cb}^* + V_{ts}V_{tb}^* = 0, \tag{2.17}$$

$$V_{ud}V_{ub}^* + V_{cd}V_{cb}^* + V_{td}V_{tb}^* = 0, \tag{2.18}$$

$$V_{ud}V_{cd}^* + V_{us}V_{cs}^* + V_{ub}V_{cb}^* = 0, \tag{2.19}$$

$$V_{cd}V_{td}^* + V_{cs}V_{ts}^* + V_{cb}V_{tb}^* = 0, \tag{2.20}$$

$$V_{ud}V_{td}^* + V_{us}V_{ts}^* + V_{ub}V_{tb}^* = 0, \tag{2.21}$$

where the first three relations express the orthogonality of two different columns, and the last three express the orthogonality of two different rows. These relations can be geometrically represented in the complex plane as "unitarity" triangles with rather different shapes. Aligning $V_{cd}V_{cb}^*$ with the real axis and dividing all sides by its magnitude $|V_{cd}V_{cb}^*|$ (or $A\lambda^3$), one obtains a rescaled Unitarity Triangle. Fig. 2.4 shows the rescaled unitarity triangle. Two vertices of the rescaled unitarity triangle are thus fixed at (0,0) and (1,0) while the coordinates of the third vertex is denoted by the Wolfenstein parameters (ρ,η). The three angles of the triangle are given by:

$$\alpha = arg[-\frac{V_{td}V_{tb}^*}{V_{ud}V_{ub}^*}],\ \beta = arg[-\frac{V_{cd}V_{cb}^*}{V_{td}V_{tb}^*}],\ \gamma = arg[-\frac{V_{ud}V_{ub}^*}{V_{cd}V_{cb}^*}]. \tag{2.22}$$

where by reconstruction $\alpha + \beta + \gamma = \pi$.

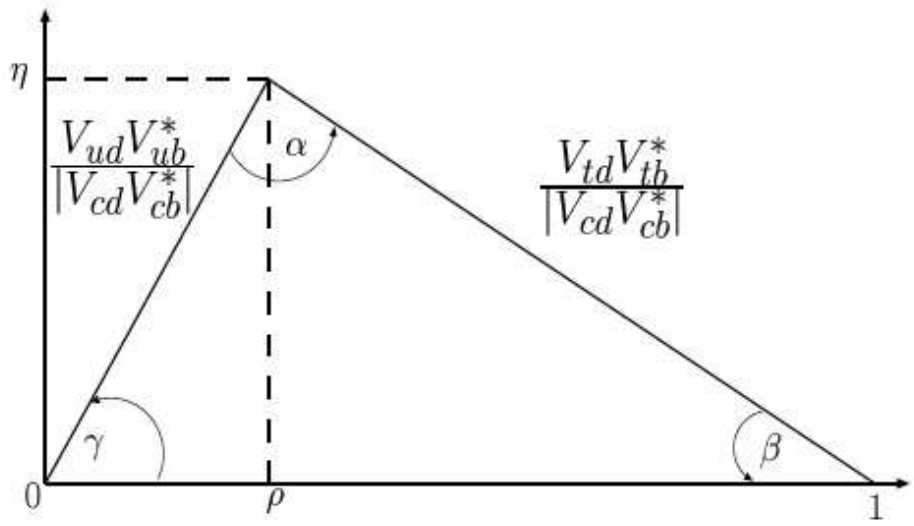

Figure 2.4: The rescaled Unitarity Triangle.

2.5 Neutral $B\overline{B}$ Mixing

The only hadrons that can undergo oscillations are K^0, D^0, B^0 and B_s^0 mesons. The π^0 is its own antiparticle, the top quark is so heavy that it decays before forming stable hadrons, and excited meson states decay strongly or electromagnetically before any mixing can occur. Mixing is expected to be a very small effect in D^0 mesons and has not been observed yet. Mixing in kaons has already been discussed in sec 2.3 and was first observed in 1956 [6]. Mixing in B mesons was first observed in an admixture of B^0 and B_s^0 by UA1 [14] and then in B^0 mesons by ARGUS [15]. Mixing in B_s^0 was established very recently by D0 Collaboration, see chapter 5 [16] and subsequently by the CDF Collaboration [17].

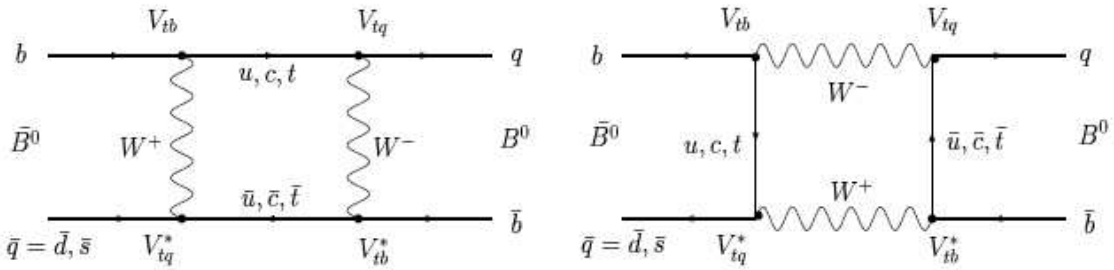

Figure 2.5: Leading order box diagrams for B mixing.

Consider an initially produced B^0 or $\overline{B}^0$ that evolves in time into a superposition of B^0 and$\overline{B}^0$. Figure 2.5 shows the Leading Order box diagrams for the mixing in the B system. Note through W exchange the initial quarks and antiquarks become antiquarks and quarks, respectively. Let $|B^0\rangle$ denote the state vector of a B meson which is tagged as a B^0 at time t = 0, i.e., $|B^0(t = 0)\rangle = |B^0\rangle$. Similarly, $\overline{B}^0$ represents a B meson initially tagged as a $\overline{B}^0$. The time evolution of these states is

given by the following Schrodinger equation:

$$i\frac{d}{dt}\begin{pmatrix} |B^0(t)\rangle \\ |\overline{B}^0(t)\rangle \end{pmatrix} = \begin{pmatrix} M_{11} - \frac{i}{2}\Gamma_{11} & M12 - \frac{i}{2}\Gamma_{12} \\ M_{12}^* - \frac{i}{2}\Gamma_{12}^* & M_{22} - \frac{i}{2}\Gamma_{22} \end{pmatrix} \tag{2.23}$$

where the mass and decay matrices (M and Γ) are 2×2 t-independent Hermitian matrices. CPT invariance requires that $M_{11} = M_{22}$ and $\Gamma_{11} = \Gamma_{22}$ so that the particle and anti-particle have the same mass and lifetime. $B^0 - \overline{B}^0$ transitions are induced by non-zero off-diagonal elements where M_{12} represents the virtual transitions and Γ_{12} represents the real transitions through common decay modes. These common modes are Cabibbo suppressed so that the $B^0 - \overline{B}^0$ mixing amplitude is dominated by virtual transitions. Diagonalization of the Hamiltonian matrix yields the mass eigenstates that can be expressed in terms of the flavor eigenstates as

$$|B_L\rangle = p|B^0\rangle + q|\overline{B}^0\rangle, \tag{2.24}$$

$$|B_H\rangle = p|B^0\rangle - q|\overline{B}^0\rangle, \tag{2.25}$$

then,

$$\frac{q}{p} = \sqrt{\frac{M_{12}^* - \frac{i}{2}\Gamma_{12}^*}{M_{12} - \frac{i}{2}\Gamma_{12}}} \tag{2.26}$$

where B_L and B_H are the light and heavy mass eigenstates, respectively, and the complex coefficients p and q obey the normalization condition $|p|^2 + |q|^2 = 1$. The two eigenvalues are

$$\omega_L = M_L - i\Gamma_L/2, \tag{2.27}$$

$$\omega_H = M_H - i\Gamma_H/2, \tag{2.28}$$

where $M_{H,L}$ and $\Gamma_{H,L}$ are the masses and widths of the physical states B_H and B_L. The mass difference , Δm, and the width difference, $\Delta\Gamma$, between the neutral B

mesons are defined using the convention:

$$\Delta\omega \equiv \omega_H - \omega_L = \Delta m - \frac{i}{2}\Delta\Gamma, \tag{2.29}$$

$$\Delta m \equiv M_H - M_L = \Re e(\Delta\omega), \tag{2.30}$$

$$\Delta\Gamma \equiv \Gamma_H - \Gamma_L = -2\Im m(\Delta\omega). \tag{2.31}$$

The eigenvalue problem

$$det|M - \frac{i}{2}\Gamma - \omega| = 0 \tag{2.32}$$

results in the condition

$$\Delta\omega = 2\sqrt{(M_{12}^* - i\Gamma_{12}^*/2)(M_{12} - i\Gamma_{12}/2)} \tag{2.33}$$

The real and imaginary parts of this equation give

$$\begin{aligned}(\Delta m)^2 - \frac{1}{4}(\Delta\Gamma)^2 &= 4|M_{12}|^2 - |\Gamma_{12}|^2, \\ \text{and } \Delta m\Delta\Gamma &= 4\Re e(M_{12}\Gamma_{12}^*)\end{aligned} \tag{2.34}$$

Using above two equations, Eqs. 2.30 and 2.31 can be re-written in terms of the matrix elements M_{12} and Γ_{12} as:

$$\Delta m = \sqrt{2}\left(|M_{12}|^2 - \frac{1}{4}|\Gamma_{12}|^2 + \sqrt{(|M_{12}|^2 - \frac{1}{4}|\Gamma_{12}|^2)^2 + [\Re e(M_{12}\Gamma_{12}^*)]^2}\right)^{\frac{1}{2}}, \tag{2.35}$$

$$\Delta\Gamma = 2\sqrt{2}\left(\sqrt{|M_{12}|^2 - \frac{1}{4}|\Gamma_{12}|^2 + [\Re e(M_{12}\Gamma_{12}^*)]^2 - (|M_{12}|^2 - \frac{1}{4}|\Gamma_{12}|^2)}\right)^{\frac{1}{2}} \tag{2.36}$$

solving for the eigenvalues gives

$$\frac{q}{p} = \frac{-\Delta\omega}{2(M_{12} - \frac{i}{2}\Gamma_{12})} = -\frac{2(M_{12}^* - \frac{i}{2}\Gamma_{12}^*)}{\Delta m - \frac{i}{2}\Delta\Gamma} \tag{2.37}$$

The time evolution of the mass eigenstates is then governed by the two eigenvalues $M_H - i\Gamma_H/2$ and $M_L - i\Gamma_L/2$ such that

$$|B_{H,L}(t)\rangle = e^{-(iM_{H,L}+\Gamma_{H,L}/2)t}|B_{H,L}\rangle, \tag{2.38}$$

where $|B_{H,L}\rangle$ denotes the mass eigenstates at time t = 0 (i.e. $|B_{H,L}\rangle = |B_{H,L}(t=0)\rangle$). Now, inverting Eq. 2.5 to express $|B^0\rangle$ and $|\overline{B}^0\rangle$ in terms of the mass eigenstates and using their time evolution in Eq. 2.37, we get:

$$|B^0(t)\rangle = \frac{1}{2p}[e^{-iM_Lt-\Gamma_Lt/2}|B_L\rangle + e^{-iM_Ht-\Gamma_Ht/2}|B_H\rangle], \tag{2.39}$$

$$|\overline{B}^0(t)\rangle = \frac{1}{2q}[e^{-iM_Lt-\Gamma_Lt/2}|B_L\rangle - e^{-iM_Ht-\Gamma_Ht/2}|B_H\rangle] \tag{2.40}$$

Eliminating the mass eigenstates in Eqs. 2.39 and 2.40 in favor of the flavor eigenstates we get:

$$\begin{aligned} |B^0(t)\rangle &= g_+(t)|B^0\rangle + g_-(t)\frac{q}{p}|\overline{B}^0\rangle, \\ |\overline{B}^0(t)\rangle &= g_-(t)\frac{p}{q}|B^0\rangle + g_+(t)|\overline{B}^0\rangle, \end{aligned} \tag{2.41}$$

where

$$g_\pm(t) \equiv \frac{1}{2}e^{-iMt}e^{-\frac{\Gamma}{2}t}\left(e^{\frac{\Delta\Gamma}{4}t}e^{i\frac{\Delta m}{2}t} \pm e^{-\frac{\Delta\Gamma}{4}t}e^{-i\frac{\Delta m}{2}t}\right) \tag{2.42}$$

and $M \equiv \frac{1}{2}(M_H + M_L)$ while $\Gamma \equiv \frac{1}{2}(\Gamma_H + \Gamma_L)$.

The above equation indicates that for $t > 0$ there is a finite probability that a $|B^0\rangle$ can be observed as a $|\overline{B}^0\rangle$ and vice versa.

Let $P_m^B(t)$ denote the probability that a particle produced as a B oscillated (mixed) and decayed as a $\overline{B}$. Let $P_u^B(t)$ denote the conjugate probability that this particle did not oscillate, that is, it remained unmixed. Then Eqs. 2.41 and 2.42 give the

following:

$$P_u^B(t) = \frac{e^{-\Gamma t}}{\Gamma\left(\frac{1+|q/p|^2}{\Gamma^2-\Delta\Gamma^2/4} + \frac{1-|q/p|^2}{\Gamma^2+\Delta m^2}\right)}(\cosh\frac{\Delta\Gamma}{2}t + \cos\Delta mt), \tag{2.43}$$

$$P_m^B(t) = \frac{|q/p|^2 e^{-\Gamma t}}{\Gamma\left(\frac{1+|q/p|^2}{\Gamma^2-\Delta\Gamma^2/4} + \frac{1-|q/p|^2}{\Gamma^2+\Delta m^2}\right)}(\cosh\frac{\Delta\Gamma}{2}t - \cos\Delta mt), \tag{2.44}$$

$$P_u^{\overline{B}}(t) = \frac{|q/p|^2 e^{-\Gamma t}}{\Gamma\left(\frac{1+|q/p|^2}{\Gamma^2-\Delta\Gamma^2/4} - \frac{1-|q/p|^2}{\Gamma^2+\Delta m^2}\right)}(\cosh\frac{\Delta\Gamma}{2}t + \cos\Delta mt), \tag{2.45}$$

$$P_m^{\overline{B}}(t) = \frac{e^{-\Gamma t}}{\Gamma\left(\frac{1+|q/p|^2}{\Gamma^2-\Delta\Gamma^2/4} - \frac{1-|q/p|^2}{\Gamma^2+\Delta m^2}\right)}(\cosh\frac{\Delta\Gamma}{2}t - \cos\Delta mt), \tag{2.46}$$

Note that these equations are not symmetric between B and $\overline{B}$ states.

These equations have two limiting cases: Neglecting CP violation in the mixing, and neglecting lifetime difference $\Delta\Gamma$ (which also in general implies there is no CP violation in the mixing).

Equation 2.5 can then be written as

$$|B_L\rangle = \frac{p+q}{2}\left[(|B\rangle + |\overline{B}\rangle) + \frac{1-q/p}{1+q/p}(|B\rangle - |\overline{B}\rangle)\right], \tag{2.47}$$

and similar equation for $|B_H\rangle$. So, here $(1-q/p)/(1+q/p) \equiv \epsilon_B$ is a measure of the amount by which $|B_L\rangle$ and $|B_H\rangle$ differ from CP eigenstates. ϵ_B is expected to be very small in the standard model, $o(10^{-3})$. The limit of no CP violation in mixing is thus $q/p = 1$. In this limit B and $\overline{B}$ symmetry is regained, and we obtain unmixed and mixed decay probabilities for both B and $\overline{B}$ of:

$$P_{u,m}(t) = \frac{1}{2}\Gamma e^{-\Gamma t}\left(1 - \frac{\Delta\Gamma^2}{4\Gamma^2}\right)(\cos h\frac{\Delta\Gamma}{2}t \pm \cos\Delta mt), \tag{2.48}$$

where the + sign corresponds to P_u. This form is appropriate for B_s^0 mesons which are not expected to be subject to large CP-violating effects.

On the other hand, even in the presence of CP violation, a simple form can be obtained. The lifetime difference between the heavy and light states is expected to

be small, $\Delta\Gamma/\Gamma \leq 1\%$ for the B^0 and perhaps as large as 25% for the B_s^0 [18].

From Eq. 2.34, $\Delta\Gamma = 0$ in general only if $\Gamma_{12} = 0$. In this case

$$\frac{q}{p} = \sqrt{\frac{M_{12}^* - \frac{i}{2}\Gamma_{12}^*}{M_{12} - \frac{i}{2}\Gamma_{12}}} = \sqrt{\frac{M_{12}^*}{M_{12}}} = e^{-i\phi}, \tag{2.49}$$

thus $|q/p| = 1$. In this $\Delta\Gamma = 0$ limit, the time evolutions from Eqs. 2.39 and 2.40 become

$$|B(t)\rangle = e^{-iMt}e^{-\frac{\Gamma}{2}t}\left(\cos\frac{\Delta m}{2}t|B\rangle + ie^{-i\phi}\sin\frac{\Delta m}{2}t|\overline{B}\rangle\right), \tag{2.50}$$

$$|\overline{B}(t)\rangle = e^{-iMt}e^{-\frac{\Gamma}{2}t}\left(\cos\frac{\Delta m}{2}t|\overline{B}\rangle + ie^{+i\phi}\sin\frac{\Delta m}{2}t|B\rangle\right). \tag{2.51}$$

The mixed and unmixed decay probabilities again become equal for the B and $\overline{B}$ mesons:

$$P_{u,m}(t) = \frac{1}{2}\Gamma e^{-\Gamma t}(1 \pm \cos\Delta m t). \tag{2.52}$$

This form is expected to be appropriate for $\overline{B}^0$ mesons, for which a large phase ϕ (the source of mixing-induced CP violation) is possible.

The time-integrated versions, expressing the probability that a B decays as a $\overline{B}$, of Eqs. 2.48 and 2.52, are

$$\chi = \int_0^\infty P_m(t) = \frac{1}{2}\frac{x^2 + \frac{1}{4}\frac{\Delta\Gamma^2}{\Gamma^2}}{1 + x^2} \tag{2.53}$$

and in the $\Delta\Gamma = 0$ limit,

$$\chi = \frac{1}{2}\frac{x^2}{1 + x^2} \tag{2.54}$$

where $x \equiv \Delta m/\Gamma$. Oscillations observed by any experiment are oscillations in space and not in time, therefore, one has a source creating a pure B or a $\overline{B}$ meson, which may have oscillated by the time it reaches the detector. In this spatial picture, we have a source, very small compared to the oscillation wavelength, which emits a pure B meson. The boundary condition that must be imposed, then, is that the

probability of finding a $\overline{B}$ meson at source must vanish at all time, otherwise a pure B would not be emanating. The $|B_L\rangle$ and $|B_H\rangle$ components propagate with phase $e^{i(E_{L,H}t - p_{L,H}x)}$, where x denotes the direction of motion. At the origin, the only way to ensure the wavefunction does not change the relative $|B_L\rangle - |B_H\rangle$ phase and develop a $\overline{B}$ component is the condition $E_L = E_H$. That is, the B meson has a definite energy. The components $|B_L\rangle$ and $|B_H\rangle$ will have the same energy but different momenta $p_{L,H} = \sqrt{E^2 - m^2_{L,H}}$ respectively. This induces spatial oscillations that go as $e^{i(p_H - p_L)x}$.

In the Standard Model, the lowest order contribution to B mixing is given by the box diagrams in Fig. 2.5. The dominant contribution is due to the exchange of the virtual top quark and hence using an effective field theory, the mass difference between heavy and light states can be written as:

$$\Delta m_q = 2|M^q_{12}| = \frac{G_F^2}{6\pi^2}\eta_B m_{B_q}\hat{B}_{B_q} f^2_{B_q} M^2_W S\left(\frac{m_t^2}{m_W^2}\right)|V_{tb}V^*_{tq}|^2, \tag{2.55}$$

with q = s or d, and where G_F is the Fermi constant and (at lowest order) is given by

$$\frac{G_F}{\sqrt{2}} = \frac{g^2}{8M_W^2} \tag{2.56}$$

η_B is a perturbative QCD correction factor, m_{B_q} is the B meson mass, and m_t is the top quark mass. The parameters f_{B_q} and $\hat{B}_q$ are the B_q decay constant and the "Bag parameter", respectively. $S\left(\frac{m_t^2}{M_W^2}\right)$ is the Inami-Lim function, given by

$$S(x_q) = x_q\left(\frac{1}{4} + \frac{9}{4(1-x_q)} - \frac{3}{2(1-x_q)^2}\right) - \frac{3}{2}\frac{x_q^3 log x_q}{(1-x_q)^3} \tag{2.57}$$

with $x_q \equiv m_t^2/M_W^2$.

Eq. 2.55 suggests that a measurement of Δm_d should allow the extraction of the CKM matrix element V_{td}. Moreover, Δm_d has been precisely measured and the world

average is [1]:

$$\Delta m_d = 0.502 \pm 0.007 ps^{-1}. \tag{2.58}$$

Unfortunately, large theoretical uncertainties in the non-perturbative QCD factors, f_{B_q} and $\hat{B}_{B_q}$ dominate the extraction of V_{td} from Δm_d. At present, Lattice QCD calculations give about $15-20\%$ uncertainty [1]. This difficulty, however, is overcome if the B_s^0 mass difference, Δm_s is also measured. The CKM matrix element, $|V_{td}|$, can then be extracted from the ratio of the oscillations frequencies of the B_s^0 and B_d^0 mesons as:

$$\frac{\Delta m_s}{\Delta m_d} = \frac{m_{B_s^0}}{m_{B_d^0}} \xi^2 |\frac{V_{ts}}{V_{td}}|^2 \tag{2.59}$$

where $m_{B_s^0}$ and$m_{B_d^0}$ are the B_s^0 and B_d^0 masses, respectively, and $\xi^2 \equiv f_{B_s}^2 \hat{B}_{B_s} / f_{B_d}^2 \hat{B}_{B_d}$. Many of the theoretical uncertainties cancel out in the ratio and ξ has been estimated from Lattice QCD calculations to be $1.21 \pm 0.022^{+0.035}_{-0.014}$ [19]. Therefore, the ratio V_{ts}/V_{td} can be extracted from the measurements of Δm_s and Δm_d with a relatively small uncertainty of about 5%.

2.6 Experimental Technique

In general, a measurement of the time dependence of the neutral B meson oscillations requires knowledge of:

- Final state reconstruction of the decay products.
- The flavor of the B meson at its production time (Flavor tagging).
- The proper decay time t of the B meson.

2.6.1 Event Selection

The large $b\overline{b}$ production cross section at the Tevatron ($\sim 100\mu b$) provides a very large sample of B mesons. Since leptons are often produced in the decay of B mesons, either directly through the semileptonic decay chain ($b \to cl\nu$, where l is a lepton) or indirectly through sequential decays ($b \to c \to sl\nu$), the presence of high momentum muons or electrons can be used to obtain datasets enriched with events from $b\overline{b}$ production. Another characteristic of the B mesons which helps in differentiating between the signal and background is the relatively long lifetime of the B mesons: $\tau(B^+) = 1.671 \pm 0.018\ ps$, $\tau(B_d^0) = 1.536 \pm 0.014\ ps$ and $\tau(B_s^0) = 1.461 \pm 0.057\ ps$ [1]. This coupled with the Lorentz boost from the initial momentum of the b quark permits the B hadrons to travel several millimeters before decaying. Reconstructing the B decay point or "secondary vertex" and requiring it to be separated from the $p\overline{p}$ interaction point or "primary vertex" further enriches the data with events from $b\overline{b}$ production.

A B_s^0 meson can decay either semileptonically ($B_s^0 \to D_s^{(*)} l\nu X$) or through hadronic decay ($B_s^0 \to D_s^{(*)} n\pi$ where n is number of pions in the final state). Note that a B_s^0 meson almost always decays to a $D_s^{(*)}$ meson since the branching ratio $\mathcal{B}(B_s^0 \to D_s^{(*)} X) \sim 100\%$. The notation $D_s^{(*)}$ here is used to represent both D_s mesons and their excited states such as D_s^* and D_{s0}^*. Semileptonic decays have larger branching ratios in comparison to hadronic decays and are used in the analysis presented in this thesis. Semileptonic decays have an additional advantage that the lepton in the final state can be used to select or trigger on the event. However, these decays do suffer from the fact that they cannot be fully reconstructed since there is a neutrino in the final state which escapes detection. This leads to poorer proper time resolution as dicussed in the section 2.6.3.

At present three semileptonic decays of B_s^0 mesons are used at $D\emptyset$ for the Δm_s search. These are $B_s^0 \to D_s^- \mu^+ X$ with $D_s^- \to \phi\pi^-$ and $D_s^- \to K^* K^-$ and $B_s^0 \to$

$D_s^- e^+ \nu X$ with $D_s^- \to \phi\pi^-$. The decay $D_s^- \to K^* K^-$ is primarily discussed in this thesis. Results from all the three channels and their combination are also presented.

2.6.2 Flavor Tagging

In order to know whether a B meson has oscillated or not we need to know its flavor at production time, this is called "initial state tagging". The methods for tagging the initial state can be grouped into two categories: tagging the initial charge of the b quark in the B_s^0 candidate itself (same side tag) and tagging the flavor of the b quark in the event (opposite side tag). Only opposite side tagging has been used in the current analysis.

The opposite side tagger makes use of the fact that the dominant mode of B quark production at the Tevatron is back-to-back $b\overline{b}$ or that the $b/\overline{b}$ quark of interest (reconstructed B meson) is always produced along with another $\overline{b}/b$ quark of opposite charge. The other $b/\overline{b}$ in the event is called the opposite side b. Determining the flavor of the opposite side B mesons allows us to infer the flavor of the reconstructed B meson. The opposite side lepton tagger, for example, relies on identifying the flavor of the other B in the event using the sign of the lepton it decayed to - a negative lepton corresponds to a b quark, and vice versa. For reconstructed $B_s^0 \to D_s^- \mu^+ X$ decays both leptons having the same sign would indicate that one B hadron has oscillated while opposite signs would indicate that neither (or both) has oscillated.

Another tagging technique determines the flavor of the opposite-side b hadron by analyzing the jet associated with it. A momentum-weighted charge distribution of all the tracks in the jet is used to form a variable to discriminate between b and $\overline{b}$ quarks. Figure 2.6 shows the schematic of the tagging.

The figure of merit typically used to compare different tagging algorithms is the "tagging power" or $\epsilon\mathcal{D}^2$ where ϵ is the tagging efficiency (or rate) and $\mathcal{D}$ is the

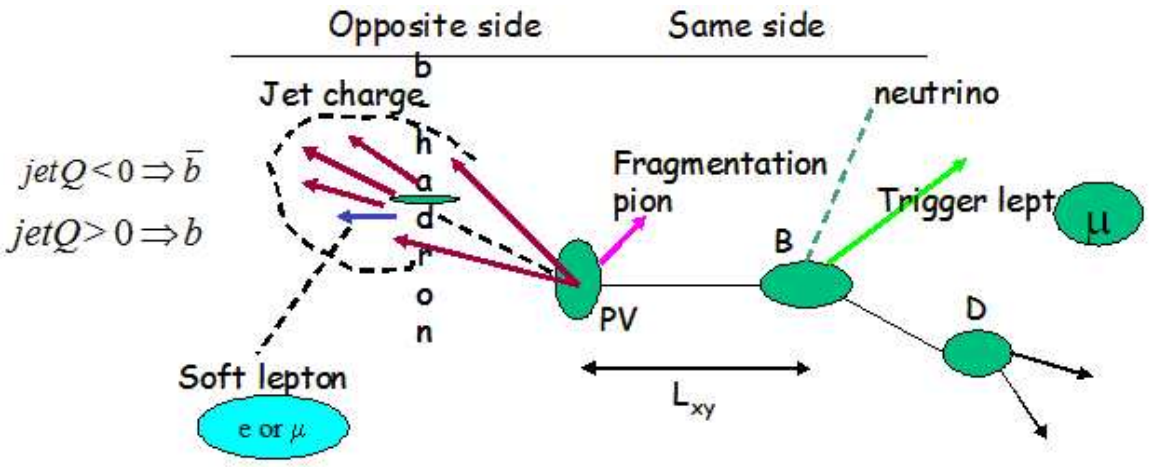

Figure 2.6: A diagram showing the tagging details.

"dilution" given by:

$$\epsilon \equiv \frac{N_{correct} + N_{wrong}}{N_{correct} + N_{wrong} + N_{notag}} \text{ and } \mathcal{D} \equiv \frac{N_{correct} - N_{wrong}}{N_{correct} + N_{wrong}} \tag{2.60}$$

where $N_{correct}$ (N_{wrong}) is the number of events that have been correctly (incorrectly) tagged and N_{notag} is the number of events that do not have a tag.

Eq. 2.60 indicates that a tagging algorithm with large dilution characterizes a more powerful tagging method than one with a smaller dilution. A large dilution is, therefore, desirable. This makes the term "dilution" counter-intuitive and its use can sometimes be misleading. It is, therefore, better to use the purity, η_s, of the tagging technique instead:

$$\eta_s \equiv N_{correct}/N_{total\ tagged\ events} \tag{2.61}$$

where η_s is related to the dilution, $\mathcal{D}$, using the simple formula $\mathcal{D} \equiv 2\eta_s - 1$. A new tagging method with electron as the tag lepton was developed and is discussed in detail in chapter 4. The other taggers used in this analysis are described in detail in the same Chapter.

2.6.3 Proper time resolution

The proper lifetime of the B_s^0 meson, $ct_{B_s^0}$, is obtained from the measurement of the distance, L^B, between its production vertex and its decay vertex such that

$$ct_{B_s^0} = \frac{L^B}{\beta\gamma} = L^B \frac{M_{B_s^0}}{p(B_s^0)} \tag{2.62}$$

where β is the speed of the B_s^0 meson, γ is the Lorentz boost factor, and $M_{B_s^0}$ and pB_s^0 are the mass and momentum of the B_s^0 meson, respectively. The above is projected in the plane transverse to the beam line since the transverse distance, L_{xy}^B, and the transverse momentum, $p_T(B_s^0)$, are measured more accurately than L^B and p(B):

$$ct_{B_s^0} = L_{xy}^B \frac{M_{B_s^0}}{p_T(B_s^0)} \tag{2.63}$$

In the case of semileptonic decays the full momentum of the B_s^0 meson cannot be reconstructed since the neutrino in undetected. Instead, the combined momentum of the $D_s\mu$ pair, $p_T(D_s\mu)$, is used to calculate the Visible Proper Decay Length (VPDL) or x^M given by

$$x^M \equiv L_{xy}^B \frac{M_{B_s^0}}{p_T(D_s\mu)}, \tag{2.64}$$

where L_{xy}^B is the measured decay length and is defined as the displacement $\vec{X}_{xy}^B$ in the transverse plane between the secondary B_s^0 vertex (V_B in Fig. 2.7) in the primary vertex (V_P in the Fig. 2.7) projected onto the transverse momentum of the D_s^μ system such that

$$L_{xy}^B \equiv \frac{\vec{X}_{xy}^B \cdot \vec{p}_T(D_s\mu)}{|\vec{p}_T(D_s\mu)|} \tag{2.65}$$

Using Eqs. 2.64 and 2.65 the VPDL is expressed as

$$x^M = \frac{\vec{X}_{xy}^B \cdot \vec{p}_T(D_s\mu)}{p_T(D_s\mu)} \cdot \frac{M_{B_s^0}}{p_T(D_s\mu)} \tag{2.66}$$

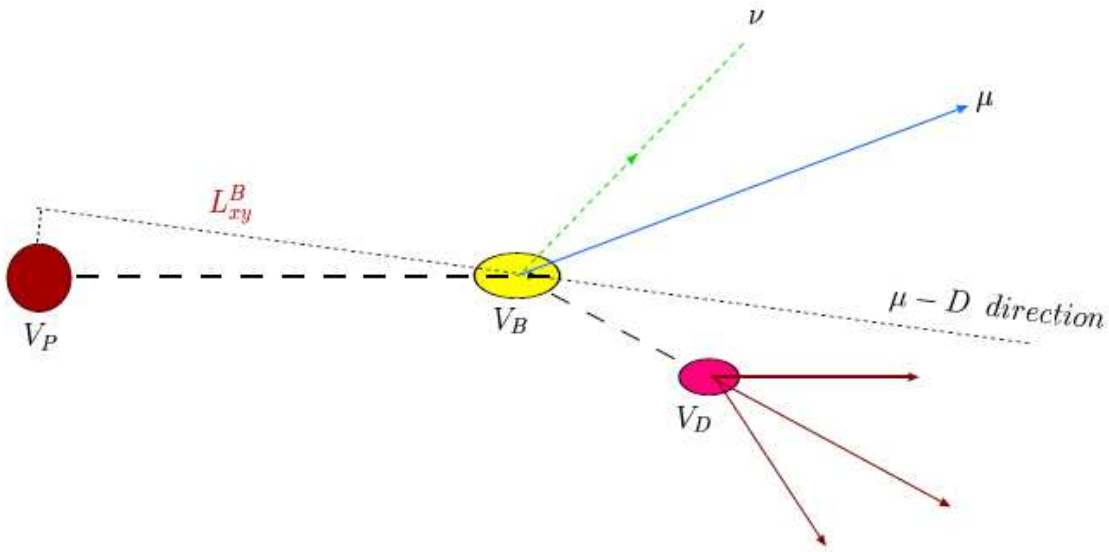

Figure 2.7: Schematic of a $B \to D\mu\nu X$ decay.

The actual proper lifetime is then obtained using Eq. 2.66 and a correction factor such that

$$ct_{B_s^0} = x^M \cdot K \tag{2.67}$$

$K \equiv p_T(D_s\mu)/p_T(B_s^0)$ and is known as the K-factor. It is essentially a correction factor used in semileptonic decays to account for the missing neutrino (and other neutral or non-reconstructed charged particles). K-factor distributions are obtained from Monte Carlo simulations and are further discussed in Chapter 5.

The uncertainty on the proper decay time, σ_t, can be expressed as:

$$\sigma_t = \sigma(L^B_{xy}) \oplus t \cdot \frac{\sigma(K)}{K} \tag{2.68}$$

where $\sigma(L^B_{xy})$ is the uncertainty due to vertexing resolution and $\sigma(K)/K$ is the K-factor resolution. Note that the latter uncertainty scales with the decay time t, while the vertexing resolution is independent of t and only adds a constant uncertainty. In order to resolve the fast B_s^0 oscillations σ_t should be smaller than the oscillation

period. Moreover, since the K-factor resolution is significant for semileptonic decays (owing to undetected neutrino), events with small decay time are the most sensitive to oscillations.

2.6.4 Overview of the Mixing Analysis

In a B mixing measurement, the oscillation frequency Δm_q (q = s,d) is extracted from the data using a maximum likelihood method. In the following, we discuss the essential steps for a B_s^0 mixing analysis determining Δm_s. We start with a pure sample of B_s^0 mesons and assume that the lepton tag is always correct. In this case, an event with an opposite-sign lepton pair signals an unmixed event, while a same-sign lepton pair indicates a mixed event. In this case the probabilities for an opposite-sign event $\mathcal{P}_{OS}$ and a same-sign event $\mathcal{P}_{SS}$ are directly related to the mixing probabilities:

$$\mathcal{P}_{SS}(t) = \mathcal{P}_{mix}(t) \text{ and } \mathcal{P}_{OS}(t) = \mathcal{P}_{unmix}(t) \tag{2.69}$$

The mixing probabilities are obtained from Equation 2.48 by neglecting the width difference between the heavy and light mass eigenstates:

$$\mathcal{P}_{unmix/mix}(t) = \frac{1}{2}\Gamma e^{-\Gamma t}(1 \pm \cos\Delta m t) \tag{2.70}$$

The observable asymmetry $\mathcal{A}_{mix}$ is defined as:

$$\mathcal{A}_{mix}(t) = \frac{\mathcal{P}_{unmix}(t) - \mathcal{P}_{mix}(t)}{\mathcal{P}_{unmix}(t) + \mathcal{P}_{mix}(t)} = \cos\Delta m t. \tag{2.71}$$

Next we introduce several effects that we will have to include in a realistic mixing analysis. First, we consider the mixing asymmetry $\mathcal{A}_{mix}$ as a function of the decay time assuming an ideal case with a perfect tagging, ideal proper time resolution, and no background, as shown in Fig. 2.8 (left). Then, we introduce a vertexing resolution

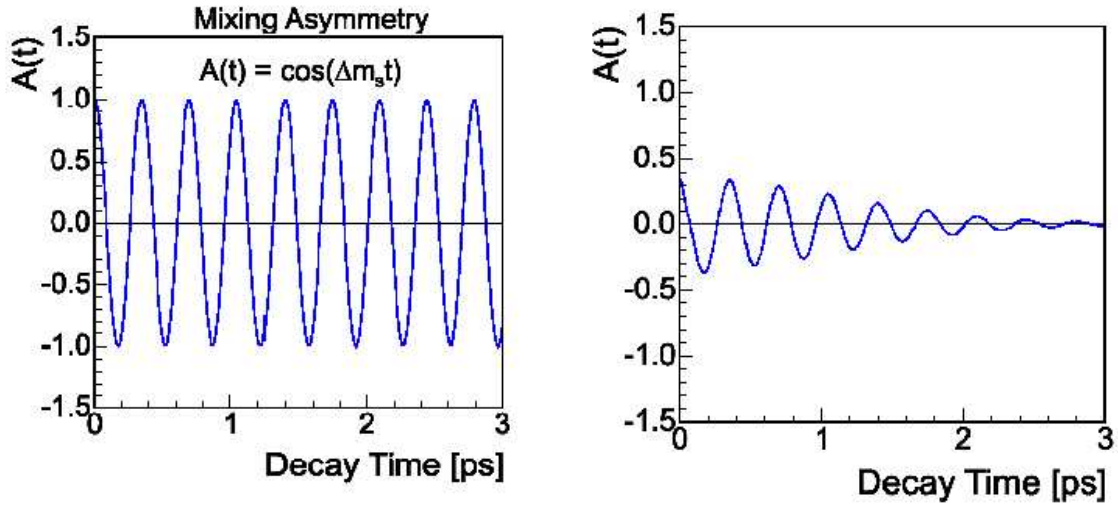

Figure 2.8: On the left is the mixing amplitude in ideal case and effect on mixing amplitude due to finite decay length resolution is shown on right.

function $\mathcal{G}$ which smears the decay time measurement and effectively reduce the amplitude of the oscillation,as shown in Fig. 2.8 (right). The oscillation amplitude is also reduced by mistag effects and the resulting amplitude is proportional with the tagging dilution $\mathcal{D}$. The effect of mis-tagging is exemplified in Fig. 2.9 (left). The effect of introducing a momentum resolution, for example through a K-factor distribution $\mathcal{F}(K)$ is also considered and shown in Fig. 2.9 (right).

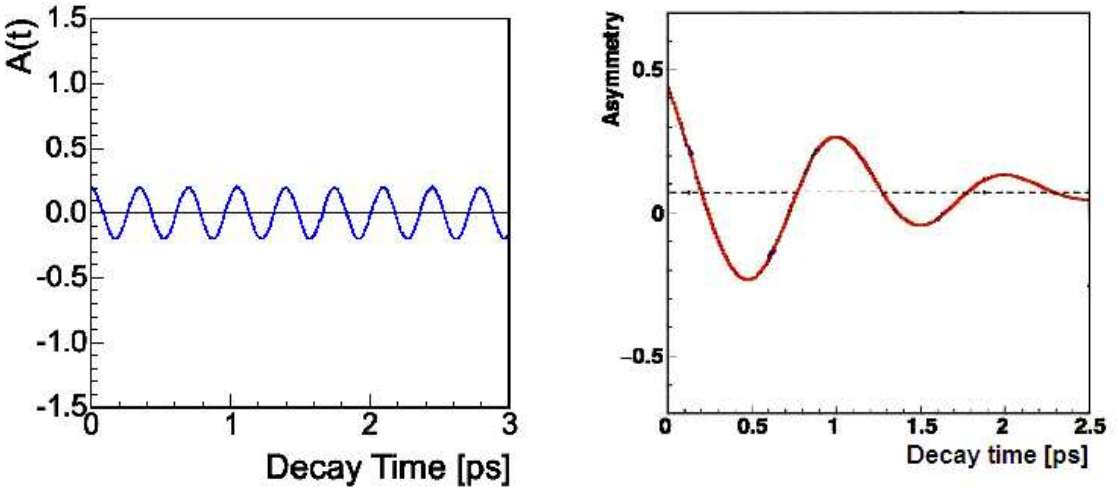

Figure 2.9: Effect on amplitude due to flavor mis-tagging (left) and combining all the effects (right)

The event selection efficiency might not be constant as a function of the decay time. We account for the the lifetime distribution bias by introducing an acceptance function ϵ. Including all these effects, the opposite/same-sign probability would be modified as

$$\mathcal{P}_{OS/SS}(t^*) \sim \int dK K\epsilon(Kt^*) \int \frac{1}{2}\Gamma e^{-\Gamma t}(1 \pm \mathcal{D}\cos(\Delta m_s t))\mathcal{G}(t'-t,\sigma)dt|_{t'=Kt^*}. \quad (2.72)$$

In real measurement there will be background such as combinatorial background under a charm signal. We define $\mathcal{P}^{sig}_{SS}$ and $\mathcal{P}^{sig}_{OS}$ as $\mathcal{P}_{SS}$ and $\mathcal{P}_{OS}$ in Eq. 2.72 and obtain

$$\begin{aligned} \mathcal{P}_{SS}(t) &= (1-f_{bkg})\mathcal{P}^{sig}_{SS}(t) + f_{bkg}f_{SS}\mathcal{P}^{bkg}(t), \quad (2.73)\\ \mathcal{P}_{OS}(t) &= (1-f_{bkg})\mathcal{P}^{sig}_{OS}(t) + f_{bkg}f_{OS}\mathcal{P}^{bkg}(t) \end{aligned}$$

where f_{bkg} is the fraction of the background in a given sample, f_{SS} is the fraction of the same-sign events in the background, while $\mathcal{P}^{bkg}$ is the probability function that describes the proper time t distribution of the background events. To extract the value Δm_s of the oscillation frequency, the following likelihood function is minimized:

$$\mathcal{L} = -\sum_{SS} ln\mathcal{P}^{SS}(t^*) - \sum_{OS} ln\mathcal{P}^{OS}(t^*). \quad (2.74)$$

The statistical significance $\mathcal{S}$ of a B^0_s oscillation signal can be approximated [20] as,

$$\mathcal{S} \approx \sqrt{\frac{1}{2}} f_{sig}\mathcal{D}e^{-(\Delta m\sigma_t)^2/2} = \sqrt{\frac{\epsilon\mathcal{D}^2}{2}}\frac{S}{\sqrt{S+B}}e^{-(\Delta m\sigma_t)^2/2}, \quad (2.75)$$

where N and f_{sig} are the number of tagged candidates and the fraction of the signal in the selected sample and σ_t is the resolution on proper decay time. S and B are the the numbers of signal and background events. The sensitivity $\mathcal{S}$ decreases rapidly as Δm increases. This dependence is controlled by σ_t which means that excellent

proper time resolution is needed to explore high frequencies of B_s^0 oscillations. The sensitivity time increases with the tagging power $\epsilon\mathcal{D}^2$, the signal fraction and the total number of events.

2.6.5 The Amplitude Method

The amplitude method [20] is used in the B_s^0 mixing analysis to set limits on Δm_s. This method is also very handy when combining the results from the different experiments. Though both the amplitude method and the likelihood method is being used in the current analysis to search for B_s^0 mixing signal, here only the amplitude method is discussed. An amplitude $\mathcal{A}$ is introduced in the expressions describing the mixed and unmixed probabilities:

$$\mathcal{P}_{unmix}^{B_s^0} = \frac{1}{2}\Gamma e^{-\Gamma t}(1 + \mathcal{A}\cos\Delta m_s t) \tag{2.76}$$

, and similarly for the mixed sample:

$$\mathcal{P}_{mix}^{B_s^0} = \frac{1}{2}\Gamma e^{-\Gamma t}(1 - \mathcal{A}\cos\Delta m_s t). \tag{2.77}$$

In the amplitude method, a B_s^0 oscillation amplitude $\mathcal{A}$ and its error $\sigma_{\mathcal{A}}$ are expected as a function of a fixed test value of Δm_s using a likelihood method in analogy to Eq. 2.74 based on the physics functions defined in Eqs. 2.76 and 2.77. To a very good approximation, the statistical uncertainty on $\mathcal{A}$ is Gaussian and equal to the inverse of the significance $1/\mathcal{S}$ defined in Equation 2.75. If Δm_s equals its true value Δm_s^{true}, the amplitude method expects $\mathcal{A} = 1$ within the total uncertainty $\sigma_{\mathcal{A}}$. If Δm_s is tested far from its true value, a measurement consistent with $\mathcal{A} = 0$ is expected. A value of Δm_s can be excluded at 95% Confidence Level if $\mathcal{A} + 1.645\sigma_{\mathcal{A}} \leq 1$.

Because of proper time resolution, the quantity $\sigma_{\mathcal{A}}(\Delta m_s)$ is an increasing function of Δm_s. It is therefore expected that individual values of Δm_s can be ex-

cluded upto Δm_s^{sens}, where Δm_s^{sens} is called the sensitivity of the analysis defined by $1.645\sigma_{\mathcal{A}}(\Delta m_s^{sens}) = 1$. If no signal is observed, a lower limit is set with 95% Confidence Level at the mixing frequency for which $\mathcal{A} + 1.645\sigma_{\mathcal{A}} = 1$.

An interesting feature of the amplitude methods is that the result from different analysis and experiments can be combined by simple avearging of different amplitude spectra (after accounting for correlations between the systematic errors). The com-

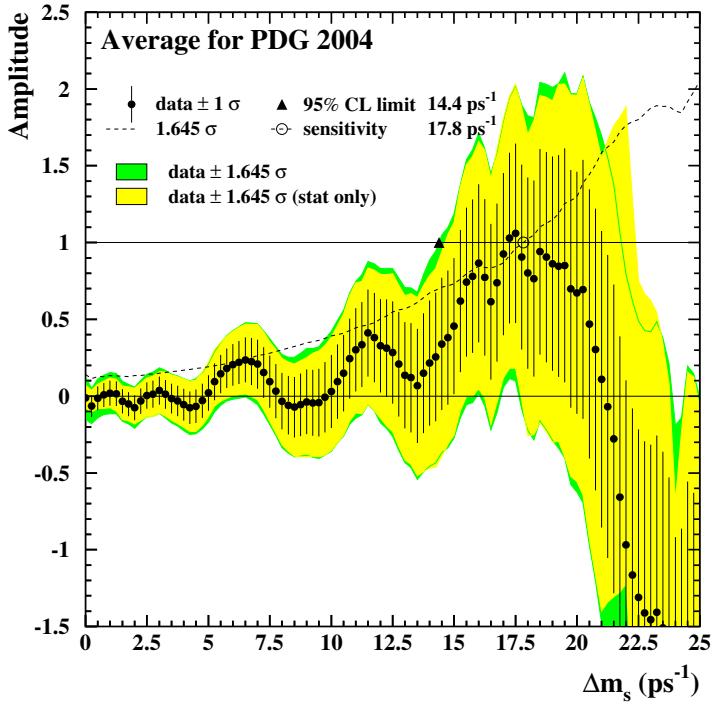

Figure 2.10: World average amplitude for B_s^0 which includes all the published results up to 2004.

bined measurements of the B_s^0 oscillation amplitude as a function of Δm_s, including all published results excluding the results from RunII of the Tevatron provide a lower limit on the B_s^0 mixing frequency of $\Delta m_s > 14.4\ ps^{-1}$ at 95% Confidence Level with a sensitivity of 17.8 ps^{-1} as shown in Fig. 2.10 and the fit to the CKM triangle can be seen in Fig. 2.11. This picture has changed completely after including the results from the RunII of the Tevatron and is discussed in detail in Chapter 5 and Chapter

6.

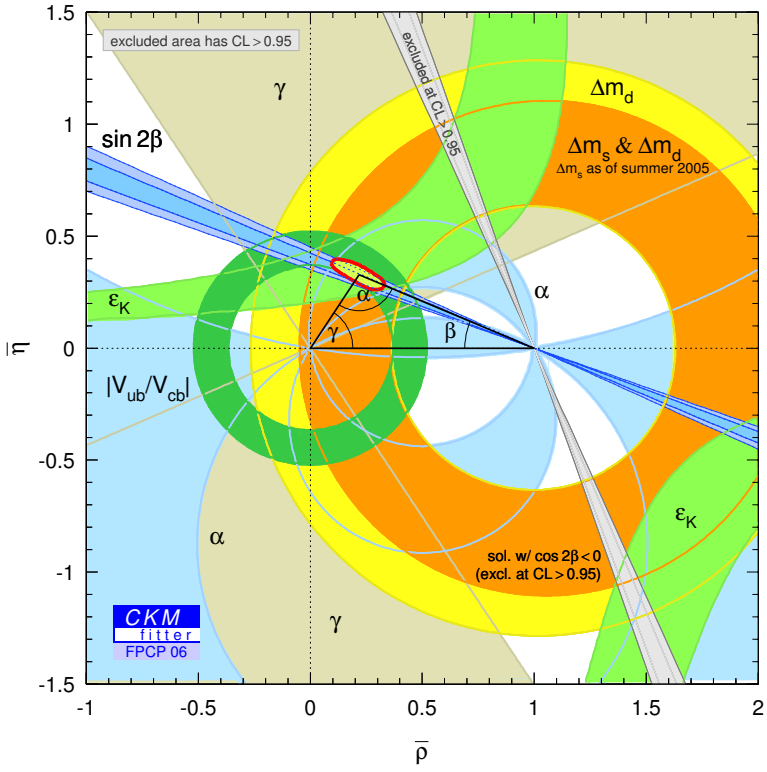

Figure 2.11: Fit to the CKM triangle using all the results up to summer 2005.

Chapter 3

Experimental Apparatus

3.1 Experimental Framework

Fermilab is the home of the world's most powerful particle accelerator at present, the Tevatron. The protons and antiprotons inside the Tevatron collide head on at two collision points. The DØ detector is situated at one of these collision points and the Collider Detector at Fermilab (CDF) being at the other point. The Fermilab accelerator complex has a chain of accelerators to produce the world's highest energy particle beams.

The Tevatron accelerator first started colliding 900 GeV proton and antiproton beams in 1985. Run I was undertaken between 1992 and 1996 and produced many important results including the discovery of the top quark [21]. Between 1997 and 2001, both the accelerator complex (see Fig. 3.1) and the two detectors underwent major upgrades, mainly aimed at increasing the luminosity of the accelerator and gathering data sample of the order of 8 fb^{-1} or more, known as RunII of the Tevatron. In RunII, the Tevatron is operating at a center of mass energy of 1.96 TeV. At present, the Tevatron accelerates 36 bunches of protons and antiprotons, whereas the previous version of the accelerator operated with only 6 bunches. Consequently, the time between bunch crossings has decreased from 3.5 μs for the previous version to 396 ns

for the current machine. The instantaneous luminosity was $\sim 1 - 2 \times 10^{31} cm^{-2} s^{-1}$ for Run I, with DØ collecting around 120 pb^{-1} of data. Despite the success of Run I, the limited integrated luminosity coupled with the low production cross sections for interesting processes limited the physics capability. Here we describe the main components of the upgraded accelerator complex in brief and then we describe the components used to identify and measure properties of the particles produced as a result of collision in the Tevatron.

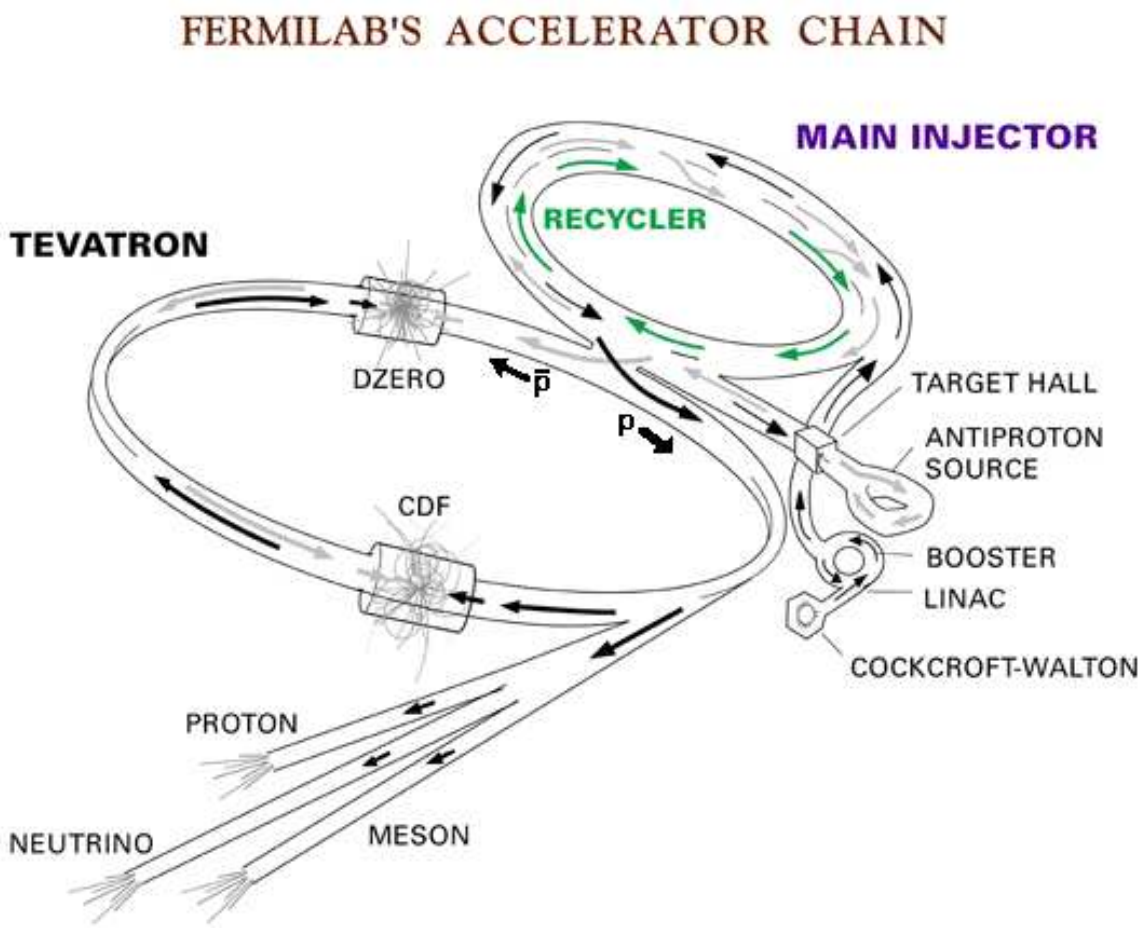

Figure 3.1: Fermilab Accelerator Complex

.

3.1.1 The Tevatron

Tevatron is presently the world's highest energy particle accelerator. The first stage of the acceleration is provided by the Cockroft-Walton preaccelerator. Inside this device, gaseous hydrogen is ionized to create H^- ions, which are accelerated to 750 keV energy. These H^- ions then enter a linear accelerator, the Linac [22], approximately 500 feet long, where they are accelerated to 400 MeV. A series of "kicks" from Radio Frequency (RF) cavities produce the acceleration in the Linac. The oscillating electric field of the RF cavities groups the ions into bunches. The next stage is the Booster, but before that, these ions pass through a carbon foil which removes the two electrons, leaving only the protons.

The Booster, a circular synchrotron [22] 74.5 m in diameter is located approximately twenty feet below the ground and uses magnets to bend the beam of protons in circular path. The intensity of the proton beam is increased by injecting new protons into the same orbit as the circulating ones. The protons travel around the Booster about 20,000 times, acquiring about 500 keV of Kinetic energy each time and so the protons are finally accelerated to an energy of 8 GeV. Protons are then injected into Main Injector [23], which operates at 53 MHz. It accelerates protons from 8 GeV to 150 GeV to be injected into the Tevatron. It also produces 120 GeV protons which are used for antiproton production and then it receives the antiprotons from antiproton source and accelerates them to 150 GeV before they are finally injected into the Tevatron.

Antiprotons are produced by hitting the nickel target with the 120 GeV protons from the Main Injector. In the collisions, about 20 antiprotons are produced per one million protons, with a mean kinetic energy of 8 GeV. The antiprotons are focused by a lithium lens and separated from other particle species by a pulsed magnet. Before the antiprotons can be used in the narrow beams needed in the collider, the differences in the kinetic energy between the different particles need to be reduced.

Since this process reduces the spread of the kinetic energy spectrum of the beam, it is referred to as "cooling" the beam. New batches of antiprotons are initially cooled in the Debuncher synchrotron, collected and further cooled using stochastic cooling [24] in the 8 GeV Accumulator synchrotron.

The principle of stochastic cooling is to sample particle motion with a pickup sensor and correct its trajectory later with a kicker magnet. In reality, the pickup sensor samples the average motion of particles in the beam and corrects for the average. Integrated over a long period of time, this manifests itself as a damping force applied onto individual particles which evens out the kinetic energies.

The antiprotons are then stored in the Accumulator ring and when a sufficient number ("stack") has been obtained, they are sent to the Main Injector for further acceleration before being fed into the Tevatron. It takes about 15-20 hours to build up a stack of $100E30$ antiprotons. The availability of the antiprotons is the limiting factor for attaining high luminosities. Recently, a new technique "Electron cooling" [25] for cooling the antiprotons has been adopted which is supposed to increase the stacking ability.

Not all the antiprotons in a given store are used up by the collisions at the end of the store. An Antiproton Recycler is used to recycle the unused antiprotons and reusing them in the next store and thus significantly reducing the stacking time. The task of the Recycler is to receive the leftover antiprotons from a Tevatron store, cool them and re-integrate them into the stack. The last and final stage of the accelerator chain is the Tevatron. It receives 150 GeV protons and antiprotons from the Main Injector and accelerates them to 980 GeV.

The protons and antiprotons accelerate in opposite directions inside the Tevatron. There are typically 36 bunches of protons and antiprotons arranged in three groups of 12 super bunches separated by 2 μs. The beams are brought to collisions at two collision points, B0 and DØ. At these two points, the two collider detectors, the

Parameters	Values
Energy $p\overline{p}$ (GeV)	980
Proton bunches	36
Protons/bunch	2.7×10^{11}
Antiproton bunches	36
Antiprotons/bunch	$\times 10^{10}$
Bunch spacing (ns)	396
Peak luminosity ($cm^{-2}s^{-1}$)	1.5×10^{32}

Table 3.1: Tevatron Operating Parameters.

Collider Detector at Fermilab (CDF) and DØ detector are located. Quadrupole magnets squeeze the beams into a cross sectional area of $\sigma_a \sim 5 \times 10^{-5} cm^2$ such that the beams collide in the geometrical center of the two detectors. The instantaneous luminosity can be expressed as

$$\mathcal{L} = \frac{f_{rev} N_B N_p N_{\overline{p}}}{2\pi(\sigma_p^2 + \sigma_{\overline{p}}^2)} F(\sigma_l/\beta^*), \tag{3.1}$$

where f_{rev} is the revolution frequency, N_B is the number of bunches, $N_{p(\overline{p})}$ is the number of protons(antiprotons) per bunch, and $\sigma_{p(\overline{p})}$ is the protons(antiprotons) rms beam size at the interaction point. F is a form factor which corrects for the bunch shape and depends on the ratio of σ_l, the bunch length to β^*, the beta function, at the interaction point. The beta function is a measure of the beam width, and it is proportional to the beam's x and y extent in phase space. Table 3.1 lists some important operating parameters for the Tevatron.

3.2 The DØ Detector

The DØ detector [26] is a general multipurpose collider detector. It has a typical cylindrical structure common to many modern high energy physics experiments. The overview of the detector is shown in Fig. 3.2. Because the beams in the Tevatron are equal in energy, the detector is symmetrical about the interaction point and covers

nearly all 4π surrounding the interaction region. The detector consists of three major subsystems:

- Central tracking detectors.
- The Calorimeter.
- The Muon Detector.

Figure 3.2 shows a schematic view of the Run II DØ detector. The tracking detectors are positioned closest to the interaction point and have the finest segmentation. They are designed to measure the three dimensional trajectories of the charged particles passing through them. The magnetic field bends the trajectory of the charged particles and allows a measurement of their momenta. The tracking detectors are built out of low Z material to introduce as little interaction as possible while still detecting their presence. The tracker is surrounded by the Calorimeter. This detector measures the energy of the particles and is constructed out of high Z material to absorb most of the particles entering it. Since muons have much more penetrating power and can escape the calorimeter, another detector has been put outside the calorimeter.

3.3 Coordinate system

We use a right handed coordinate system in which the z-axis is along the proton direction and y-axis points vertically upward and x-axis points horizontally towards the center of the ring, as shown in Fig. 3.3. The angles ϕ and θ are azimuthal and polar angles, respectively, with $\theta = 0$ along the beam pipe. Because of the approximate axial symmetry of the detector, it is convenient to define the cylindrical coordinates r and ϕ.

$$r = \sqrt{(x^2 + y^2)} \tag{3.2}$$

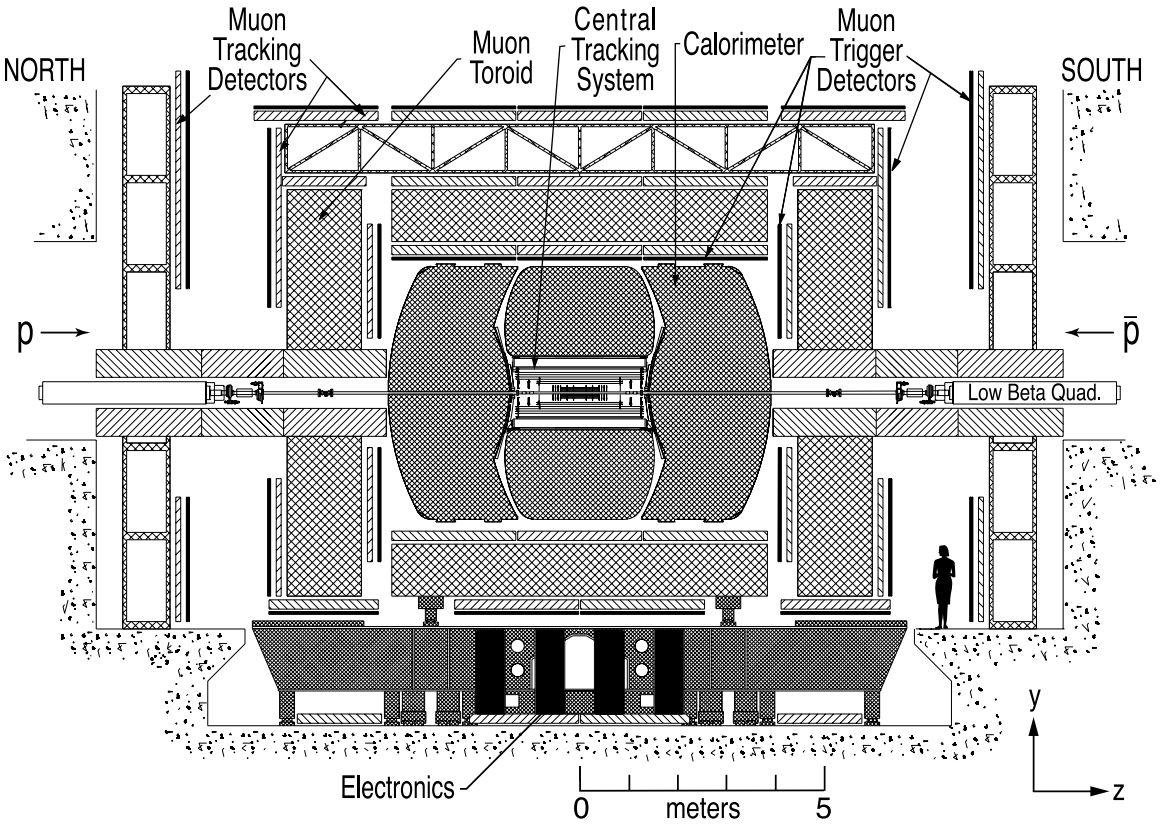

Figure 3.2: Side view of the DØ detector [26].

$$\phi = \tan(\frac{y}{x}) \tag{3.3}$$

The r coordinate denotes the perpendicular distance from the z axis. Since most of the particles of interest are ultra-relativistic it is convenient to use η, or the pseudo-rapidity, in place of θ. The pseudo-rapidity η is related to the polar angle by:

$$\eta = -\ln[\tan(\frac{\theta}{2})], \tag{3.4}$$

and approximates the true rapidity,

$$y = \frac{1}{2}\ln[\frac{E + p_z}{E - p_z}] \tag{3.5}$$

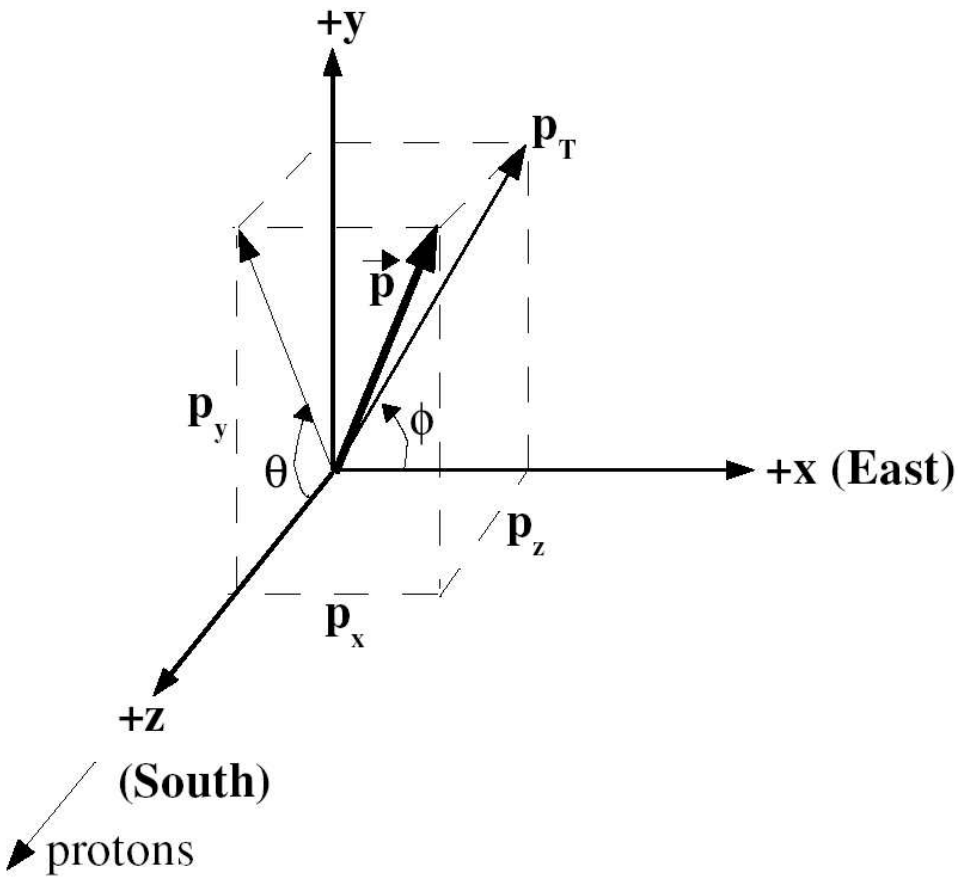

Figure 3.3: DØ coordinate system.

for infinite angles in the limit that $(\frac{mc^2}{E}) \rightarrow 0$, where E is the energy of the particle and P_z its longitudinal momentum. Rapidity is convenient for two regions: Rapidity intervals are Lorentz invariant and particle multiplicity is approximately constant in rapidity. Since some particles escape down the beam pipe and the initial momentum of the interacting particles are not known, we measure the momentum and energy in the direction perpendicular to the beam axis, i.e. transverse momentum (p_T) and transverse energy (E_T), defined by

$$p_T = p \sin\theta, \text{ and } E_T = E \sin\theta. \tag{3.6}$$

Collisions do not always occur at the center of the detector because of the long

bunch length $\sim$ 30 cm in Z, so when reconstructing the direction and transverse momentum of the final state objects a correction in the Z position is applied, see Fig. 3.4. However, for discussing the position of the detector it is most convenient to speak of the detector η. Unless otherwise noted, when discussing detector elements the η referred to will be the detector η. Similarly, when referring to the reconstructed physics objects such as electrons, jets, and muons the η referred to is the physics η which is simply the η of the object with respect to the hard scattering event vertex.

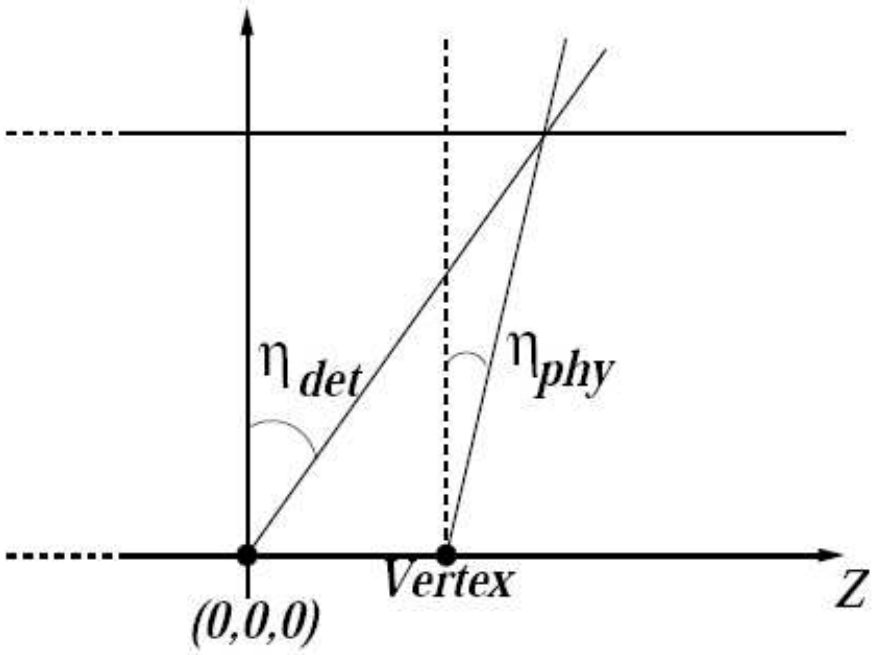

Figure 3.4: Difference between Detector and Physics η.

3.4 Central Tracking System

Excellent tracking in the central region is necessary for studies of b physics, top quark, etc. The tracking system is the backbone of the b physics program at DØ. The central tracking system consists of the Silicon Microstrip Tracker (SMT) and the Central Fiber Tracker (CFT) surrounded by a solenoidal magnet. A schematic

view of the central tracking system is shown in the figure 3.5. Working together, the

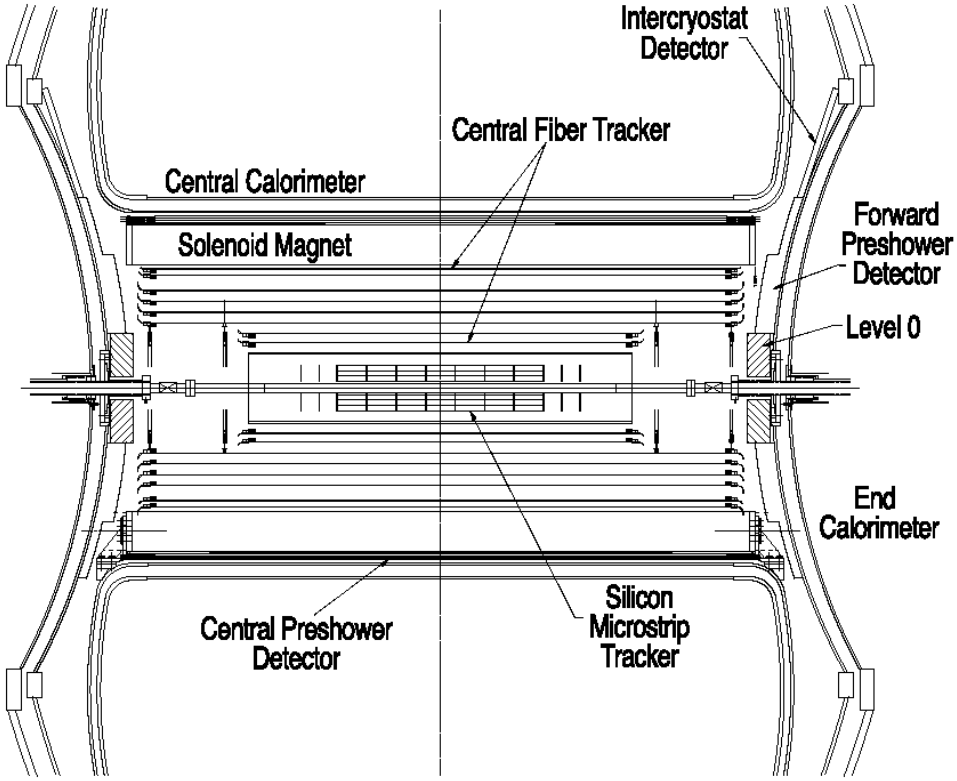

Figure 3.5: Schematic of the central tracking system.

two detectors locate the primary interaction vertex with a resolution of about 35 μm along the beamline.

Charged particles interact with the tracking detectors and leave a pattern of hits in the various layers of the detectors. From these hits, a track can be reconstructed representing the trajectory of the charged particle. Since the entire tracking region is inside a highly uniform magnetic field, the trajectories of charged particles are curved. By measuring the curvature of the track, it's momentum can be precisely estimated.

There is another detector called Preshower located between inner tracking system and calorimeter. Preshower detectors function as calorimeters as well as tracking detectors. These detectors aid in electron identification and background rejection during both online triggering and offline reconstruction.

3.4.1 Silicon Microstrip Tracker (SMT)

The SMT provides both tracking and vertexing over nearly the full η coverage of the calorimeter and muon systems. An isometric view of the SMT is shown in Figure 3.6. With a long interaction region, it is difficult to deploy detectors such that the tracks

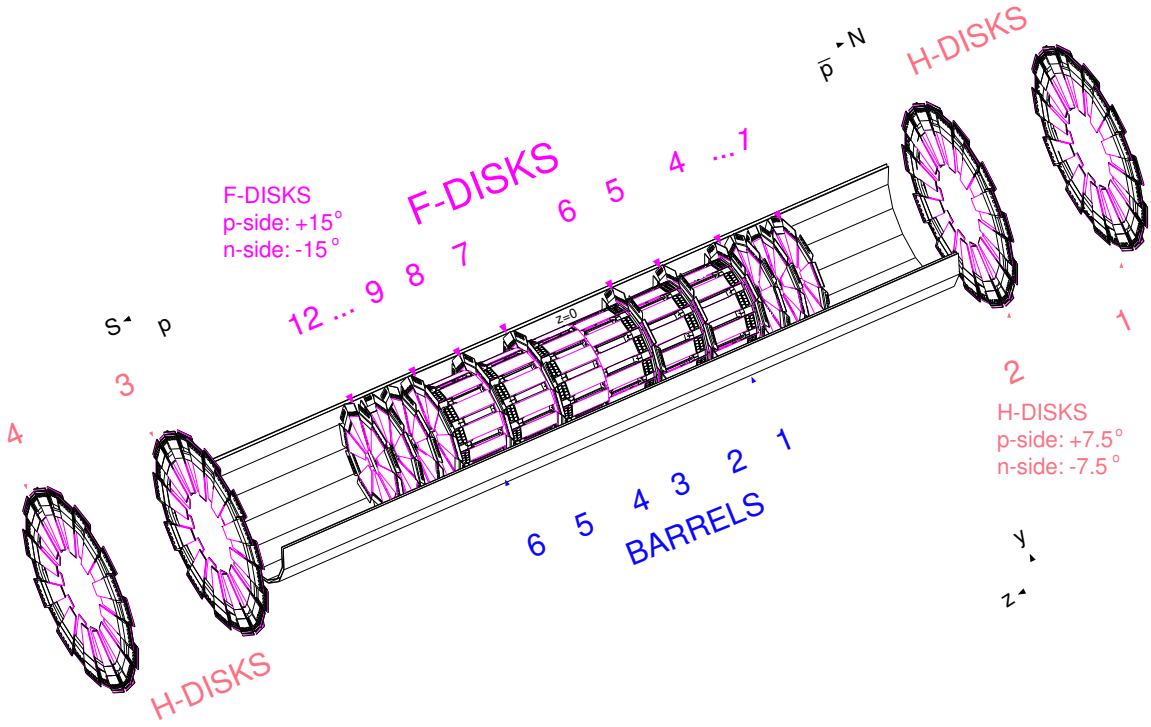

Figure 3.6: Isometric view of SMT.

are generally perpendicular to detector surfaces for all η. This led to the design of barrel modules interspersed with the disks in the center and assemblies of disks in the forward regions. The detector has six barrels in the central region. Each barrel has four silicon readout layers, two double sided layers, and two single sided layers. The silicon modules installed in the barrels are called "ladders". Layers 1 and 2 have twelve ladders each; layers 3 and 4 have twenty-four ladders each, for a total of 432 ladders.

The active part of the silicon sensor is segmented into a series of parallel strips. The barrel module detectors are 12 cm long with 50 μm strip pitch. The double

sided detectors have axial strips parallel to the beam on one side while the strips on the other side are placed at an angle (either at 2^0 or 90^0) with respect to the beam. The pitch strips are chosen so that the position resolution would be approximately 10 microns. The length of the barrel region is dictated by the fact that the bunches have a wide distribution along the beam axis with $\sigma_z = 30\ cm$.

The detectors are fabricated on n-type silicon wafers that are 300 μm thick as shown in Fig. 3.7. The strips are formed by p^+ implants along the length of the detector. A thin dielectric layer between the strips and an aluminium coating forms a capacitor which AC couples the detector to the readout electronics. A radiation hard polysilicon resistor is used to bias the sensor. The sensors operate essentially as reverse biased diodes. When a charged particle passes through the sensor, electron/hole pairs are created. The electrons are then accelerated toward the positive voltage. The p^+ silicon is separated from the aluminium readout strip by a silicon oxide layer which forms a capacitor. As electrons rush towards the p^+ region, an image charge is formed on the aluminium which is collected and stored in an analog pipeline in a readout chip in an array of switched capacitors. The signal is buffered, digitized, and readout by a chip which is bonded onto the sensor.

The detector is read out by 128-channel readout chips. These chips are called SVXIIe chips and are designed to work with double sided detectors and can accept both positive and negative currents as input signals. The chips are mounted on a high density interconnect or HDI. Data from HDIs are sent from the sequencers to VME readout buffer (VRB) memories via optical link fibers. The VRB controller (VRBC) receives trigger data from the SCL and uses that information to control the operation of the VRBs. A single board computer is resident in the readout crate to collect and process detailed diagnostic information.

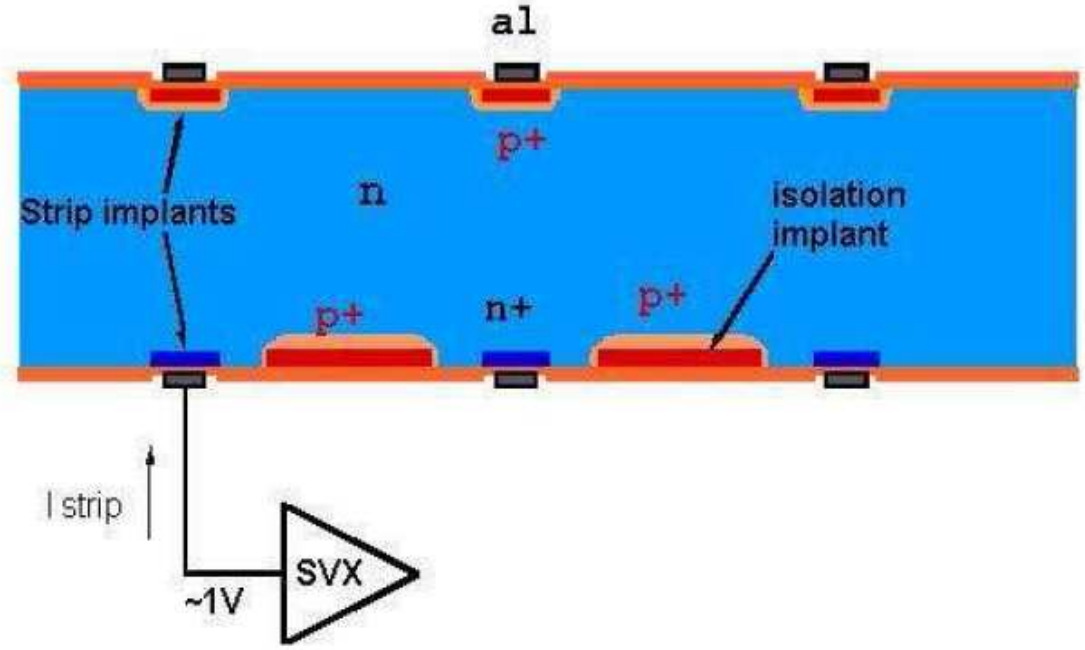

Figure 3.7: Schematic diagram of a silicon microstrip detector

.

3.4.2 Central Fiber Tracker

The CFT consists of scintillating fibers mounted on eight concentric support cylinders and occupies the radial space from 20 to 52 cm from the center of the beampipe. Figure 3.8 shows a cross section of the CFT. The two innermost cylinders are 1.66 m long; the outer six cylinders are 2.52 m long. Each cylinder supports one doublet layer of fibers oriented along the beam direction (z) and a second doublet layer at a stereo angle of $+3^0$ (u) or -3^0 (v). Doublet layers with the fibers oriented along the beam axis are referred to as the axial layers, while the doublet layers oriented at small angles are referred to as the stereo layers. The scintillating fibers are 860 microns thick and between 1.7 - 2.6 meters long. They are organized and mounted in 128 fiber ribbons which consists of two singlet layers. Scintillating fibers are coupled to clear fibers waveguides which carry the scintillation light to visible light photon counters (VLPCs) for read out.

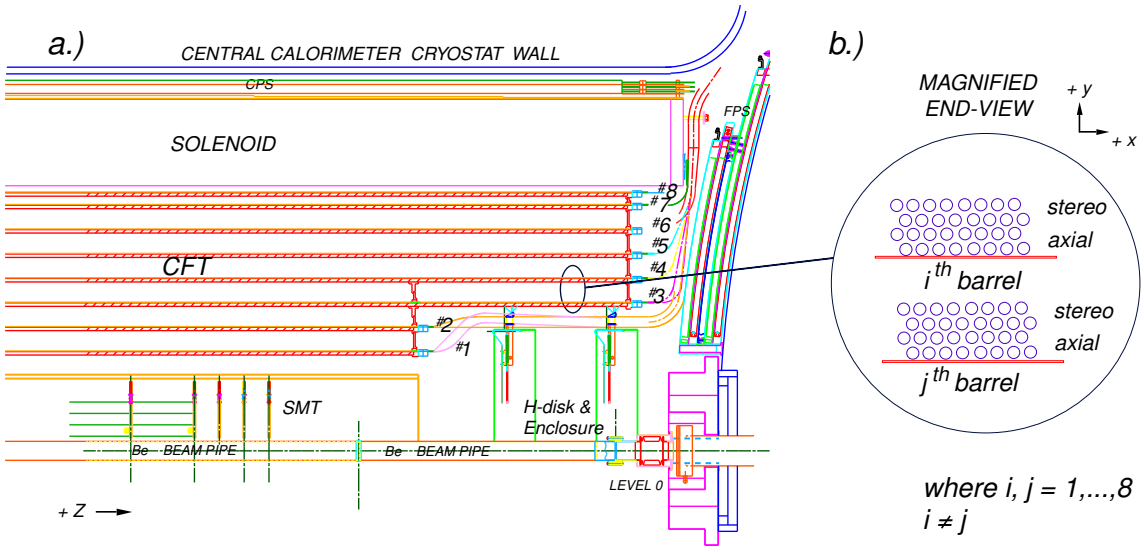

Figure 3.8: Cross Section view of the CFT detector

.

The scintillating fibers, including cladding, are $835\mu m$ in diameter and 1.66 or 2.52 m in length. The fibers are 99% polystyrene (by weight) and contain two organic scintillating dyes: Paraterphenyl (PHP) and 3-hydroxyflavone (3HF) [27]. The polystyrene absorbs energy from the ionizing radiation incident upon it. The relaxation time of polystyrene absorbs energy from the ionizing radiation incident upon it. The relaxation time of polystyrene is slow so the organic dye PHP is added to the fiber. Through dipole interactions the PHP molecules are excited which then decay promptly back to their ground state radiating a photon within a few nanoseconds.

However, since the PHP emits light with a very short wavelength ($\sim 340\ mm$) the optical path length is very short, on the order of a few hundred microns. Therefore, a second dye (3HF) is used as wavelength shifter to absorb the light from the de-excitation of the PHP molecules and emit photons with a longer wavelength of $\sim 530\ nm$. This second dye was chosen since the optical path length in polystyrene is maximized in this region and is on the order of several meters. The long optical path length allows the scintillation light to travel the necessary distance to be detected.

The light from the scintillating fiber is observed only at one end while the other

end of the fiber is coated with a reflecting material providing a reflectivity of 85 to 90%. The light generated by the passage of charged particles through the scintillating fibers is converted into electrical signals by the VLPCs. These VLPCs are capable of detecting a single photon, provide fast response, have excellent qantum efficiency greater than 75%, and have high gain.

3.4.3 Solenoid

The superconducting solenoidal magnet was designed to optimize momentum resolution, $\frac{\Delta p_T}{p_T}$, and tracking pattern recognition. It surrounds the tracking region and creates a highly uniform axial magnetic field of 2 Tesla. The solenoid is wound with two layers of superconductor and is 2.73 m in length and 1.42 m in diameter. Both conductors are made up of superconducting Rutherford-type cable of multifilamentary Cu:NbTi strands stabilized with pure aluminium and operates at 4.7 K. They run at a current of $4749A$. The magent stores $5.3MJ$ of energy. To maximize the field uniformity inside the bore of the magnet, current density in the windings is larger at the ends of the coil. The magnet polarity is reversed from time to time using a $5000A$ DC mechanical motorized polarity reversing switch and a switch controller. This is being done to run the detector for equal amount of time in each polarity and maintaining the charge asymmetry distribution.

3.4.4 Preshower Detectors

Particles to loose significant amount of energy in the solenoid magnet. It is convenient to describe the amount of material in terms of the amount of energy a particle looses as it passes through it. The radiation length X_0 is defined as the mean distance over which an electron loses all but $\frac{1}{e}$ of its energy [1]. The material in the solenoid amounts to about 0.8 to 2.0 X_0 depending on the incident angle of the particles. The particles coming out at large η will have to traverse a longer path and hence would

interact with more matter than the particle at normal incidence or smaller η.

To take into account the effect of the extra material of the solenoid, preshower detectors are installed in the space between the magnet and calorimeter. Preshower detectors aid in electron identification and background rejection during both online triggering and offline reconstruction. They function as calorimeters as well as tracking detectors, enhancing the spatial matching between tracks and calorimeter showers [28]. The detectors can be used offline to correct the electromagnetic energy measurement of the central and end calorimeters for losses in the solenoid and upstream materials, such as cables and supports.

The Central Preshower detector (CPS) covers the region $|\eta| < 1.3$ and is located between the solenoid and central calorimeters. The two Forward Preshower Detectors (FPS) cover $1.5 < |\eta| < 2.5$ and are attached to the faces of the end calorimeters. The detectors consist of lead absorbers and triangular strips of plastic scintillator. Since the triangles are interleaved, there is no dead space between strips and most tracks traverse more than one strip, allowing for strip-to-strip interpolations and hence improved position measurement. Additional lead of varying thickness surrounds the solenoid to make the radiation length approximately 2.0 X_0 for all particle trajectories. Embedded at the center of each triangular strip is a wavelength-shifting fiber which collects and carries the light to the end of the detector. At the readout end, the fibers are grouped into bunches of sixteen and potted into connectors for transition to clear light-guide fibers. Light is transmitted via the clear fibers to VLPC pixels for readout.

The CPS consists of three concentric cylindrical layers of triangular scintillator strips and is located in the nominal 5 cm gap between the solenoid and the central calorimeter. Between the solenoid and the CPS is a lead radiator of approximately 1 radiation length thickness and 96" long, covering $|\eta| < 1.31$. One layer is oriented parallel to the beam while the other two layers are oriented at a stereo angle of

$+23.77^0$ and -24.01^0. Each layer contains 1280 strips.

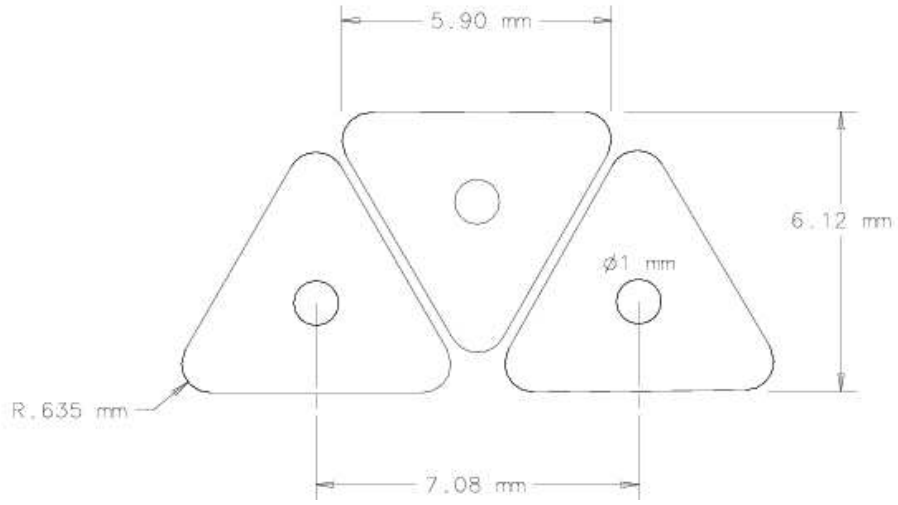

Figure 3.9: Cross section view of the Preshower detector.

The FPS detectors are made up of two layers, at different z, of a double layer of scintillator strips. A 2 X_0 thick lead stainless steel absorber separates the two layers. The upstream layers are known as the minimum ionizing particle, or MIP, layers while the downstream layers behind the absorbers are called the shower layers. All charged particles passing through the detector will register a minimum ionizing hit in the MIP layer, allowing measurement of the location of the track.

3.5 The Calorimeter

Calorimeter detectors are designed to accurately measure the energies of the electromagnetic and hadronic objects. They are crucial for the identification of electrons, photons and jets as well as for inferring the presence of neutrinos and other non-interacting particles from the transverse momentum imbalance. This measurement is made by inducing interactions with incident particles via the material of the calorimeter, creating showers of secondary particles which lose energy (through ionization, excitation etc.) in the calorimeter's active medium. A measurement of a particle's

total energy is made when the showering process is fully contained.

Electromagnetic (EM) and Hadronic (HAD) objects shower differently in the calorimeter, allowing for their identification and as well as an energy measurement. For EM objects (electrons and photons), the energy loss is dominated via two processes : pair production ($\gamma \rightarrow e^+e^-$) and bremsstrahlung[1] ($e \rightarrow e\gamma$). As a result of successive interactions[2] of these two processes, an electromagnetic shower develops. For each successive interaction the number of secondary particles increases while the average energy per particle decreases. Collecting and measuring these secondary particles gives insight into the original EM object's energy (E_0) since the energy of the original particle drops exponentially:

$$E(x) = E_0 e^{-x/X_0} \tag{3.7}$$

where x is the distance traveled and X_0 is the radiation length.

Calorimeters fall into two categories :

- Electromagnetic (EM) Calorimeters
- Hadronic (HAD) Calorimeters

It has to be noted here that although the hadronic showers are dominated by nuclear interactions, they also contain EM shower components, making the determination of hadronic showers more complicated, since the EM part has to be accounted for differently. These two types of showers differ also in relative size. For a given energy of an incident particle, a hadronic shower tends to be larger than the EM.

The different depth (in the radially outward direction) for the two types of showers is reflected in the designs of the calorimeters for a general purpose collider detector.

[1]Emission of a photon due to the interaction between the Coulomb field surrounding a nucleus a charged particle

[2]For instance, an incident electron loses energy by emitting a photon. The photon converts into an e^+e^- pair, which in turn will lose energy by emitting photons.

The calorimeter consists of two subdetectors : the EM and the HAD calorimeter. The EM calorimeter is the innermost calorimeter and more compact; it encloses the volume closer to the interaction point, while the hadronic calorimeter covers the outer region of the detector.

Although the design of the calorimeter is optimized for both types of showers, there are still some difficulties affecting the energy measurement of showers. The first is that the EM component of the hadronic shower fluctuates in energy. The second is that most of the hadronic energy is converted into excitation or break-up of the nuclei, from which only a fraction will result in detectable ("visible") energy. The above two difficulties affect the ratio of EM and HAD response (e/h), and as a result this ratio is not equal to one. To improve calorimeter performance, attempts have been made to make e/h as close to one as possible by means of compensation. The main idea was to use uranium as the absorber material; this would contribute an additional , i.e., compensating signal due to nuclear fission caused by nuclear excitations. The DØ calorimeter is a compensating calorimeter with e/h=1$\pm$0.02.

3.5.1 DØ Calorimeter

The DØ calorimeter [29] is a compensating, sampling calorimeter with fine segmentation. In a sampling calorimeter, the shower development of the incident particles is periodically sampled via the ionization of an active medium or the use of a scintillator. The DØ Calorimeter uses liquid argon (LAr) as active medium and ^{238}U, stainless steel/copper plates as absorber materials. For the active material, LAr was chosen for several reasons : a) it provides uniform gain over the entire calorimeter, allowing for a channel-to-channel response stable over time and dependent on gap and absorber thickness, b) is highly flexible in segmenting the calorimeter volume into readout cells, c) is radiation hard, and d) is easy to calibrate. For the absorber material uranium was chosen because its high density allows for a compact detector

that contains almost all shower energy while reducing cost. It also improves the e/h ratio.

The need to operate the calorimeter at liquid argon temperatures, along with construction and installation needs (access to the Central Detectors), dictates that the Central Calorimeter (CC) must exist as a separate module from each of the two End Calorimeters (EC-North and EC-South). Each of the three modules (CC, EC-North and EC-South), is placed inside a separate cryostat, which is a vessel containing the calorimeter and the cooling apparatus to maintain the liquid argon at a constant temperature, and is shown in Figure 3.10.

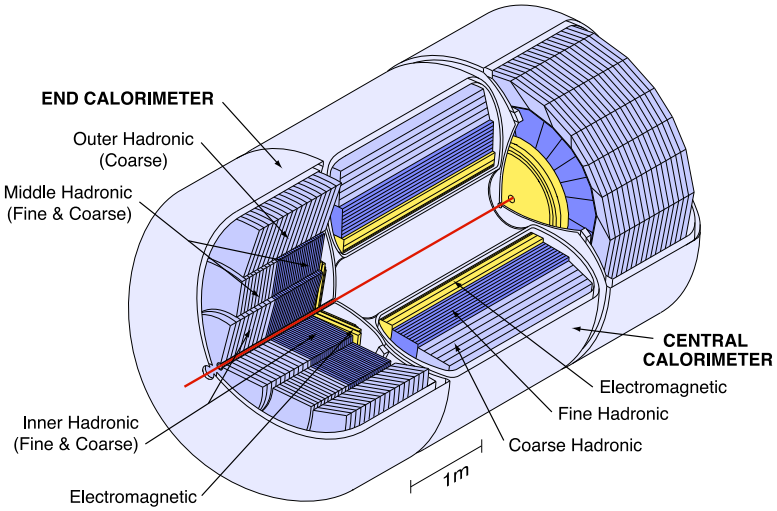

Figure 3.10: Overall view of the DØ calorimeter system [26].

The Central Calorimeter (CC) covers roughly the $|\eta_d| < 1.1$ region and each of the End Calorimeters (EC North and EC South) extend the coverage out to large η_d regions ($1.5 < |\eta_d| < 4.2$) . The CC weighs about 330 tons; each of the EC modules weighs about 240 tons. The calorimeter modules themselves are further segmented into three distinct sections. In order of increasing radius, these are

- electromagnetic (EM) section with relatively thin uranium absorber plates.
- fine-hadronic (FH) with thick uranium plates.

- coarse-hadronic (CH) with thick copper or stainless steel plates.

3.5.2 Electromagnetic Calorimeter

Because EM objects tend to shower over a shorter distance than hadrons, the innermost layers of both the CC and EC are the electromagnetic layers. The electromagnetic calorimeter is 21 radiation lengths deep and it is arranged in four readout layers (EM1 through EM4). These layers extend radially in the CC and along the z-axis in the EC. Each layer uses 3(4) mm thick uranium (^{238}U) absorber plates in the CC (EC). In the central cryostat, the transverse segmentation of the EM calorimeter is $\Delta\eta \times \Delta\phi = 0.1 \times 0.1$ in all layers except the third. The third layer (EM3) is expected to receive the maximum of electromagnetic showers and hence is segmented twice as finely into cells with $\Delta\eta \times \Delta\phi$=0.05 $\times$ 0.05, to allow for more precise location of the EM shower centroid. With this fine segmentation the azimuthal position resolution for electrons with energy above 50 GeV is about 2.5 mm. In the endcap cryostat, the segmentation is 0.1×0.1 except for $|\eta_d| > 3.2$, where the pad becomes too small and the segmentation is increased to 0.2×0.2.

3.5.3 Hadronic Calorimeter

The hadronic calorimeter surrounds the EM calorimeter in both the CC and EC cryostats and are 7-9 interaction lengths deep. The transverse segmentation of all hadronic modules is around 0.1×0.1. It consists of 3 (4) fine hadronic layers (FH) in CC (EC). These use slightly thicker uranium absorber plates, 6 mm thick. Finally, the coarse hadronic layer uses 46.5 mm thick copper (CC) or stainless steel (EC) absorbers. There is one CH layer in CC and three CH layers in EC.

The calorimeter layer depths in terms of their radiation (X_0) and nuclear interaction (λ_0) lengths are summarised in the Table 3.2 .

From the readout point of view, each layer represents a discrete set of readout

	EM (X_0)				**FH** (λ_0)				**CH** (λ_0)		
	EM1	EM2	EM3	EM4	FH1	FH2	FH3	FH4	CH1	CH2	CH3
CC	2	2	7	10	1.3	1.0	0.9		3		
EC	0.3	2.6	7.9	9.3	1.2	1.2	1.2	1.2	3	3	3

Table 3.2: Layer depths in the calorimeter.

cells. These readout cells (one from each layer) are grouped radially along the outward direction (approximate direction of a shower development) to form a $\Delta\eta \times \Delta\phi$ 0.2×0.2 readout geometry referred to as a tower. The readout tower geometry is shown in Figure 3.11. This is a "pseudo-projective" geometry. The term "pseudo-projective" refers to the fact that the centers of cells of increasing shower depth lie on the rays projecting from the center of the detector, but the cell boundaries are aligned perpendicular to the absorber plates.

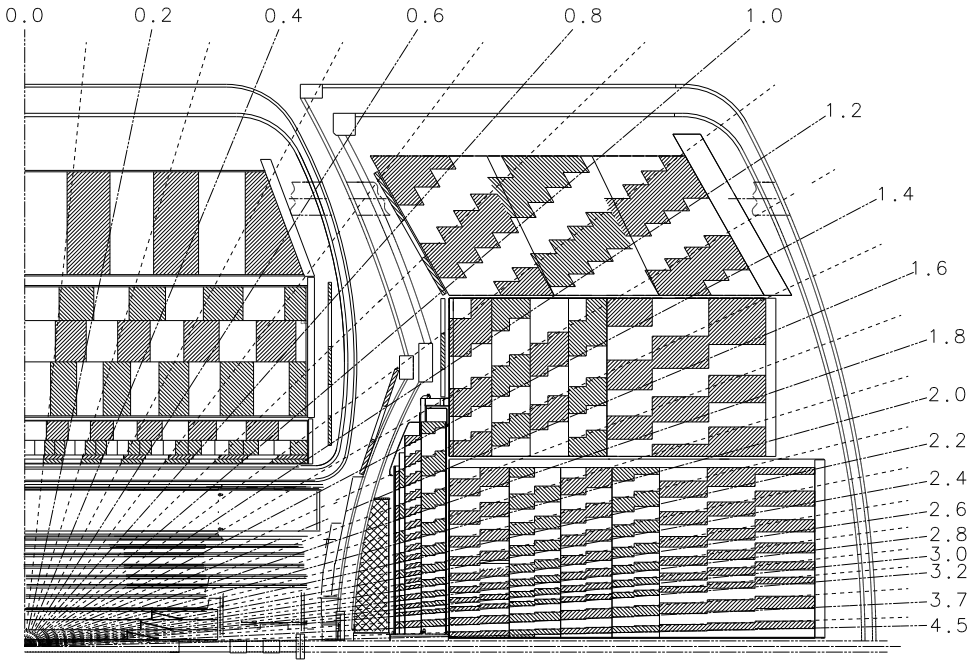

Figure 3.11: A quarter of the calorimeter in the $r - z$ plane of the detector showing the tower geometry.

Each layer consists of alternating layers of absorber plates and signal boards filled with LAr as shown in Figure 3.12. A cell (readout cell) is a combination of several

adjacent unit cells. The signal boards are made of copper readout pad sandwiched by two 0.5 mm thick G-10 insulators. The outer surfaces of the boards are coated with a highly resistive epoxy.

An electric field is created by applying a positive high voltage of 2.0-2.5 keV between the resistive surfaces of the signal boards and the grounded absorber. When a particle enters the calorimeter, it showers inside the absorber plate, and the secondary particles from the shower ionize the argon atoms. The ionization electrons drift toward the signal boards inducing a signal on the copper pad. The gap between the absorber plates is 2.3 mm, and the electron drift time across the gap is about 450 ns.[3] Readout electronics sample the charge on the pad, converting it to an analog signal proportional to the ionization energy recorded. To detect signals that can be very small, signals from several boards in the same η and ϕ regions are grouped together in depth to form a readout cell. The pattern and sizes of the readout cells were determined from

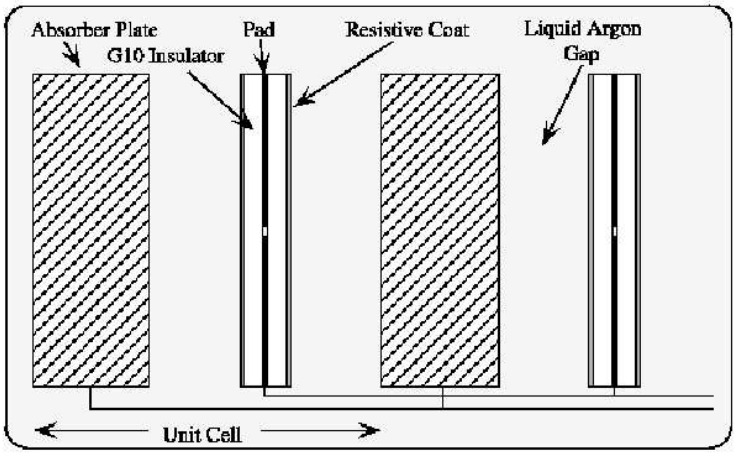

Figure 3.12: Unit Cell in the Calorimeter.

several considerations.

The transverse sizes of the cells were chosen to be comparable to the transverse sizes of showers : ΔR ~0.2 for EM showers and ΔR ~0.5 for hadronic showers.

[3]The gap thickness was chosen to be large enough to observe minimum ionizing particles(MIP) signals and to avoid fabrication difficulties.

Segmentation finer than this is useful in measuring the shape of electrons and jets. Longitudinal subdivision within the EM, fine hadronic and coarse hadronic sections is also useful since the longitudinal shower profiles help distinguish EM objects and hadron jets.

3.5.4 Intercryostat and Massless Gaps Detectors

As evident in Fig. 3.10 and 3.11 there is an uninstrumented region between the CC and EC cryostats ($1.1 < |\eta_d| < 1.4$). The material in this region (cryostat walls, support structures, cabling ...) can participate in shower evolution, and thus can impact jet measurements. To augment the shower sampling in this region, scintillator detectors have been mounted on the EC cryostat walls facing the gap. Each intercryostat detector (ICD) consists of 384 scintillator tiles of the same size as the calorimeter cells ($\Delta\eta \times \Delta\phi$=0.1 $\times$ 0.1), which are read out by photomultiplier tubes. Massless gap detectors are made of a sampling LAr layer and are installed in the gap region to make further measurements of shower formation. These detectors compensate for the uninstrumented region, however, they do not have the energy resolution of the CC and EC.

3.6 Muon System

Most of the particles are absorbed in the calorimeter but muons do not interact strongly with the matter and hence escape the calorimeter system with very little energy loss. In order to detect these high energy muons, a muon detector is located outside the calorimeter. The muon detector consists of the central muon system proportional drift tubes (PDTs) and toroidal magnets, central scintillation counters, and a forward muon system. In the muon detector, a tracking system is used to provide position and momentum measurements.

The muon detectors consists of three layers (labeled A, B and C) at increasing distance from the interaction point. These provide position measurements with a combination of drift chambers and scintillating pixels. A toroid magnet between the A and B layers allows a measurement of momentum through the curvature of the muon track.

The muon system has a different geometry than the rest of the DØ detector, with a cuboid rather than cylindrical shape. In the central muon system, covering the range $|\eta| < 1$, detectors are arranged in the planes of x and y. The two forward muon systems consists of detectors in planes of Z, extending the coverage to $|\eta| < 2.2$.

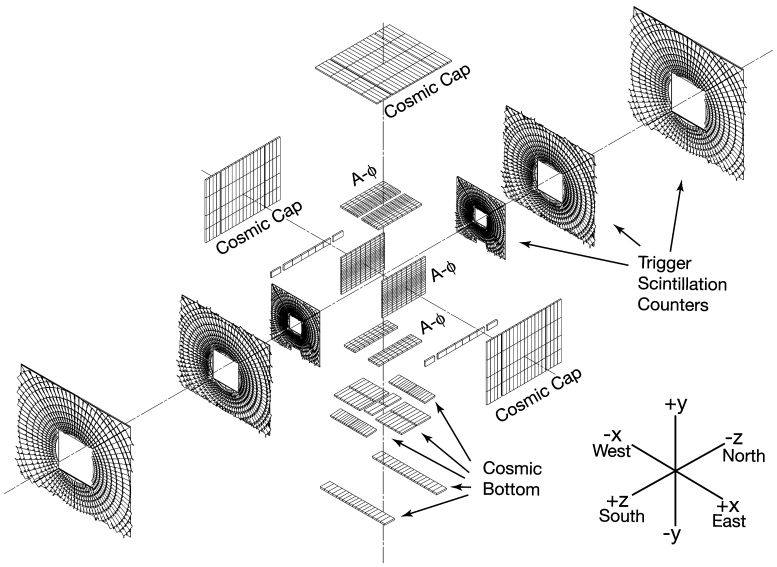

Figure 3.13: Exploded view of the muon wire Chambers.

The central toroid is a square cuboid annulus 109 cm thick whose inner surface is about 318 cm from the tevatron beamline. It covers the region $|\eta| \leq 1$. The magnet is wound using twenty coils of ten turns each. The two end toroids are located at $454 \leq |z| \leq 610\ cm$. The end toroid windings are eight coils of eight turns each. The magnet is being operated at a current of $1500A$ and the fields in the central magnet are approximately 1.8 T and those in the end magnets are approximately 1.9 T.

Three layers of the drift chambers are located inside and outside of the toroidal

magnet. The position of the particles are measured by collecting electrons from gas ionized by the passage of the charge particles. Typically the gas is kept in a sealed volume, with one or more high voltage sense wires used to collect the charge. The arrival time of the signal coupled with the drift velocity of free electrons in the gas, gives a measurement of the radial distance from the wire at which the charge was created. This is called the drift distance.

The PDTs outside of the magnet have three decks of drift cells. The cells are 10.1 cm across; each chamber is 24 cells wide and typically contains 72 or 96 cells and an anode wire at the center of the cell. The wires are grouped together in pairs within a deck and then read out by the electronics located at one end of each chamber. For each PDT hit, the following information is recorded: the electron drift time, the difference ΔT in the arrival time of the hit between a hit cell and the neighbor connected to it, and the charge deposition on the inner and outer vernier pads.

To reduce the number of bunch crossings which occur during one maximum drift time interval, a fast mixture of gas is being used. The mixture is 84% argon, 8% methane and 8% CF_4. The operating high volatge is 2.3 kV for the pads and 4.7 kV for the wires. The drift velocity is approximately 10 $cm/\mu s$, for a maximum drift time of about 500 ns. The forward muon system operates in a significantly higher radiation environment due to scattered proton and antiproton fragments that interact with the end of the calorimeter or due to the beam remnants or halo.

The muon system also contains scintillating pixel detectors. The basic pixel design consists of a slab of scintillator, the surface of which has grooves which holds wavelength shifting readout fibers. A photomultiplier tube is attached to each pixel which collects the light from the readout fibers. Time resolutions of around 2.5 ns are expected depending in the pixel size. The pixels also provide the position measurement along the sense wires of the drift chambers.

3.7 Trigger

There are about $1.7M$ collisions taking place at the DØ interaction point every second. Due to limited infrastructure and electronics speed, its almost impossible to write all the events to the tape for the offline analysis. Fortunately, not all the events are of physics interest and hence does not be written to tape. Out of $1.7M$ collisions, most of them are inelastic $p\overline{p}$ scattering and the interesting elastic events occur at much lower rate. These interesting events are selected using a technique known as "triggering", which proceeds by matching event properties to a predefined set of patterns which are characteristics of the physics process of interest.

DØ has three level trigger system. Level-1 is the hardware-based trigger system which uses Field Programmable Gate Arrays (FPGAs) microchips, Level-2 uses FPGAs and microprocessors, and Level-3 is a completely software based system. For a trigger to fire, trigger conditions for all the levels must be satisfied.

Many different triggers are defined for use in data taking with each one designed to fire on a specific type of event. All triggers used in data taking period are grouped together into a "trigger list". The L1 trigger provides the largest reduction in rate as it has to make decisions on every beam crossing to determine whether the event should proceed in the trigger chain. The L1 system can support a total of 128 separate L1 triggers or trigger bits. Each bit is programmed to require a specific combination of trigger terms (or trigger decisions) and the logic is determined by custom hardware and firmware. Each of the L1 trigger elements report their findings to the Trigger Framework (TFW) upon each bunch crossing. The TFW then issues either an L1 "Accept" or "Reject" to process the event further or reject it. If an L1 accept is issued by the TFW then the event data is digitized and moved into a series of 16 event buffers for analysis at Level 2.

The L2 trigger uses both FPGAs and microprocessor chips. L2 reduces the trigger rate by a factor of about two and has an accept rate of about 1.5 kHz. It has 100

μs to either accept or reject the event. On a L2 Accept events are moved into a set of L2 buffers where they await transfer to Level 3. L3 is a fully software based programmable trigger. Standard PCs running the Linux operating system refine the physics objects created by the L2 trigger and do a simple reconstruction of the whole event. The trigger has up to 100 ms to make the decision and the rate is reduced to about 100 Hz.

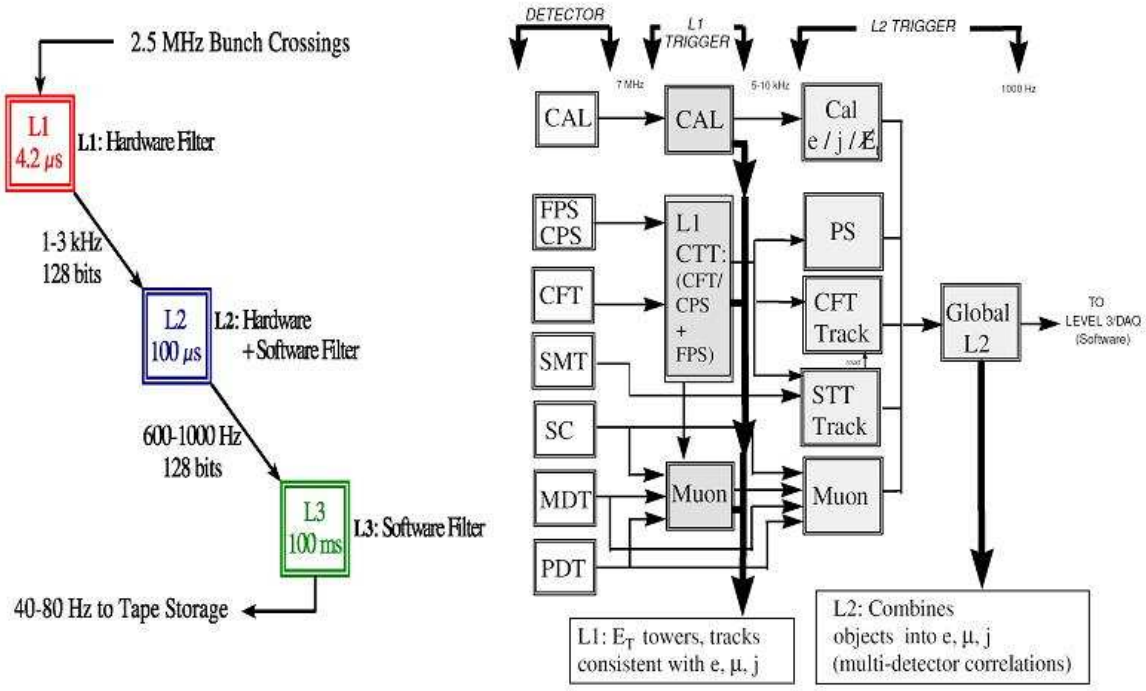

Figure 3.14: Schematic of the DØtrigger system

.

3.8 Level 1 Trigger Elements

3.8.1 Track Triggers

The L1 central track trigger (CTT) is based on the reconstruction of the trajectories of charged particles using fast discriminator data provided by the three scintillator-based detectors: the central fiber tracker and the central and forward preshower

detectors. The CTT trigger is based upon $r-\phi$ hit patterns in 4.5^0 sectors of the CFT. A decision is based on the hit pattern being consistent with a track of one of four software programmable p_T thresholds. There may also be energy deposition in the CPS consistent with the track trigger. The FPS requires a special match between hits in the MIP and shower layers. The digitized signals from all fibers are fed into VME cards with FPGA's that search for tracks via pre-programmed look up tables (LUTs). Each track candidate is identified by its trigger sector, relative ϕ within a trigger sector, momentum, and direction of curvature. While the CTT is optimized for making fast L1 trigger decisions, the electronics also store more-detailed event data for later L2 or L3 readout.

3.8.2 L1 Calorimeter Trigger

The calorimeter tower segmentation in $\eta \times \phi$ is 0.1×0.1, which results in towers whose transverse size is larger than the expected sizes of the EM showers but, considerably smaller than the typical sizes of the jets. For triggering purposes, four adjacent calorimeter towers are added to form a trigger tower (TT) with a segmentation of 0.2×0.2 in $\eta \times \phi$. This yields an array that is 40 in η and 32 in ϕ or a total of 1280 EM and 1280 Hadronic tower energies as inputs to the L1 calorimeter trigger. Since the L1 calorimeter trigger system has been upgraded and completely replaced for the Run IIb of the Tevatron so it is being discussed here in somewhat more detail. Fig. 3.15 shows the block diagram of the L1 calorimeter trigger.

- **Run IIa Calorimeter electronics**:

  The charge from the calorimeter is integrated in the charge sensitive preamplifiers located on the calorimeter. The signals are then transmitted (single ended) on terminated twisted-pair cable to the baseline subtractors cards (BLS) that shape the signal to an approximately unipolar pulse. The signal on the trigger path is further differentiated by the trigger pickoff to shorten the pulse width.

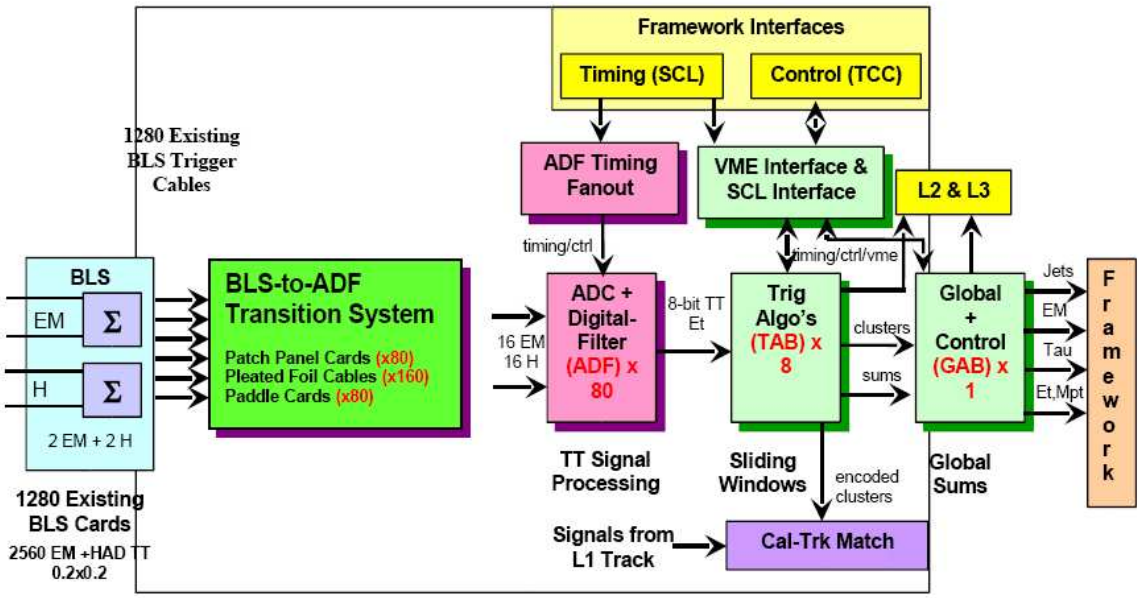

Figure 3.15: Block diagram of L1 calorimeter trigger

.

The signal from the different depths in the electromagnetic and hadronic sections are added with appropriate weights to form the analog trigger tower sums. These analog sums are output to the L1 calorimeter trigger after passing through the trigger sum drivers.

- **Pickoff**:

  The trigger pickoff captures the preamplifier signal before any shaping. The preamplifier signal is differentiated and passed through an emitter follower to attempt to restore the original charge shape (a triangular pulse with a fast rise and a linear fall over 400 ns). This circuitry is located on a small hybrid that plugs into the BLS motherboard. There are 48 such hybrids on a motherboard, and a total of 55,296 for the complete detector.

- **Trigger summers**

  The trigger pickoff signals for the EM and HAD sections in individual towers

are routed in the BLS board to another hybrid plug-in that forms the analog sums with the correct weighting factors for the different radial depth signals that form a single tower. A single 48 channel BLS board has 8 trigger summer hybrid (4 EM and 4 HAD towers). There are a total of 9,216 hybrid trigger summers made up of 75 species.

- **Trigger sum Driver**:

  The outputs of the 4 EM trigger summers and the 4 HAD trigger summers on a single BLS board are summed separately (except at large η) once more by the trigger sum drivers circuit where a final over all gain can be introduced. There are a total of 2,560 such drivers in 8 species.

  Once the analog trigger tower signals from the detector platform reaches the L1 calorimeter trigger located in the first floor moving counting house (MCH1), the first step is to scale these signals to represent the E_T of the energy deposited in each trigger and then digitize these signals at the beam-crossing rate (396 ns) with fast analog to digital converters. The digital output of these 2,560 converters is used by the subsequent trigger logic to form the level 1 calorimeter trigger decision for each beam crossing. The converter outputs are also buffered and made available for the readout to both the level 2 trigger system and the level 3 trigger DAQ system.

  The digital logic used in the L1 cal trigger is arranged in a "pipe-lined" design. Each step in the pipe-line is completed at the beam crossing rate and the length of the pipe-line is less than the maximum DØ level 1 trigger latency for Run IIa which is 3.3 μs. The digital logic is used to calculate a number of quantities that are useful in triggering on specific physics processes. Among these are quantities such as the total transverse energy and the missing transverse energy, which we designate as "global" and information relating to "local" or cluster aspects of the energy deposits in the calorimeter.

- **Global Trigger**

  The interesting global quantities are:

$$(E_T^{EM})_{Total} = \sum_{i=1}^{1280} (E_T^{EM})_i \tag{3.8}$$

$$(E_T^{H})_{Total} = \sum_{i=1}^{1280} (E_T^{H})_i \tag{3.9}$$

  and

$$(E_T)_{Total} = (E_T^{EM})_{Total} + (E_T^{H})_{Total} \tag{3.10}$$

  The missing transverse energy:

$$M_{p_T} = \sqrt{(E_x^2 + E_y^2)} \tag{3.11}$$

  where $E_x = \sum_{i=1}^{1280} \left[(E_T^{EM})_i + (E_T^{H})_i\right] \cos(\phi_i)$ and
  $E_y = \sum_{i=1}^{1280} \left[(E_T^{EM})_i + (E_T^{H})_i\right] \sin(\phi_i)$.

  Any of these global quantities can be used in constructing triggers. Each quantity is compared to a number of thresholds and the result of these comparisons is passed to the trigger framework where upto 128 different Level 1 triggers can be formed.

- **Cluster Trigger**

  In the calorimeter, electrons and photons will manifest themselves as localized EM energy deposits and the quarks and gluons as hadron-like clusters. Energy deposited in a trigger tower is called EM-like if it exceeds one of the EM E_T thresholds and if it is not vetoed by the Hadronic energy behind it. Up to four EM E_T thresholds and their associated H veto thresholds may be programmed for each of the 1280 trigger towers. Hadronic energy deposits are detected by calculating the EM E_T + H E_T of each trigger tower and comparing each of

these 1280 sums to four programmable thresholds.

3.8.3 Motivations for Upgradation

Due to an increase in the luminosity and the decrease in bunch spacing (132 ns) for Run IIb, there is a heavy load on the L1 Calorimeter trigger. Also, the Run IIb L1 Cal trigger performance improvements allow increased rejection of backgrounds from QCD jet production and new tools for recognition of interesting signatures. In order to achieve these things, we need

1. An improved capability to correctly assign the calorimeter energy deposits to the correct bunch crossing via digital filtering.

2. A significantly sharper turn-on for jet triggers, thus reducing the trigger rates.

3. Improved trigger turn-on for electromagnetic objects.

4. The ability to match tracks to energy deposition in calorimeter trigger towers, leading to reduced trigger rates.

3.8.4 New L1 Cal Trigger System

Architectural overview of the new system:

The main elements of the new system are:

1. ADC-Digital-Filter Boards (ADF) that receive analog TT signals, from the BLS cards, digitize them, convert from energy to transverse energy and perform the digital filtering to associate energy with correct bunch crossing. There are a total of 80 such boards and each of these deals with signals from 16 EM TTs and 16 HAD TTs.

2. ADF Timing Fanout Boards (ATF) that send timing signals coming from the trigger framework to the ADF cards.

3. Trigger Algorithm Boards (TAB) that receive TT transverse energies from the ADF boards. Each of the 80 ADF cards will send three copies of data from 16 EM TTs and 16 HAD TTs to the TAB bit-serially in 8-bit words. Data transmission

between the ADF and TABs are accomplished using LVDS links. The TAB produces EM and jet cluster $E_T s$ using a sliding windows algorithm and begins the global summing process that will yield scalar summed transverse energy (E_T, total) and missing transverse energy ($\not\!\!E_T$). Outputs are also provided at this level for data transmission to L2/L3 and the Cal-track match system. TAB also allows transmission of fake data, by computer, directly after the inputs to test system functionality and debugging purposes. A block diagram of TAB is shown in Fig. 3.16.

4. A Global Algorithm Board (GAB) that receives data from the TABs and produces the final E_T, E_{total} and missing E_T, as well as providing an interface to the DØ trigger framework and a timing fanout. The data consists of trigger terms derived from counts of clusters over threshold and global sums and sends these to the trigger framework. The GAB receives timing and control information from the trigger framework over the Serial Command Link (SCL) via an SCL Receiver Mezzanine card (SCLR) and fans this out to the ADF and TAB as necessary. It sends data to L2 and L3.

3.8.5 ADF to TAB Data Transmission

Each ADF outputs 16 8-bit trigger towers and 4 8-bit control words. The control words are the Bunch Crossings (BC) number, the frame bit signifying the least significant bit (i.e. it is always "1"), the parity, and a spare word. These 20 words are 8-bit serial on the ADF, requiring a 60 MHz clock. These 20 words are sent to LVDS channel link serializers, which multiplex the 20 words using a higher frequency. On the TAB, the channel link receiver steps this data down back to 20 words of 8-bit serial data clocked at 60 MHz.

The data from the ADF is written into a dual port memory using a 60 MHz clock. It is read out by the TAB using a 90 MHz clock, with the additional four bits available due to the higher speed set to zero. These additional bits are not needed for the input data, but are used by the output of the sliding windows algorithm.

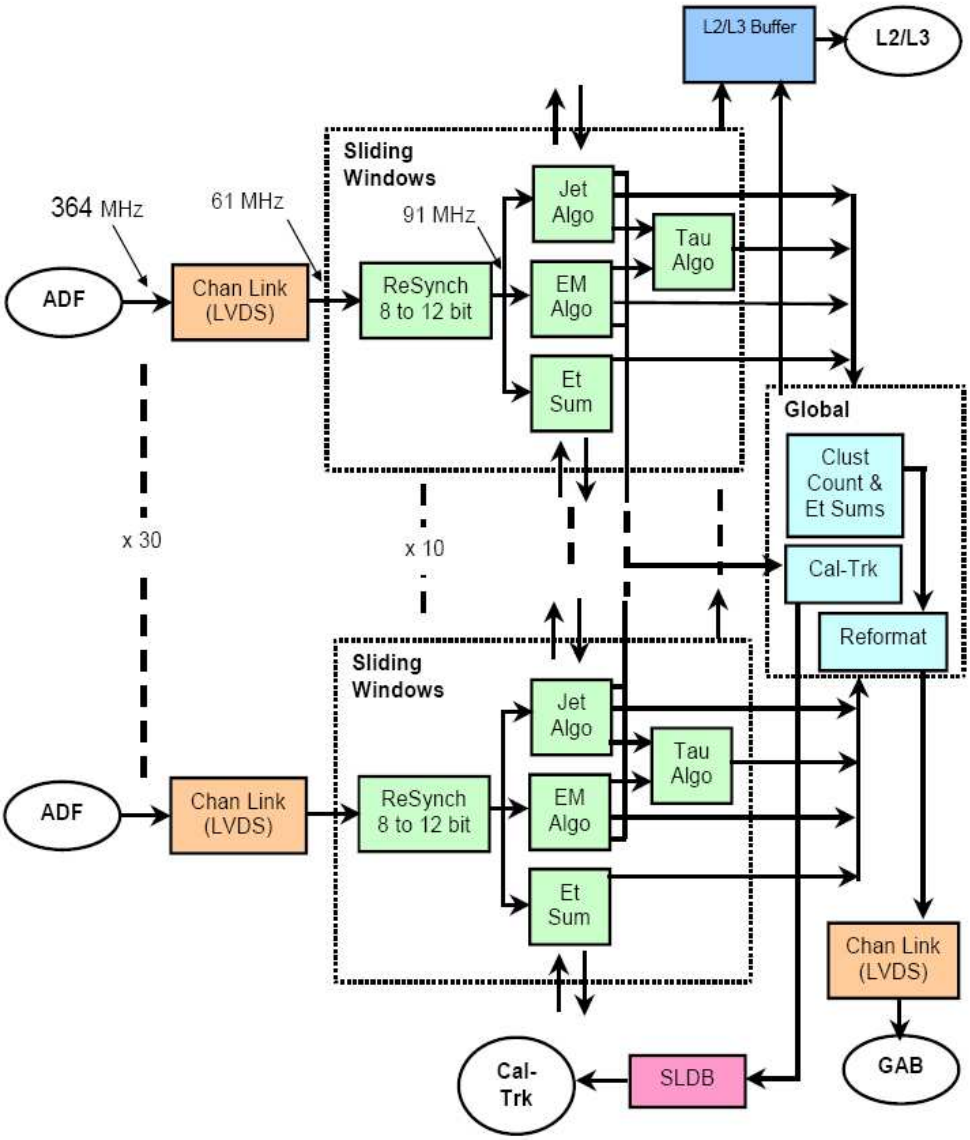

Figure 3.16: Block Diagram of TAB

.

Once taken from the dual port memory, the TAB can be directed to save the data in diagnostic memory for readout over VME. In this way, the data can be checked offline for parity errors. The TAB also calculates the parity on board and latches a parity error if it does not agree with parity reported by the ADF.

The ADF can be directed to send pseudo-random data, that is, data that appears random but can in fact be calculated from a simple algorithm. The TAB is equipped

to check that the pseudo-random data from the ADF is exactly as expected.

3.8.6 TAB to L2/L3 Data Transmission

Upon a L1 accept, the TAB global chip assembles data from all ten sliding windows algorithm chips and sends it to a glink transmitter. It is transmitted through a fiber optic cable and received on a VTM. There, a glink receiver decodes the data and sends it on to a VRB for L3 or a FIC for L2. The glink receiver reports sync lost if the phase locked loop (PLL) on the receiver loses lock with the incoming data. It reports a word error if the reconstructed data is not a valid word according to the glink protocol.

The data is clocked in at 53MHz, which is stepped up by the glink for serial transmission. On the receiving end, the clock is reconstructed by a phase locked loop. Increasing the size of the loop filter capacitor, which makes the receiver more sluggish to respond to jitter in the transmitter clock, has been shown to make the transmission more robust.

Even though the glink protocol allows for separate data words (DAV) and control words (CAV) the VRB/FIC design requires CAV is never sent. Instead, in 20 bit mode, the upper four bits are treated as an in band control word. A value of 1010 signals begin of event while 0101 signals end of event.

3.8.7 Full System Tests

Before installing the full system in MCH1, a part of the system was setup at the side walk test stand. The ADFs cards were connected to the BLS cables coming from MCH1 using the splitters for the four trigger towers. The system was setup so that TAB can send data to L2 and L3 using the fibers and can be operated using the current DØ DAQ system. Once the system was installed at sidewalk, the system was tested with real data coming from the collisions in the Tevatron. To check the

functionality of the system, data was written to tape and was reconstructed using a newly written unpacker for Run IIb. The outcome from the new system was compared to the precision measurement. The comparison plot for four EM and HAD trigger towers can be seen in the fig. 3.17. After the confirmation that the new system was functioning as it was expected to function and after some other latency and bit error tests, the whole system was finally moved to the MCH1 and has been integrated into the DØ trigger and DAQ system.

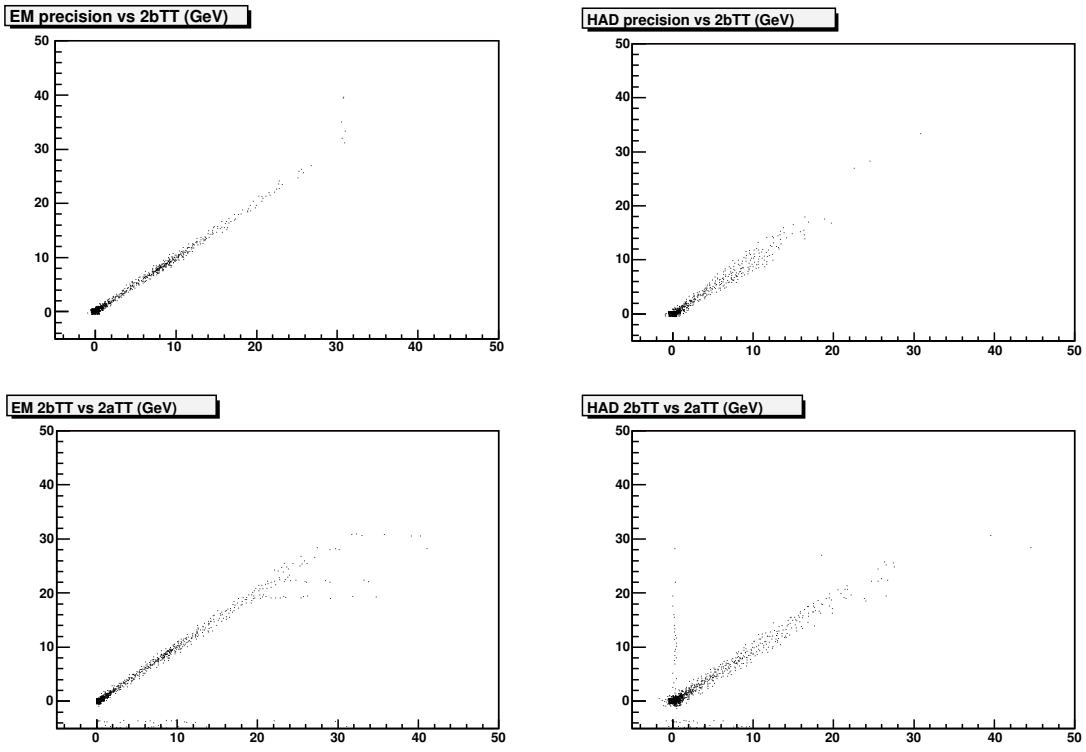

Figure 3.17: Comparison plots for L1Cal2b trigger tower energies with L1Cal2a and precision measurement using the test run data

.

3.8.8 Muon Triggers

L1Muon triggers look for patterns consistent with muons using hits from muon wire chambers, muon scintillation counters, and tracks from the L1CTT. The segmentation

of the muon scintillator was chosen to match that of the trigger sectors of the CFT. FPGAs are used to perform combinatorial logic on roughly 60,000 muon channels and up to 480 tracks from L1CTT for every bunch crossing. Because of the cosmic rays passing the DØ detector, high p_T tracks are also required to pass cosmic ray veto scintillation counters. Cosmic rays are rejected based on their timing information relative to the beam crossing. Since the majority of the cosmic rays pass through the detector at oblique angles they do not pass through the center of the interaction region. When an L1 or L2 Accept is received, the pointer is used to read the data for a particular event.

3.8.9 Level 1 Calorimeter-Track Matching

The L1CalTrack trigger look for matches in the ϕ position of tracks from the L1CTT trigger with that of EM and jet objects from the L1Cal trigger in order to reduce the L1 trigger rates of EM and track triggers. Information from the central preshower and forward preshower detectors is also used. The implementation of the L1CalTrack trigger uses the existing L1Muon architecture (discussed in section 3.8.8) with small modifications.

3.8.10 Trigger Framework

The L1 trigger framework (TFW) gathers digital information from each of the specific L1 trigger devices and chooses whether a particular event is to be kept for further examination. In addition, it coordinates various vetoes that can inhibit triggers, provides the prescaling[4] of triggers too copious to pass on without rate reduction, and correlates the trigger and readout functions. The framework also manages the

[4]Some triggers are designed to fire on more common physics events which occur too often to keep each of them. Prescales are defined to lower the event rate of these triggers. Prescaled triggers are only tested once out of every 'prescale' number of events. For example, if a trigger is prescaled by 10 then only 1 out of 10 events will be considered for triggering purpose. The prescale values are highly dependent on the luminosity and hence changes from run to run.

communication tasks with the front-end electronics and the trigger control computers (TCC) and a large number of scalars that allow accounting of trigger rate deadtimes.

3.9 L2 Trigger

The L2 trigger system can handle input rates of upto 10 KHz with a maximum accept rate of 1 KHz. The L2 trigger provides detector-specific preprocessing engines and a global stage (L2Global) to test for correlations in physics signatures across detector subsystems. L2 preprocessors collect data from the front-ends and L1 trigger processors and analyze these data to form physics objects. For each L1 trigger bit there is a corresponding L2 trigger bit.

The L2 trigger consists of L2CAL, L2CTT, L2STT, L2PS and L2MU preprocessors for the individual subdetector system and a global processor (L2Global) which makes the trigger decisions. The preprocessors handle data specific to the individual subdetectors, and in general, prepare lists of physics objects (such as electrons, muons) to be sent to L2Global. L2Global then makes trigger decisions based on the objects found by the preprocessors. This may involve the correlation of objects in different subdetectors (such as calorimeter and track matching), the calculation of kinematic variables from multiple objects. When L2Global makes a decision, the decision is returned to the TFW which in turns issues a L2 Accept or L2 Reject. Events passing the L2 are tagged for full readout and sent to L3 for further analysis.

3.10 L3 Trigger

The Level-3 trigger is a high level, software based, fully programmable trigger. It refines the physics objects created at Level-2, creates new, more sophisticated objects, finds relations between objects and makes the final decision to keep the event. There is full access to the detector readout and limited reconstruction of each event is

performed. It has approximately 50-100 ms in order to do this. The software runs on a farm of standard PC computers running Linux Operating system. Each individual PC is known as a Level-3 node and runs an independent instance of the Level-3 software. There are about 200 nodes.

The Level-3 nodes run essentially two programs: an event builder and an event filter. The event builder is told by the L3 supervisor from which readout crates to expect data. If the event builder does not get a full event from each crate then the event is rejected. The second program runs the event reconstruction and an event filter. The event filter is a list of filters, each of which place requirements on the event. If the event passes any of the event filters, the event is passed on to the datalogger where it is sent to tape for the offline analysis. The L3 acceptance is about 100 Hz.

Chapter 4

Initial State Tagging

4.1 Introduction

In this chapter we describe a method to identify the initial flavor of a B meson using opposite side flavor tagging technique. First we discuss a method in which we use low energy electrons to tag the initial flavor of B. We describe the selection for $B^{\pm} \rightarrow J/\psi K^{\pm}$ in section 4.3. Then we describe the soft electron selection in section 4.4 and give the results on electron tagging in section 4.5. We then test the electron tagger on the semileptonic sample by measuring the mixing parameter for B_d^0 mixing and the details are given in section 4.8. We also give a brief description of the combined tagging used for the B_s^0 mixing analysis in section 4.13.

4.2 Soft Electron Tagging

Electrons from B decays often have low P_T and the standard clustering with additional isolation requirements is not efficient for selecting these electrons. For this analysis we use track based road electrons to flavor tag a sample of $B^{\pm} \rightarrow J/\psi K^{\pm}$ decays using $\sim 460\ pb^{-1}$ of data collected with the $D\emptyset$ experiment. Determining the B flavor at production is required for B mixing and CP asymmetry measurements. At the

Tevatron, we produce $b\bar{b}$ pairs and so the flavor of one b is strongly correlated to the flavor of the b on the opposite side. One can flavor tag the B, using its semileptonic decay into a lepton $b(\bar{b}) \rightarrow l^-(l^+)\bar{\nu}(\nu)X$ on the opposite side, where 'l' could be an electron or a muon. The details of this technique can be found in [30, 31].

4.3 $B^{\pm} \rightarrow J/\psi K^{\pm}$ decay reconstruction

For this study, we have used the d0root framework to select and vertex tracks. We reconstruct $J/\psi \rightarrow \mu^+\mu^-$ following cuts listed in [32]. We consider all events having at least two well identified muons. Muons are identified by extrapolating tracks and matching them with the muon track segments formed from the hits in the muon system. We applied the following cuts on the two muons in reconstructing J/ψ's:

- Two loose certified muons of opposite charge.
- For muons with $nseg > 0$, $P_T > 1.5\ GeV/c$
- $P_T > 1.0$ for $nseg(\mu) = 0$. Cuts on calorimeter quantities, consistent with a MIP.
  - nmtc() ≥ 0
  - $CalEsig() > 0.015 \cdot CalNLayer()$
  - $P_T > 2.5GeV$ for second muon.
- At least 1 muon with nseg=3.
- number of CFT & SMT hits > 0 for each track.
- $M(\mu^+\mu^-) > 2.5GeV/c^2$.

The two muons are vertexed to form the J/ψ candidate. To reconstruct the decay $B^{\pm} \rightarrow J/\psi K^{\pm}$, only $J/\psi's$ in the mass region 2.8-3.35 GeV are considered. The cuts for the kaon track are summarized below,

- $P_T > 0.5\ GeV$, $P_{tot} > 0.7\ GeV$
- > 1 SMT hits
- If the P_T of the kaon is $< 1.0\ GeV$, it is required to be in the same jet as the J/ψ.
- The 3D impact parameter significance of the kaon, relative to the primary vertex $\frac{dca^2}{\sigma^2_{dca}} + \frac{zdca^2}{\sigma^2_{zdca}} > 3$

The B candidate is required to satisfy additional criteria as follows :

- $P_T(J/\psi) > 5.0\ GeV$.
- At least 2 of the three tracks should have ≥ 2 hits in the SMT.
- The χ^2 of the three track vertex should be < 16 or < 9 (if kaon $P_T < 1.0\ GeV$).
- The decay length significance $\frac{L}{\sigma_L}$ of the B candidate is required to be > 4.5 (is increased to > 5.5, if (P_T(kaon) < 1.0).
- $\cos(\alpha) > 0.9$ where α is the angle between the B candidate and the direction from the primary vertex to the $B^{\pm}$ vertex.

We find a total of 6361 ± 135 signal B candidates shown in Figure 4.1. 5639 ± 119 are signal B candidates where the kaon $P_T > 1\ GeV$ and 722 ± 61 signal candidates where the kaon $P_T < 1\ GeV$. So we find approximately a $\sim 10\%$ increase in statistics by including tracks below 1 GeV, but the S/B is lower. (see Figure 4.2).

4.4 Soft electron selection

The details of the track based EM clusters is described in [40]. In short, the EM cluster is comprised of the η rings and ϕ slices that the track hit and a neighboring ϕ slice is included if it is within a certain dismerge parameter. The dismerge parameter

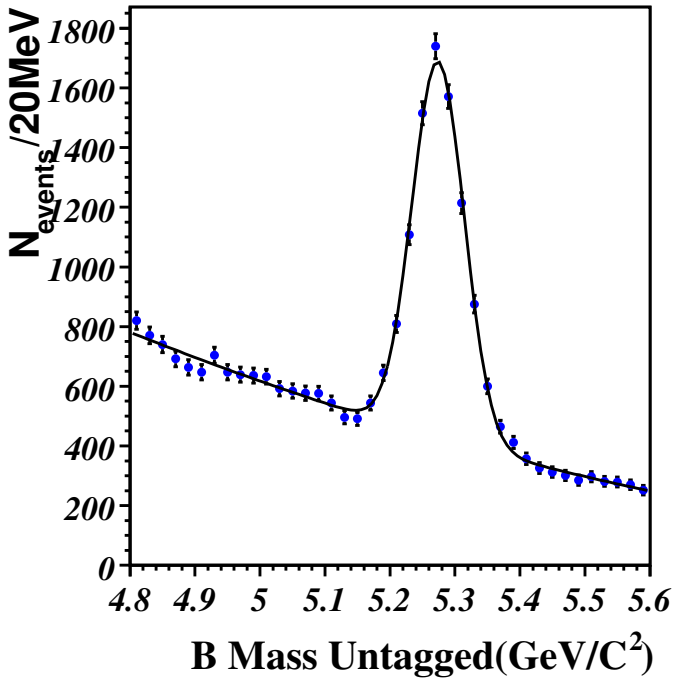

Figure 4.1: Total number of B candidates using $nseg(\mu) \geq 0$

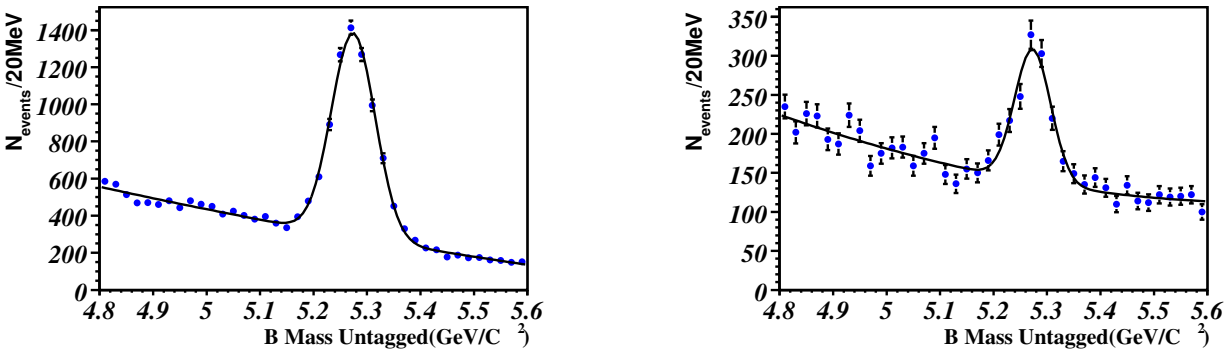

Figure 4.2: B candidates where kaon $P_T > 1.0\ GeV$ (L) and kaon $P_T < 1.0\ GeV$ (R)

is defined as the difference between the hit position and the nearest ϕ slice divided by the slice width. A neighboring η ring is included if both entrance and exit points lie within the dismerge zone of the hit ring. The ratio of energy contained in the road cluster to the total energy deposited in the first three floors is 89% on an average. The energy deposited in the first three floors in the calorimeter is 90% of the total energy deposited by the electron, so we expect $E/P \sim 80\%$ for road electrons. Therefore we do not see a peak at ~ 1.0 for the E/P distribution for road electrons. The definition of E/P and Energy fraction(EMF) in the EM calorimeter is as follows,

$$EMF = \frac{\sum_{floornumberi=1,2,3} E_T(i)}{\sum_{allfloors} E_T(i)}, \tag{4.1}$$

$$E/P = \frac{\sum_{floornumberi=1,2,3} E_T(i)}{P_T(\mathrm{t}rack)}, \tag{4.2}$$

where $E_T(i)$ is the transverse energy within the road in floor i. The above defined EMF does not include the energy in the fourth floor. The road clustering algorithm calculates these variables for three different values of the dismerge parameter for the central region, 0.25, 0.125, 0.0. For this analysis, we chose to use the value 0.25.

4.5 Electron tagging

We have optimized the cuts using simulated $B^+ \rightarrow J/\psi K^+$ events, and studied expectations for efficiency and dilution. We first give numbers obtained from the Monte Carlo simulation in subsection 4.5.1 and then in subsection 4.5.2 we summarize the results obtained from data. We require the tag electron to satisfy the following selection criteria. As stated earlier this is a road electron.

- $P_T > 2.0\ GeV$
- $EMF > 0.7$
- Central region($\mid \eta \mid < 1.1$) : $0.6 < E/P < 1.2$.

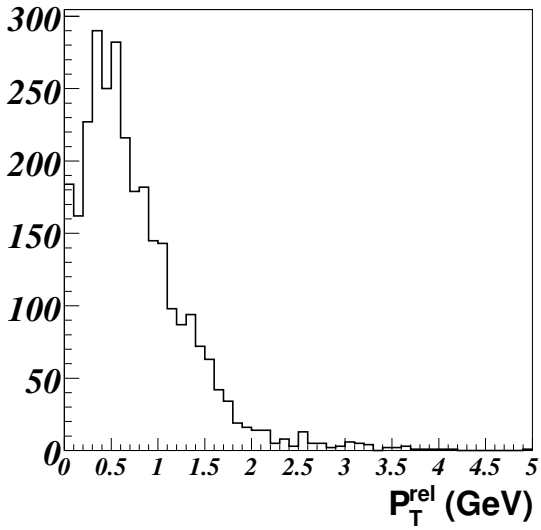

Figure 4.3: P_T^{rel} distribution for the tag electron

- $\mid \Delta\phi \mid$ between electron and the B candidate should be > 2.5 rad(144°).

If we find more than one non isolated EM candidate, we choose the electron with the maximum P_T^{rel}. P_T^{rel} is the relative P_T of the electron with respect to the nearest jet, i.e. closest in $\Delta R = \sqrt{(\Delta\eta^2 + \Delta\phi^2)}$ where $\Delta\eta$ is the difference in pseudorapidity between electron and jet and $\Delta\phi$ is the difference in azimuthal angle between electron and jet. We require $\Delta R_{e-jet} < 0.7$. If no non-isolated electron is found, we take the electron with the maximum P_T. 5.7 % of the events have more than 1 EM candidate. The P_T^{rel} distribution of the tag electron is shown in Figure 4.3.

We fit both the untagged and the tagged B mass distributions to a single Gaussian and a second order polynomial to obtain the number of events in the signal Gaussian. We fix the background shape of the tagged mass plots from the total untagged fit and let the rms float for all the fits. The efficiency (ϵ) and dilution ($\mathcal{D}$) of the tag is defined in equation 3. The tagging power ($\epsilon\mathcal{D}^2$) quantifies the performance of the tag. The higher this value, the better is the tag performance.

$$\epsilon = \frac{R+W}{N} \qquad\qquad \mathcal{D} = \frac{R-W}{R+W} \tag{4.3}$$

The uncertainties on ϵ, $\mathcal{D}$ and $\epsilon\mathcal{D}^2$ are given in equations 4.4 - 4.6.

$$\sigma_\epsilon^2 = \frac{1}{N^2}({\sigma_R}^2 + {\sigma_W}^2), \tag{4.4}$$

$$\sigma_{\mathcal{D}}^2 = \frac{4W^2}{(R+W)^4}{\sigma_R}^2 + \frac{4R^2}{(R+W)^4}{\sigma_W}^2, \tag{4.5}$$

$$\sigma_{\epsilon\mathcal{D}^2}^2 = (\epsilon\mathcal{D}^2)^2(\frac{(R+3W)^2\sigma_R^2 + (W+3R)^2\sigma_W^2}{(R^2-W^2)^2}), \tag{4.6}$$

where R and W are the number of right sign, i.e. the tag electron is oppositely charged to the kaon used in the B^+ reconstruction, and wrong sign, i.e. where the tag electron has the same charge as the opposite kaon, and σ_R and σ_W are their respective errors. N is the total number of reconstructed B candidates.

4.5.1 Electron tagging in Monte Carlo

From the simulation, we study the contribution to the dilution and also the reconstruction efficiency of our electron cuts. Some of the sources which contribute to right and wrong sign electrons are listed in Table 4.1. We obtain a branching fraction of $9.5 \pm 0.2\%$ for direct b to electron decays and we find an acceptance of $4.5 \pm 0.1\%$ in the central ($\eta < 1.1$) region and an acceptance of $3.3 \pm 0.1\%$ in the forward region ($1.4 < \eta < 3.2$).

We evaluate numbers for generator level expectations, assuming we can remove conversions where the second leg P_T goes down to 0.2 GeV. We estimate a maximum expected $\epsilon\mathcal{D}^2 \sim 1.06\%$. Most of the dilution comes from the central region. We get an efficiency of about $4.05 \pm 0.14\%$ in the central region after requiring tag electron $P_T > 1.8\ GeV$ and $\Delta\phi_{eB} > 144^\circ$ at the generator level. We find a tagging power of $0.88 \pm 0.12\%$ in the central and 0.18% in the forward region. This gives us an upper limit on the expected $\epsilon\mathcal{D}^2$ and efficiency in data.

We study the reconstruction efficiency of road electrons by matching generator

Source	Type of Tag	%'age fraction
$b \rightarrow e^-$	R	65.8 %
$b \rightarrow \bar{b} \rightarrow e^+$ (Mixed)	W	8.4 %
$b \rightarrow c \rightarrow e^+$	W	9.3 %
$b \rightarrow c \rightarrow e^-$	R	1.8 %
$b \rightarrow \bar{b} \rightarrow \bar{c} \rightarrow e^+$	W	1.3 %
$b \rightarrow \bar{b} \rightarrow \bar{c} \rightarrow e^-$	R	0.4 %
$J/\psi \rightarrow e^+e^-$	Both	0.9 %
$\tau \rightarrow e$	Both	1.8%
$\pi^0 \rightarrow e^+e^-$	Both	1.4%
$\pi^0 \rightarrow e^+e^-\gamma$(Dalitz)	Both	2.2%
Unseen conversions	Both	4.0%

Table 4.1: Table summarizing contributions to tag electrons

level electrons with the track which seeded the road cluster. For each generator level electron we find the closest road cluster, .i.e. whose track is closest, defined by a minimum in $\chi^2 = (\Delta\eta)^2 + (\Delta\phi)^2$. Requiring $\mid \Delta\phi \mid < 0.02$ rad and $\mid \Delta\eta \mid < 0.02$, we find 588 matched road cluster tracks out of 796 generated electrons, giving a reconstruction efficiency of $73.8 \pm 1.5\%$. The $\Delta\phi$ and $\Delta\eta$ distributions are shown in Fig. 4.4. The E/P and the EMF distribution for these electron matched tracks is shown in Fig. 4.5.

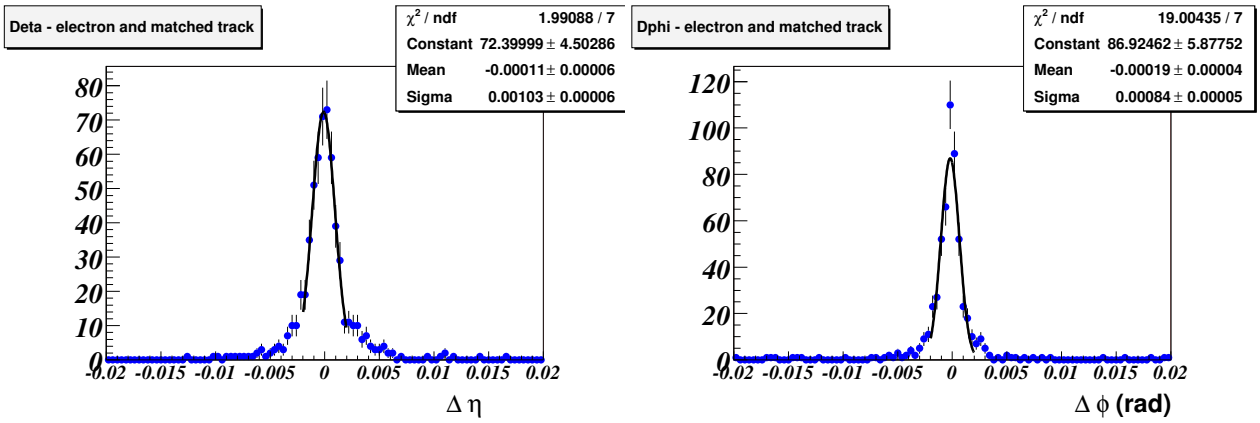

Figure 4.4: $\Delta\eta$ and $\Delta\phi$ between EM object track and the generator level electron ($\mid \eta \mid < 1.1$)

The results of electron tagging in the simulation at the reconstructed level, is summarized in table 4.2. N_{RS} is the number of right sign tags, i.e. the opposite

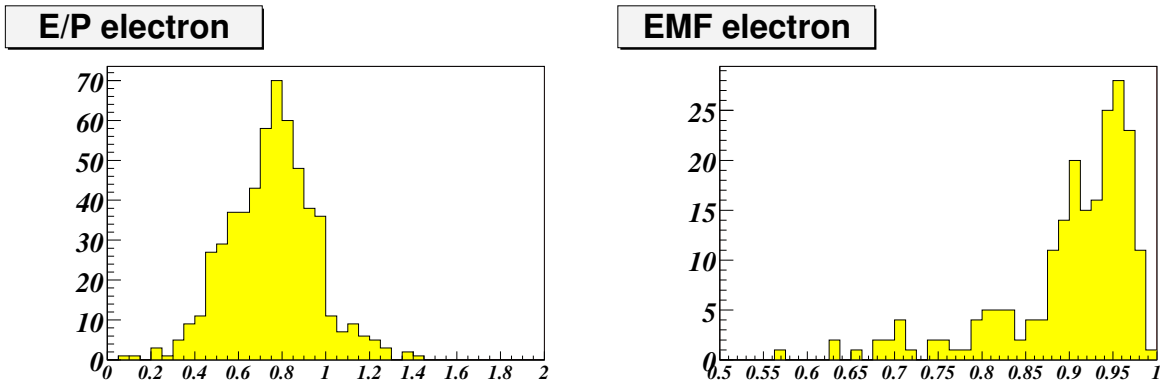

Figure 4.5: $\frac{E}{P}$ and EMF of EM object track matched to generator level electron ($|\eta| < 1.1$)

side electron is oppositely charged to the kaon used for the B candidate and N_{WS} is number of wrong sign tags, i.e where the electron has the same charge as the kaon in the B candidate. We find a low dilution in the forward region and therefore concentrate only in the central region. Out of a total of 5393 ± 74 B candidates, we select 133 tagged events. The number of events is obtained from a fit to the B mass distribution. We used the MC sample number 12603 listed on the B group Monte carlo page [34]. The B mass distribution before and after tagging is shown in Figures 4.6 and 4.7.

N_{RS}	N_{WS}	Efficiency	Dilution	$\epsilon\mathcal{D}^2$ (%)
98	35	$2.5 \pm 0.2\%$	$47.4 \pm 7.7\%$	$0.56 \pm 0.18\%$

Table 4.2: Table summarizing tagging results for simulated events

4.5.2 Electron tagging in data

It was found that the forward region contributes little to the dilution and more studies are needed in the forward region. Due to the poor dilution in the forward region, we use electrons only in the central region ($|\eta| < 1.1$). Out of a total of 6361 ± 135, we find a total of 126 ± 16 tagged events. Table 4.3 summarizes the results for the

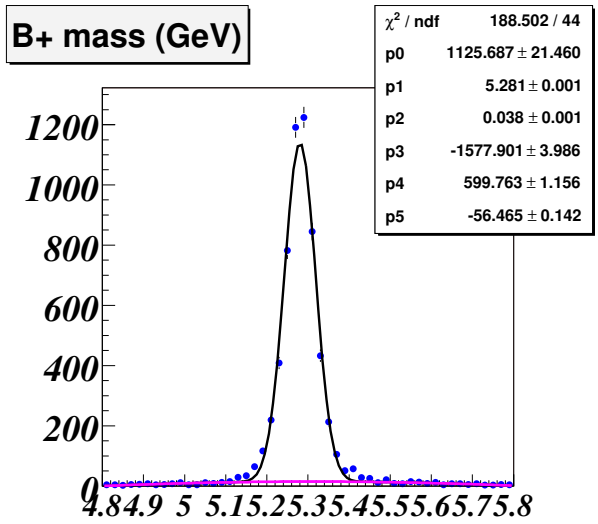

Figure 4.6: B mass distribution in the MC sample

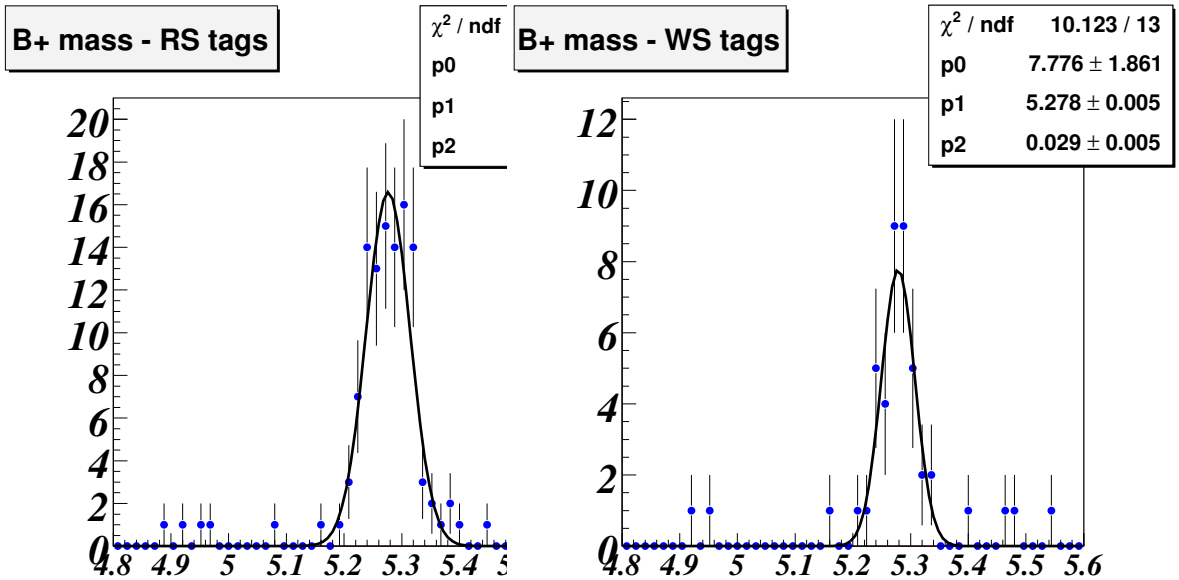

Figure 4.7: Right sign and wrong sign tagged candidates in MC sample using central electrons

tagging and Figure 4.8 shows the B candidates for right sign and wrong sign tags.

N_{RS}	N_{WS}	Efficiency (%)	Dilution (%)	$\epsilon\mathcal{D}^2$(%)
89 ± 12	37 ± 10	2.0 ± 0.2	41.2 ± 12	0.34 ± 0.19

Table 4.3: Summary of electron tagging results in the data.

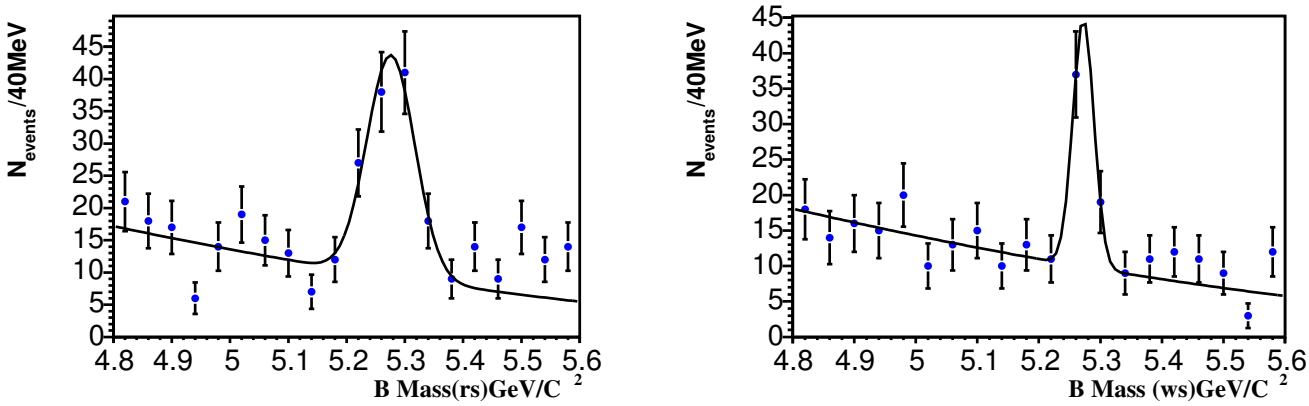

Figure 4.8: Right sign and wrong sign tagged events in data using central electrons

4.6 Conclusion

We find a tagging power of $0.34 \pm 0.19\%$ from data and a tagging power of $0.56 \pm 0.18\%$ from simulation for electrons. The efficiency is about 2.5% in the Monte Carlo simulation and $2.0 \pm 0.2\%$ in data.

As noted in section 4.5.1 the tagging efficiency in the central region for generator level electrons is $\sim 4.0\%$. Including the electron reconstruction efficiency of 70% and the 90% efficient cuts on E/P and EMF, we predict an overall tagging efficiency of 2.5% which gives an estimate of the upper limit on efficiency we can achieve.

4.7 Fit Cross checks

In order to test the stability of our mass fitting procedure, we performed various fits with different options. When both the background and width is fixed from the fit to the total untagged sample, we obtain an efficiency of $1.94 \pm 0.22\%$ and dilution of $41.9 \pm 11.5\%$, giving a tagging power of $0.34 \pm 0.18\%$. When the background is fixed from fit to the total tagged sample and width is fixed from fit to total untagged sample then we get an efficiency of $1.77 \pm 0.22\%$, dilution of $43.3 \pm 12.6\%$ and tagging power of $0.33 \pm 0.18\%$. Hence, we confirm the robustness of our default fit.

4.8 B_d^0 mixing with electron tagging

Now that we have demonstrated the feasibility of using an initial state electron tagger, we now turn to the measurement of Δm_d using $B_d^0 \to \mu^+ \nu \mathrm{D}^{*-} X$ events.

4.8.1 Untagged sample Reconstruction

For this analysis, muons were required to have transverse momentum $P_T^\mu > 2$ GeV/c as measured in the central tracker, pseudo-rapidity $|\eta^\mu| < 2$ and total momentum $p^\mu > 3$ GeV/c. All charged particles in a given event were clustered into jets using the DURHAM clustering algorithm [39]. Events with more than one identified muon in the same jet were rejected, as well as events with identified $J/\psi \to \mu^+\mu^-$ decays.

The $\bar{\mathrm{D}}^0$ candidate was constructed from two particles of the opposite charge belonging to the same jet as the reconstructed muon. Both particles are required to have transverse momentum $P_T > 0.7$ GeV/c, and pseudo-rapidity $|\eta| < 2$. They were required to form a common D-vertex with good fit χ^2. For each particle, the axial (plane perpendicular to the beam direction) ϵ_T and stereo (plane parallel to the beam direction) ϵ_L projections of the track impact parameter with respect to the primary vertex together with the corresponding errors ($\sigma(\epsilon_T)$, $\sigma(\epsilon_L)$) were computed. The combined significance $\sqrt{(\epsilon_T/\sigma(\epsilon_T))^2 + (\epsilon_L/\sigma(\epsilon_L))^2}$ was required to be greater than 2. The distance d_T^D between the primary and D vertices in the axial plane was required to exceed 4 standard deviations: $d_T^D/\sigma(d_T^D) > 4$. The accuracy of the distance d_T^D determination was required to be better than 500 μm. The angle α_T^D between the $\bar{\mathrm{D}}^0$ momentum and the direction from the primary to the $\bar{\mathrm{D}}^0$ vertex in the axial plane was required to satisfy the condition: $\cos(\alpha_T^D) > 0.9$.

The tracks of muon and $\bar{\mathrm{D}}^0$ candidate were required to form a common B-vertex with good fit χ^2. The momentum of the B-candidate was computed as the sum of the momenta of the μ and $\bar{\mathrm{D}}^0$. The mass of the $(\mu^+\bar{\mathrm{D}}^0)$ system was required to fall

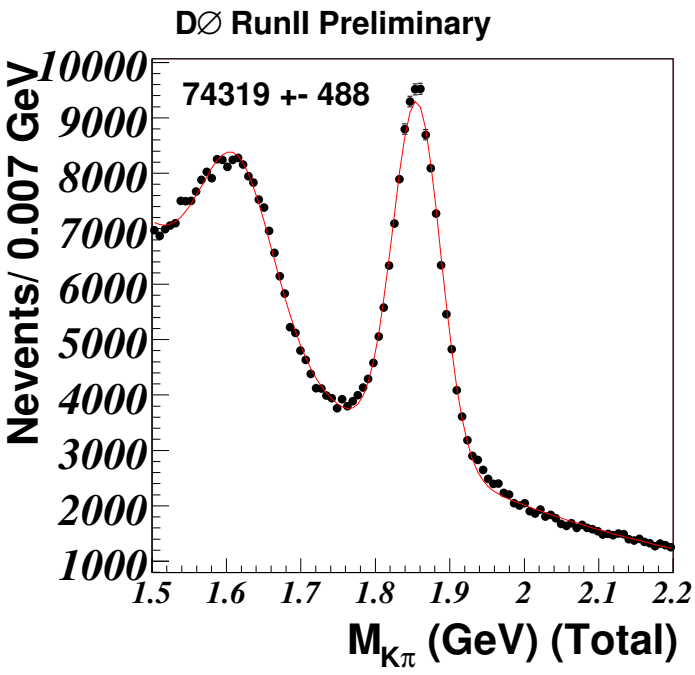

Figure 4.9: The invariant mass of the $K\pi$ system for $\mu^+K^+\pi^-$ candidates before electron tagging.

within $2.3 < M(\mu^+\bar{\mathrm{D}}^0) < 5.2$ GeV/c^2. If the distance d_T^B between the primary and B vertices in the axial plane exceeded $4\sigma(d_T^B)$, the angle α_T^B between the B momentum and the direction from the primary to the B-vertex in the axial plane was demanded to satisfy the condition $\cos(\alpha_T^B) > 0.95$. The distance d_T^B was allowed to be greater than d_T^D, provided that the distance between the B and D vertices d_T^{BD} was less than $3\sigma(d_T^{BD})$. The error $\sigma(d_T^B)$ was required to be less than 500 μm.

The masses of kaon and pion were assigned to the particles according to the charge of the muon, requiring the $\mu^+K^+\pi^-$ final system or its charge conjugate. The mass spectrum of the $(K\pi)$ system after all these selections is shown in Fig. 4.9. The masses of kaon and pion were assigned to particles according to the charge of the muon, requiring a $\mu^+K^+\pi^-$final system. In the following the events falling into the $K\pi$ invariant mass window between 1.4 and 2.2 GeV/c^2 will be referred to as $\mu^+\bar{\mathrm{D}}^0$ candidates.

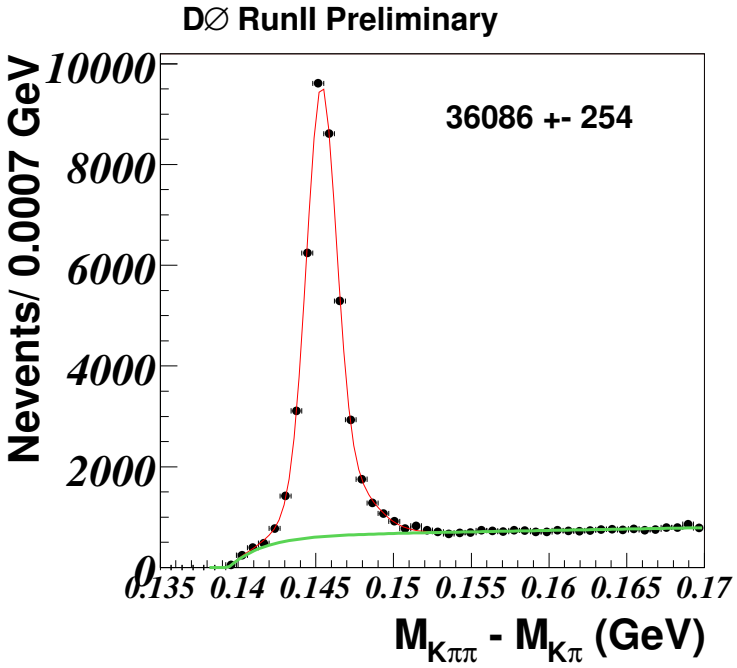

Figure 4.10: The mass difference $M(D^0\pi) - M(D^0)$ for events with $1.75 < M(D^0) < 1.95$ GeV/c^2.

The curve in Fig.4.9 shows the result of the fit of the $K^+\pi^-$ mass distribution with a Gaussian signal peak and polynomial background. The total number of D^0 candidates in the peak is 74319 $\pm$ 488. The peak at lower masses corresponds to the partially reconstructed decay $\bar{D} \to K^+\pi^- X$ where typically a π^0 is not detected. With the tagging criteria described in the next section, the total number of electron tagged events is 1790 ± 96 which gives a tag rate of $(2.4 \pm 0.1\%)$.

For $\mu^+\bar{\mathrm{D}}^0$ candidates, we search for an additional pion with charge opposite to the charge of muon and with $P_T > 0.18$ GeV/c. The mass difference $\Delta M = M(\bar{\mathrm{D}}^0\pi) - M(\bar{\mathrm{D}}^0)$ for all such pions when $1.75 < M(\bar{\mathrm{D}}^0) < 1.95$ GeV/c^2 is shown in Fig.4.10. The peak, corresponding to the production of $\mu^+\mathrm{D}^{*-}$ is clearly seen. The total number of D^* candidates in the peak is equal to 36086 $\pm$ 254. The signal and the background have been modelled by a sum of two Gaussian functions and by the sum of exponential and first-order polynomial functions, respectively.

4.8.2 Tagged Sample

We now apply the electron tagging algorithm described in Section 4.5 to the semi-leptonic final state. Since the semi-leptonic final state are primarily found in events collected with the inclusive single muon triggers, the event environment is likely to be different than in events with the J/ψ final state, which are collected with the dimuon trigger, we re-visit the electron selection criteria. The J/ψ events are less affected by noise, background *etc.* and tend to be "cleaner".

The requirements for the electron tag are summarized below:

- Electron $|\eta| < 1.1$ and $P_T > 2.0$ GeV/c.
- The track associated with the electron has to have at least one hit in the Silicon detector.
- To separate the tag electron from the decaying B candidate, we require (a) the electron is not from the same jet as the B candidate, and (b) cos(ϕ angle between B and tag electron) < 0.5.
- Electron does not come from a photon conversion or from a mis-identified pion (where the latter comes from K_S decay).
- The electron is well reconstructed in the preshower sub-detector. Reconstruction involves combining clusters in each of its three layers to form a 3D cluster. Fig. 4.11 shows the minimum single layer cluster (SLC) energy of a CPS cluster for electrons and pions. We have included a cut on this variable for tagging the semileptonic decays.
- The electron satisfies criteria described in Table 4.4. To improve electron identification, we have divided up the sample in 2 P_T bins and cuts are chosen to keep the pion rejection at the same level. This was studied using a sample of pions from K_S decays and conversions to e^+e^-.

Variable	$P_T^e < 3.5$ GeV/c	$P_T^e > 3.5$ GeV/c
E/P	> 0.55 & < 1.0	> 0.5 & < 1.1
EMF	> 0.8	> 0.7
Min CPS SLC_E (MeV)	> 4.0	> 2.0

Table 4.4: Table summarizing the soft electron cuts.

As described in Section 4.4, if more than one non-isolated electron candidate per event is found the candidate with the maximum P_T^{rel} is selected. If no non-isolated electron is found, then the maximum P_T isolated electron is chosen.

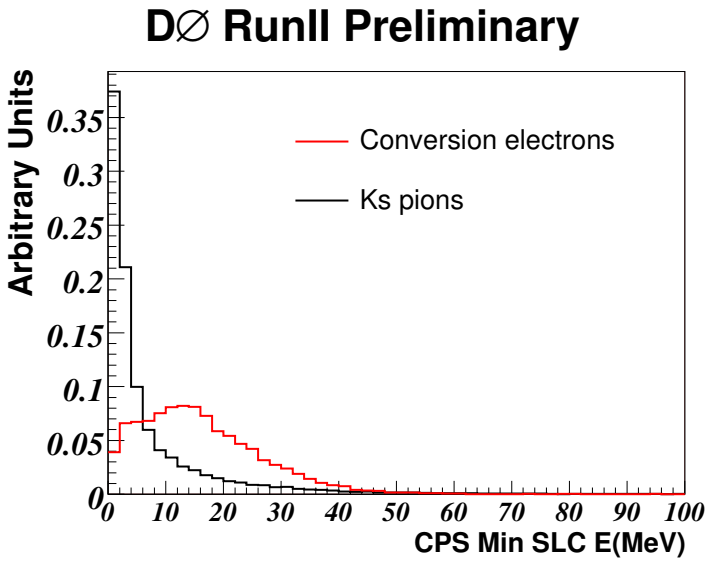

Figure 4.11: Minimum CPS Single Layer Cluster energy of electrons (from photon conversions) and pions (from K_S^0 decays)

Fig. 4.12 shows the mass difference $M(D^0\pi) - M(D^0)$ after tagging. It is found to be equal to 904 ± 36 and thus the tagging rate is determined to be $(2.5 \pm 0.1\%)$.

As will be described in Sec.4.9 the measurement of the B_d oscillations is performed using the ratio of D^* events with right and wrong tags. We also use the fits to the D^0 sample and do a simultaneous fit to obtain the mixing parameter. We use the same algorithm as the one used in the analysis with muons as the inital state flavor tag [37].

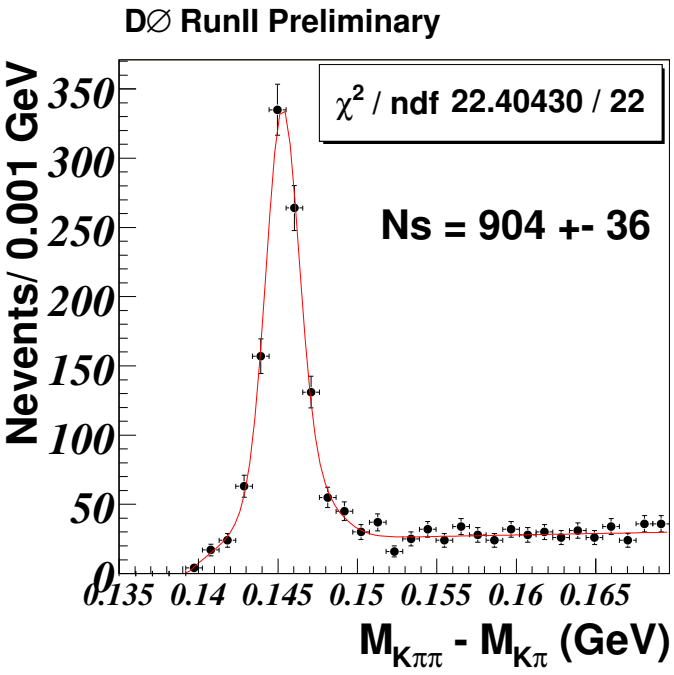

Figure 4.12: The mass difference $M(D^0\pi) - M(D^0)$ for tagged events with $1.75 < M(D^0) < 1.95$ GeV/c^2.

4.9 Experimental Observables

For a mixing analysis, we need to know the production and decay points of the B hadron, so that we can measure its decay length. The transverse decay length of a B-hadron L_{xy} was defined as the distance in the axial plane between the primary vertex and vertex produced by the muon and $\bar{\mathrm{D}}^0$. The vertexing algorithm is described in detail in [42].

The transverse momentum of a B-hadron $P_T^{\mu D^0}$ was defined as the vector sum of transverse momenta of muon and $\bar{\mathrm{D}}^0$. The sign of the decay length was set positive, if the angle α_T^B was less than $\pi/2$, otherwise it was set negative. The measured *visible proper decay length* (VPDL) was defined as

$$x^M = L_{xy} \cdot M_B \cdot c / P_T^{\mu D^0} \tag{4.7}$$

Events were divided into 7 bins according to the measured VPDL. The number of $\mu^+ D^*$ events with same-sign ("oscillated") and opposite-sign ("non-oscillated") tags, N_i^{osc} and $N_i^{non-osc}$, in each bin i of VPDL were determined from a fit of the D^* peak in the mass difference $M(D^0\pi) - M(D^0)$ distribution.

Bin	VPDL (cm)	N_{tot}	$N_i^{non-osc}$	N_i^{osc}	ϵ_i	A_i	A_i^e
1	−0.025-0.000	2154 ±61	29±6	14±5	2.00± 0.30	0.359 ± 0.170	0.340
2	0.000-0.025	9974 ±212	159±14	88±10	2.48±0.16	0.286 ± 0.067	0.331
3	0.025-0.050	8832 ±137	125±12	59±9	2.09± 0.15	0.355 ± 0.078	0.287
4	0.050-0.075	6156 ±121	76±9	46±8	1.98± 0.18	0.245 ± 0.096	0.207
5	0.075-0.100	4163 ±88	51±8	49±7	2.39± 0.24	0.025 ± 0.109	0.104
6	0.100-0.125	2930 ±140	27±6	25±6	1.77± 0.24	0.034 ± 0.157	−0.003
7	0.125-0.250	4735 ±111	49±8	67±9	2.45± 0.23	−0.163 ± 0.104	−0.151

Table 4.5: Definition of the seven bins in VPDL. For each bin the measured number of D^* for the opposite sign and same sign of muon tag $N_i^{non-osc}, N_i^{osc}$, its statistical error $\sigma(N_i^{non-osc}); \sigma(N_i^{osc})$, all determined from the fits of corresponding mass difference $M(D^0\pi) - M(D^0)$ distributions, measured asymmetry A_i, its error $\sigma(A_i)$ and expected asymmetry A_i^e corresponding to $\Delta m_d = 0.545\ ps^{-1}$ (the fit result) are given.

The experimental observables, asymmetry A_i in each VPDL bin, for this measurement were defined as:

$$A_i = \frac{N_i^{non-osc} - N_i^{osc}}{N_i^{non-osc} + N_i^{osc}} \tag{4.8}$$

The number of "non-oscillated" and "oscillated" events, the asymmetries and the corresponding errors derived from the fit in each VPDL bin are given in Table 4.5. For comparison, we show the expected asymmetry obtained from the best fit to the data (described in Section 4.10). Fig. 4.13 shows the asymmetry as a function of the visible proper decay length.

4.10 Fitting procedure and results

The D^* sample is composed mostly of B_d^0 mesons with some contributions from B_u and B_s mesons. Different species of B mesons behave differently with respect to oscillations. Neutral B_d^0 and B_s mesons do oscillate while charged B_u mesons do not oscillate. In the following it was assumed that the oscillations of B_s mesons have infinite frequency. Possible contributions from b-baryons to the sample were also neglected.

The purity of the tagging method was defined as
$\eta_s = N_{correctly\ tagged\ events}/N_{total\ tagged\ events}$. It was assumed that the tagging purity is the same for all reconstructed B mesons because the opposite-side tagging information has little correlation with the reconstructed B meson candidate.

For a given type of reconstructed B-hadron (i.e. $d,\ u,\ s$), the distribution of the visible proper decay length x is given by:

$$n_d^{non-osc}(x,K) = \frac{K}{c\tau_{B_d}} \exp(-\frac{Kx}{c\tau_{B_d}}) \cdot 0.5 \cdot (1 + (2\eta_s - 1)\cos(\Delta m \cdot Kx/c)); \quad (4.9)$$

$$n_d^{osc}(x,K) = \frac{K}{c\tau_{B_d}} \exp(-\frac{Kx}{c\tau_{B_d}}) \cdot 0.5 \cdot (1 - (2\eta_s - 1)\cos(\Delta m \cdot Kx/c)); \quad (4.10)$$

$$n_u^{non-osc}(x,K) = \frac{K}{c\tau_{B_u}} \exp(-\frac{Kx}{c\tau_{B_u}}) \cdot \eta_s, \quad (4.11)$$

$$n_u^{osc}(x,K) = \frac{K}{c\tau_{B_u}} \exp(-\frac{Kx}{c\tau_{B_u}}) \cdot (1 - \eta_s), \quad (4.12)$$

$$n_s^{non-osc}(x,K) = n_s^{osc}(x,K) = \frac{K}{c\tau_{B_s}} \exp(-\frac{Kx}{c\tau_{B_s}}) \cdot 0.5. \quad (4.13)$$

where $K = P_T^{\mu D^0}/P_T^B$ is a K-factor reflecting the difference between the observable and true momentum of the B-hadron and τ is the lifetime of B-hadrons taken from [1]. The K-factors were determined from the simulation using generator-

level information for the computation of p_T^B and $P_T^{\mu D^0}$. The following decay channels of B mesons were considered: $B_d^0 \to \mu^+\nu \mathrm{D}^{*-}$, $B_d^0 \to \mu^+\nu \mathrm{D}^{**-} \to \mu^+\nu \mathrm{D}^{*-}X$, $B^+ \to \mu^+\nu \bar{\mathrm{D}}^{**0} \to \mu^+\nu \mathrm{D}^{*-}X$ and $B_s^0 \to \mu^+\nu \mathrm{D}^{*-}X$. Here and in the following the symbol "D**" denotes both narrow and wide D** resonances, together with non-resonant Dπ and D$^*\pi$ production. The slow pion from D^{*-}decay was not included in the $P_T(\mu D^0)$ computation for the K-factors. The K-factors for all considered decays were combined into 3 groups: $B \to \mu^+\nu \bar{\mathrm{D}}^* X$, $B \to \mu^+\nu \bar{\mathrm{D}}^{**} X \to \mu^+\nu \bar{\mathrm{D}}^* X$ and $B_s \to \mu^+\nu \bar{\mathrm{D}}^* X$.

Translation to the measured VPDL, x^M is achieved by integration over K-factors and resolution functions:

$$N^{osc,\ non-osc}_{(d,u,s),\ j}(x^M) = \int dx\ Res_j(x - x^M) \cdot Eff_j(x) \int dK\ D_j(K) \cdot \theta(x) \cdot n^{osc,\ non-osc}_{(d,u,s),\ j}(x, K). \tag{4.14}$$

Here $Res_j(x - x^M)$ is the detector resolution of the VPDL and $Eff_j(x)$ is the reconstruction efficiency for a given decay channel j of this type of B meson. Both are determined from the simulation. The decay length resolution was parameterised by the sum of 3 Gaussians with the following parameters: widths 26, 56 and 141 microns; relative normalizations 0.423, 0.505 and 0.072 respectively. The step function $\theta(x)$ takes into account that only positive values of x are possible (x^M can have negative values due to resolution effects). The function $D_j(K)$ gives the normalized distribution of the K-factor in a given channel j.

The expected number of oscillated/non-oscillated events in the i-th bin of VPDL is equal to

$$N_i^{e,osc/non-osc} = \int_i dx^M \left(\sum_{f=u,d,s} \sum_j (Br_j \cdot N^{osc/non-osc}_{f,\ j}(x^M)) \right) \tag{4.15}$$

Here the integration $\int_i dx^M$ is taken over a given interval i, the sum $\sum_j$ is taken over all decay channels $B \to \mu^+\nu \mathrm{D}^{*-}X$ and Br_j is the branching ratio of a given

channel j.

The latest PDG values [1] were used for the B decay branching fractions. Exploiting the fact that semileptonic B decays are saturated by decays to D, D^* and D^{**} , and isotopical invariance it was determined that the B_d^0 (85%) and B^+ (15%) decays give the main contributions to the sample. The B_s contribution is small but it was taken into account.

Finally, the expected value A_i^e for interval i of the measured VPDL is given by equation (4.8), and substituting $N_i^{non-osc}$ and N_i^{osc} by $N_i^{e,non-osc}$ and $N_i^{e,osc}$.

The fit values of Δm and η_s were determined from the minimization of a $\chi^2(\Delta m,\eta_s)$ defined as:

$$\chi^2(\Delta m, \eta_s) = \sum_i \frac{(A_i - A_i^e(\Delta m, \eta_s))^2}{\sigma^2(A_i)}. \tag{4.16}$$

We perform a simultaneous fit to the B^0 and B^+ samples. The result of the minimization is:

$$\Delta m_d = 0.545 \pm 0.085 \text{ (stat) ps}^{-1} \qquad \eta_s = (66.9 \pm 1.5)\% \tag{4.17}$$

The values of A_i^e obtained in each bin are given in Table 4.5. Fig. 4.13 shows the asymmetry as function of VPDL together with the result of the fit[1].

4.11 A study of systematic uncertainties

We studied various sources of systematic uncertainties and the more important ones are described in this section, and results are summarized in Table 4.6.

The B meson branching rates and lifetimes used in the fit of the asymmetry were taken from [1] and were varied by 1σ. The VPDL resolution, obtained in simulation, was multiplied by a large factor from 0.2 to 2, significantly exceeds the estimated

[1]As a check the fit was performed by allowing different values of purity for the $B^0$and B^+ dominated samples. In this case, we obtain η_s^0 and η_s^+ to be $(67.4 \pm 2.8)\%$ and $(66.8 \pm 2.0)\%$, respectively, which is consistent with the main result in the text

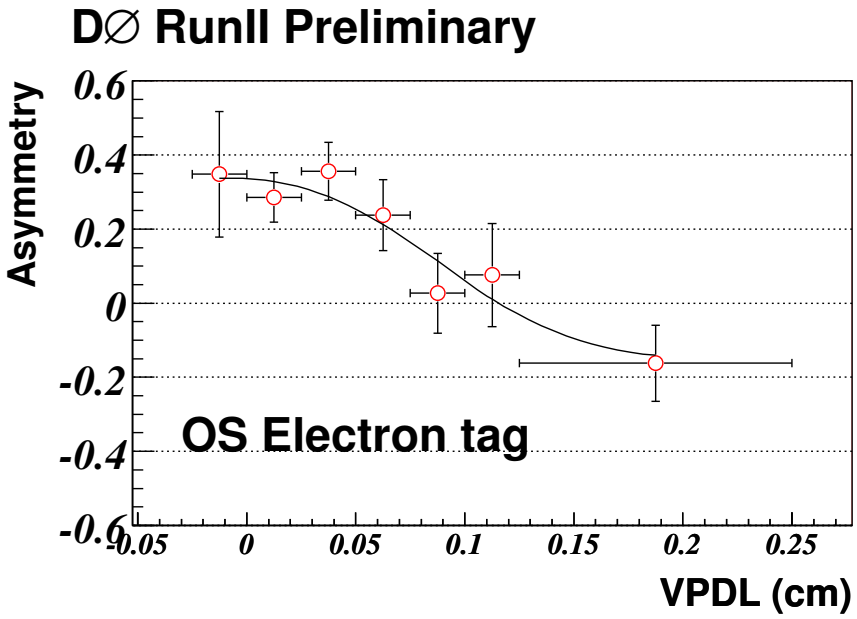

Figure 4.13: The asymmetry in D* sample (dominated by B^0) as a function of the visible proper decay length in cm. The result of the minimization of (4.16) with $\Delta m_d = 0.545$ ps^{-1} is shown as a curve.

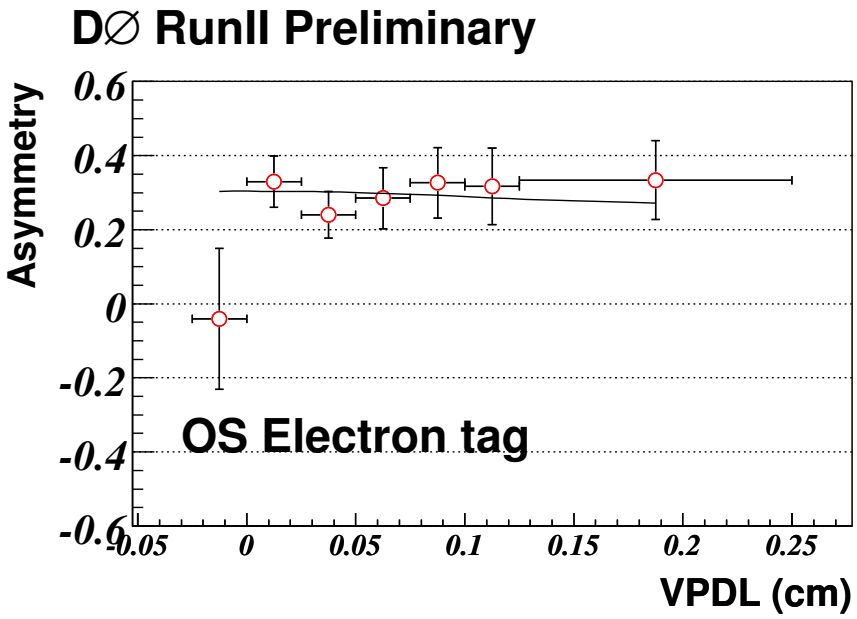

Figure 4.14: The asymmetry in D^0 sample (dominated by B^+) as a function of the visible proper decay length in cm. The result of the minimization of (4.16) with $\Delta m_d = 0.545$ ps^{-1} is shown as a curve.

difference in the resolution between data and simulation.

The variation of K-factors with the change of B momentum was neglected in this analysis. To check the impact of this assumption on the final result, their computation was repeated without the cut on $P_T(D^0)$ or by applying an additional cut on P_T of muon, $P_T > 4$ GeV/c. The change of average value of K-factors did not exceed 2%, which was used as the estimate of the systematic uncertainty in their values. This was propagated into the variation of Δm_d and tagging purity by repeating the fit with the K-factor distributions shifted by 2%.

The reconstruction efficiency in different B-meson decay channels depends only on the kinematic properties of corresponding decays and can therefore be reliably estimated in the simulation. The ISGW2 model [45] was used to describe semileptonic B decays. The uncertainty of the reconstruction efficiency, set at 12%, was estimated by varying kinematic cuts on P_T of the muon and D^0 in a wide range. Changing the model describing semileptonic B decay from ISGW2 to HQET [46] produces a smaller variation. The fit to extract Δm_d was repeated with the efficiencies to reconstruct $B \to \mu^+ \nu \mathrm{D}^{**-}$ and $B \to \mu^+ \nu \bar{\mathrm{D}}^{**0}$ channels modified by 12%, and the difference was taken as the systematic uncertainty from this source.

Possible background contribution into events with small lifetime, e.g. the $c\bar{c}$ contamination of the sample or the misidentification of the muon, can bias the oscillation wave at small values of VPDL. The contribution of this background was varied from 3.5% to 10% and the difference in the result was taken as the systematic uncertainty from this source.

We also investigated the systematic uncertainty of measuring the number of D^* and D^0 candidates in each VPDL bin. This we call systematics due to fit procedure. We changed the background parametrization for the D^0 mass fit from the exponent to a second degree polynomial and varied the background shape by $\pm 1\sigma$.

For the D^* candidates, we performed cross-checks using other functions, but

the chosen background parametrization gives the best description. Since we fix the background shape, we varied the background shape by $\pm 1\sigma$. Also, the default bin width for the fits in individual VPDL bins is 1.40 MeV. We lowered the binwidth to 1.05 MeV, and increased the binwidth 1.75 MeV, and include it in our systematics.

	variation	$\delta(\Delta m_d)$	$\delta(\mathcal{D}(B^0))$	$\delta(\mathcal{D}(B^+))$	$\delta(\mathcal{D})$
$Br(B^0 \to D^{*-}\mu^+\nu)$	$5.53 \pm 0.023\%$	0.002 ps^{-1}	0.001	0.001	0.001
$Br(B \to D^*\pi\mu\nu X)$	$1.07 \pm 0.17\%$	0.008 ps^{-1}	0.002	0.001	0.001
B lifetime	$\pm 1\sigma$	0.001 ps^{-1}	0.000	0.000	0.000
Resolution function	$\times[0.2 \div 2]$	0.006 ps^{-1}	0.002	0.000	0.000
Alignment	$\pm 10\mu$m	0.007 ps^{-1}	0.004	0.000	0.004
K-factor	$\pm$ 2%	0.009 ps^{-1}	0.000	0.000	0.000
$c\bar{c}$ Background	$[0.035 \div 0.1]$	0.002 ps^{-1}	0.002	0.000	0.002
Efficiency	$\pm 12\%$	0.006 ps^{-1}	0.001	0.001	0.001
Fit procedure	Overall	0.010 ps^{-1}	0.006	0.006	0.008
Total		0.019 ps^{-1}	0.008	0.006	0.009

Table 4.6: Systematic uncertainties.

4.12 Conclusions

We use both fully reconstructed $B^{\pm}$ events as well as a large semileptonic sample corresponding to about 36086 ($\mu^+ \mathrm{D}^* X$) candidate events.

Using the latter sample, the B^0 meson oscillation frequency was measured to be consistent with the world average. We also obtained a tag rate, purity and dilution of,

$$\epsilon = (2.5 \pm 0.1)\%, \qquad \eta_s = (66.9 \pm 1.5 \pm 0.5)\%, \qquad \mathcal{D} = (34.0 \pm 3.0 \pm 0.9)\%$$

and tagging power, $\epsilon\mathcal{D}^2 = (0.29 \pm 0.05 \pm 0.03)\%$.

4.13 Combined Tagging

In this section, we discuss how we combined the different tagging algorithms into a single tagging variable to be finally used in our B_s^0 mixing analysis. Many different properties can be used to identify the original flavor – b or $\bar{b}$ – of a heavy quark producing a reconstructed B meson. Some of them perform well by themselves; other properties give a weak separation between flavors. In all cases, their combination into a single tagging variable gives a significantly better result [47, 48] . We obtain such a combination with the likelihood ratio method described below.

It is assumed that a set of discriminating variables $x_1, ...x_n$ can be constructed for a given event. The discriminating variable, by definition, should have a different distribution for b and $\bar{b}$ flavors. For the initial b quark, the probability density function (PDF) for a given variable x_i is denoted as $f_i^b(x_i)$, while for the initial $\bar{b}$ quark it is denoted as $f_i^{\bar{b}}(x_i)$. The combined tagging variable y is defined as:

$$y = \prod_{i=1}^{n} y_i; \quad y_i = \frac{f_i^{\bar{b}}(x_i)}{f_i^b(x_i)} \tag{4.18}$$

Given variable x_i can be undefined for some events. For example, there are events which don't contain an identified muon from the opposite side. In this case, the corresponding variable y_i is set to 1. The initial b flavor is more probable if $y < 1$, and $\bar{b}$ flavor is more probable if $y > 1$. Correspondingly, an event with $y < 1$ is tagged as b quark and the event with $y > 1$ is tagged as $\bar{b}$ quark. For an oscillation analysis, it is more convenient to define the tagging variable as:

$$d = \frac{1 - y}{1 + y}. \tag{4.19}$$

The variable d changes between -1 and 1. An event with $d > 0$ is tagged as b quark and with $d < 0$ as $\bar{b}$ quark. Higher $|d|$ value corresponds to a higher tagging purity.

For uncorrelated variables $x_1, ...x_n$, and perfect modeling in the PDF, d gives the best possible tagging performance and its absolute value gives a dilution of a given event.

Very often analyzed events are divided into samples with significantly different discriminating variables and tagging performance. This division would imply making a separate analysis for each sample and combining results at a later stage. On the contrary, the tagging variable d defined by (4.18-4.19) provides a "calibration" of all events regardless of their intrinsic differences. Since its value is proportional to the dilution of the flavor tagging, events from different categories but with a similar value of d can be treated in the same way. Thus, another important advantage of the proposed method of the flavor tagging is a possibility to build a single variable having the same meaning for all kinds of events. It allows to classify all events according to their tagging performance and use them simultaneously in the analysis.

4.13.1 Discriminating Variables

All our discriminating variables are constructed using properties of the b quark opposite to the reconstructed B meson ("opposite side tagging"). It is assumed that every event with b quark also contains a $\bar{b}$ quark. Therefore, the b flavor at the opposite side determines the b flavor at the reconstruction side. An important property of the opposite side tagging is the independence of its performance on the type of the reconstructed B meson, since the hadronization of two b quark is not correlated in $p\bar{p}$ interactions. Therefore, the flavor tagging algorithm can be calibrated in data by applying it to the events with the B^0 and B^+ decays. The measured performance then can be used to study B_s meson oscillations.

Another set of variables, which exploits properties of hadronization $b \to B$ at the reconstruction side, can also be defined ("same side tagging"). The tagging with these variables depends on the type of B meson. Its performance can only be obtained from the simulation and is therefore model dependent. Currently, it is not used for the B_s

mixing measurement and is not discussed here.

The probability density function for each discriminating variable discussed below was constructed using events from D^0 sample with the visible proper decay length greater than 0 and less than 500 μm. The $B_d^0 \to \mu^+\nu \mathrm{D}^{*+}$ events give 16% contribution and due to the cut on the visible proper decay length contain mainly the non-oscillating B_d^0 decays. Therefore, the initial flavor of a b-quark is determined by the charge of the muon. According to the MC estimates, the purity of such identification of the initial flavor in the selected sample is 0.98 ± 0.01, where the error reflects the uncertainty in branching ratios of B decays.

For each discriminating variable, the signal band containing all events with $1.80 < M(K\pi) < 1.92$, and the background band containing all events with $1.94 < M(K\pi) < 2.2$ were defined. The PDF distribution was constructed as the difference of distribution for the signal band and for the background band multiplied by 0.74. The coefficient 0.74 was chosen so that the number of events in the background band corresponds to the estimated number of background events events in the signal band.

In each analyzed event, an additional muon was searched for. This muon was required to have at least one hit in the muon chambers, and to have $\cos\phi(\mathbf{p}_\mu, \mathbf{p}_B) < 0.8$, where $\mathbf{p}_B$ is a three-momentum of the reconstructed B meson. If more than one muon was found, the muon with the highest number of hits in the muon chambers was used. If more than one muon with the same number of hits in the muon chambers was found, the muon with the highest transverse momentum p_T was used. For this muon, a *muon jet charge* Q_J^μ was constructed as:

$$Q_J^\mu = \frac{\sum_i q^i p_T^i}{\sum_i p_T^i}.$$

The sum was taken over all charged particles, including the muon, satisfying the condition $\Delta R = \sqrt{(\Delta\phi)^2 + (\Delta\eta)^2} < 0.5$. $\Delta\phi$ and $\Delta\eta$ were computed with respect to the muon direction. Daughters of the reconstructed B meson were explicitly excluded

from the sum. In addition, any charged particle with $\cos\phi(\mathbf{p}, \mathbf{p}_B) > 0.8$ was excluded.

An additional identified electron [40] was used for the flavor tagging if $\cos\phi(\mathbf{p}_e, \mathbf{p}_B) < 0.8$. For this electron, an *electron jet charge* Q_J^e was constructed as:

$$Q_J^e = \frac{\sum_i q^i p_T^i}{\sum_i p_T^i}.$$

The sum was taken over all charged particles, including the electron, satisfying the condition $\Delta R = \sqrt{(\Delta\phi)^2 + (\Delta\eta)^2} < 0.5$. $\Delta\phi$ and $\Delta\eta$ were computed with respect to the electron direction. Daughters of the reconstructed B meson were explicitly excluded from the sum. In addition, any charged particle with $\cos\phi(\mathbf{p}, \mathbf{p}_B) > 0.8$ was excluded.

A secondary vertex corresponding to the decay of B mesons was searched for using all charged particles in the event. The secondary vertex should contain at least 2 particles with the axial impact parameter significance greater than 3. The distance l_{xy} from the primary to the secondary vertex should satisfy the condition: $l_{xy} > 4\sigma(l_{xy})$. The details of the secondary vertex search can be found in [42].

The momentum of the secondary vertex $\mathbf{p}_{SV}$ was defined as the sum of all momenta of particles included in the secondary vertex. The secondary vertex with $\cos\phi(\mathbf{p}_{SV}, \mathbf{p}_B) < 0.8$ was used for the flavor tagging. A *secondary vertex charge* Q_{SV} was defined as the third discriminating variable:

$$Q_{SV} = \frac{\sum_i (q^i p_L^i)^k}{\sum_i (p_L^i)^k}.$$

where the sum was taken over all particles included in the secondary vertex. Daughters of the reconstructed B meson were explicitly excluded from the sum. In addition, any charged particle with $\cos\phi(\mathbf{p}, \mathbf{p}_B) > 0.8$ was excluded. The p_L^i is the longitudinal momentum of a given particle with respect to the direction of the secondary vertex momentum. The value of $k = 0.6$ was used. It was taken from the previous studies

at LEP [44]. We found that this value of k results in an optimal performance of the Q_{SV} variable, as can be seen in Fig. 4.15.

Finally, the *event charge* Q_{EV} was constructed as:

$$Q_{EV} = \frac{\sum_i q^i p_T^i}{\sum_i p_T^i}.$$

The sum was taken over all charged particles with $0.5 < p_T < 50$ and having $\cos\phi(\mathbf{p}, \mathbf{p}_B) < 0.8$. Daughters of the reconstructed B meson were explicitly excluded from the sum.

4.13.2 The Combined Tagger

For each event with an identified muon, the muon jet charge Q_J^μ and the secondary vertex charge Q_{SV} were used to construct a *muon tagger*. For each event without a muon but with an identified electron, the electron charge Q_J^e and the secondary vertex charge Q_{SV} were used to construct an *electron tagger*. Finally, for events without a muon or an electron but with reconstructed secondary vertex, the secondary vertex charge Q_{SV} and the event jet charge Q_{EV} were used to construct a secondary vertex tagger. The resulting distribution of the tagging variable d for the combination of all three taggers, called the combined tagger, is shown in Fig. 4.16.

4.14 Results

For any sample of tagged events, the observed and expected asymmetries were determined using the flavor asymmetry given as

$$A = \frac{N^{nos} - N^{osc}}{N^{nos} + N^{osc}}, \tag{4.20}$$

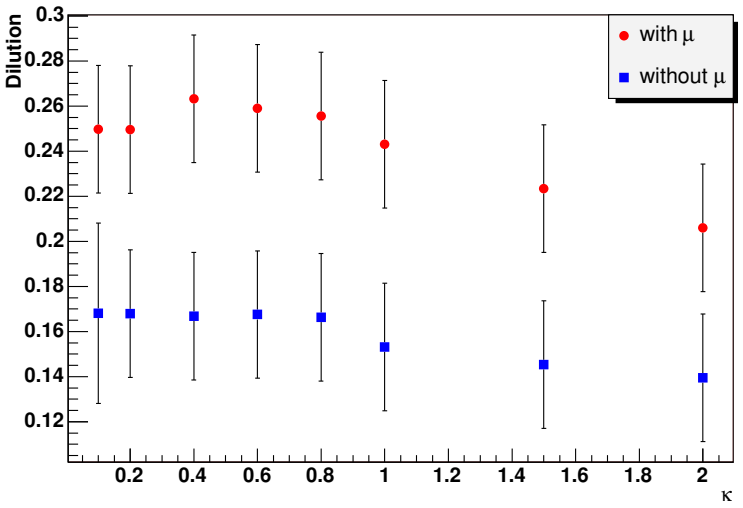

Figure 4.15: Dilution of events tagged by Q_{SV} versus the coefficient k. Statistical errors shown are correlated.

and the expected value A_i^e for interval i of the measured VPDL given as:

$$A_i^e(\Delta m, f_{c\bar{c}}, \mathcal{D}_d, \mathcal{D}_u) = \frac{N_i^{e,nos} - N_i^{e,osc}}{N_i^{e,nos} + N_i^{e,osc}} \tag{4.21}$$

in all VPDL bins. The values of $\Delta \mathrm{m_d}$, $f_{c\bar{c}}$, $\mathcal{D}_u$ and $\mathcal{D}_d$ were obtained from the simultaneous χ^2 fit:

$$\begin{aligned}
\chi^2(\Delta \mathrm{m_d}, f_{c\bar{c}}, \mathcal{D}_d, \mathcal{D}_u) &= \chi^2_{\mathrm{D}^*}(\Delta \mathrm{m_d}, f_{c\bar{c}}, \mathcal{D}_d, \mathcal{D}_u) + \chi^2_{D^0}(\Delta \mathrm{m_d}, f_{c\bar{c}}, \mathcal{D}_d, \mathcal{D}_u) \quad (4.22)\\
\chi^2_{\mathrm{D}^*}(\Delta \mathrm{m_d}, f_{c\bar{c}}, \mathcal{D}_d, \mathcal{D}_u) &= \sum_i \frac{(A_{i,\mathrm{D}^*} - A^e_{i,\mathrm{D}^*}(\Delta \mathrm{m_d}, f_{c\bar{c}}, \mathcal{D}_d, \mathcal{D}_u))^2}{\sigma^2(A_{i,\mathrm{D}^*})}\\
\chi^2_{D^0}(\Delta \mathrm{m_d}, f_{c\bar{c}}, \mathcal{D}_d, \mathcal{D}_u) &= \sum_i \frac{(A_{i,D^0} - A^e_{i,D^0}(\Delta \mathrm{m_d}, f_{c\bar{c}}, \mathcal{D}_d, \mathcal{D}_u))^2}{\sigma^2(A_{i,D^0})}.
\end{aligned}$$

Here $\sum_i$ is the sum over all VPDL bins. Examples of the fit of the flavor asymmetry with (Eq.4.22) is shown in Fig. 4.17-4.18.

The performance of the flavor tagging was studied separately for the muon, electron and secondary vertex taggers using events with $|d| > 0.3$. Results are given in Tables 4.7-4.9. All errors are statistical and do not include systematic uncertainties.

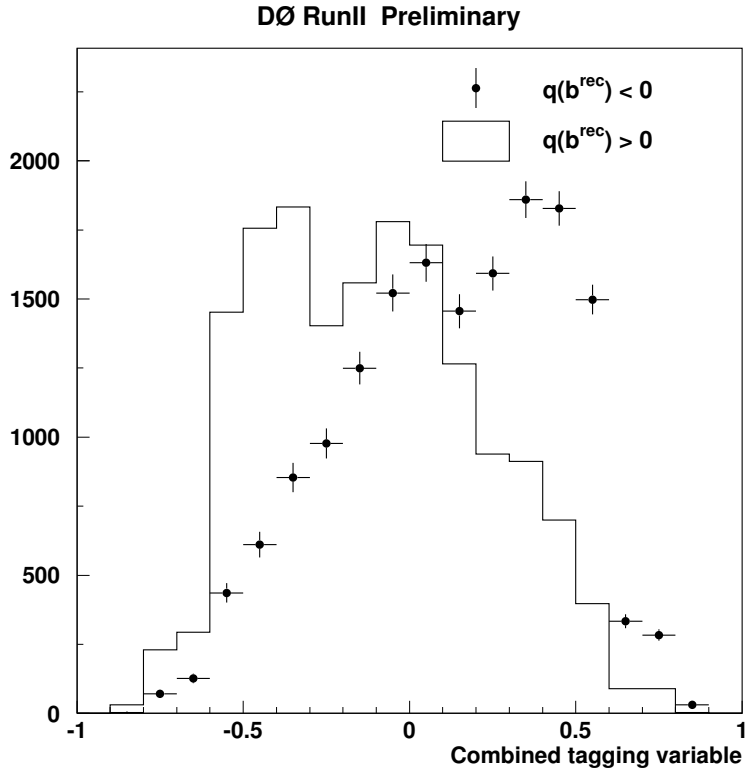

Figure 4.16: Normalized distributions of the combined tagging variable. The $q(b^{rec})$ is the charge of the b quark from the reconstruction side.

The tagging efficiencies shown in Tables 4.7, 4.8 were computed using events with the VPDL=[0.025,0.250]. This selection reduces the contribution from $c\bar{c} \rightarrow \mu^+\nu D^0 X$ events, since they have a VPDL distribution with zero mean and $\sigma \sim 150\mu$m according to our study.

It can be seen from Tables 4.7,4.8 that the dilution of the individual taggers with the same cut on $|d|$ is similar. This is a direct consequence of the chosen tagging method which defines the tagging variable through the ratio of probabilities. It allows a very simple and transparent combination of different taggers into a single variable with a significantly larger tagging power. All taggers give a compatible value of $\Delta \mathrm{m_d}$ and $f_{c\bar{c}}$, as can be seen in Table 4.9. For the combined tagger the following

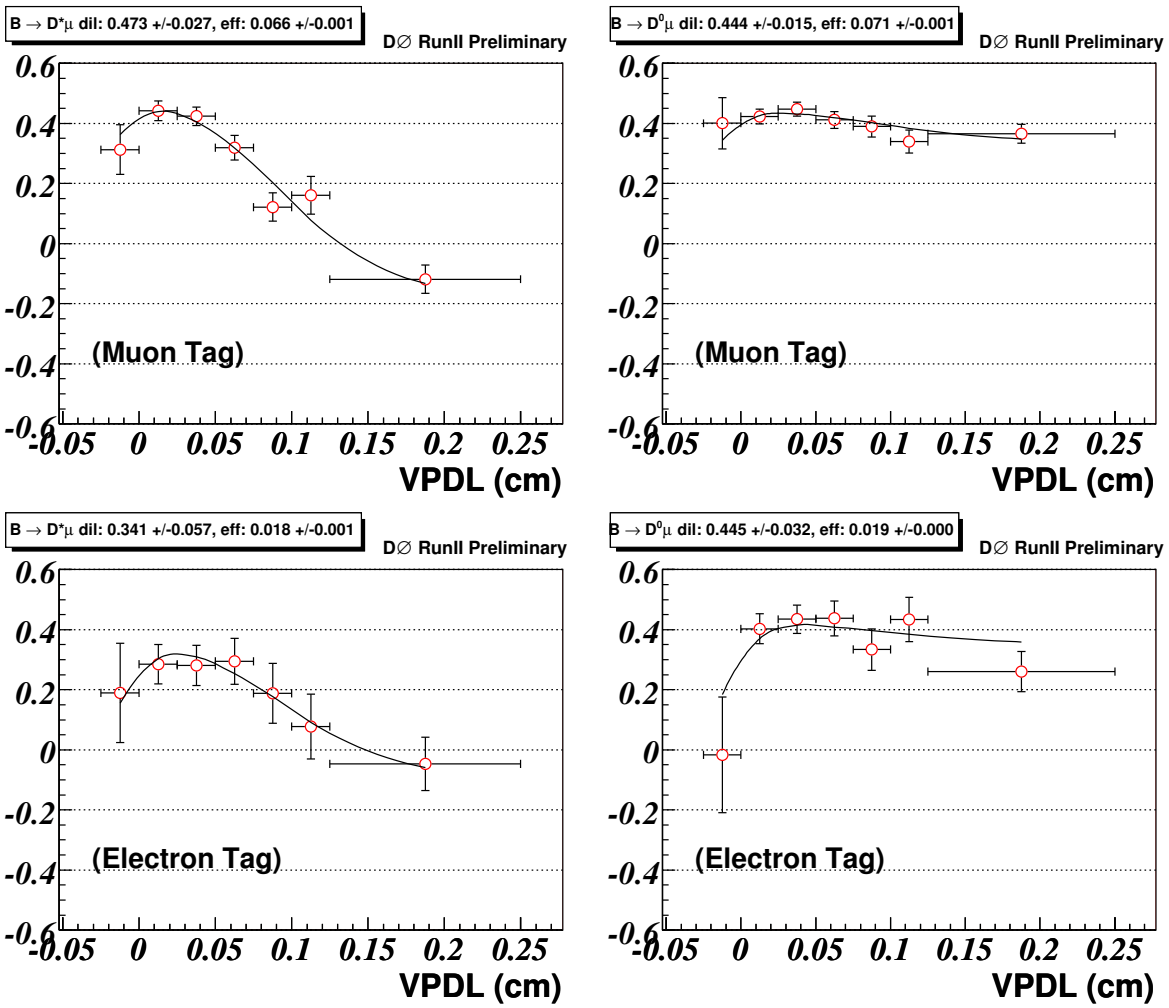

Figure 4.17: The asymmetries obtained in the D* and D^0 sample with the result of the fit superimposed for the Muon and electron tagger. For the individual taggers, $|d| > 0.3$ was required.

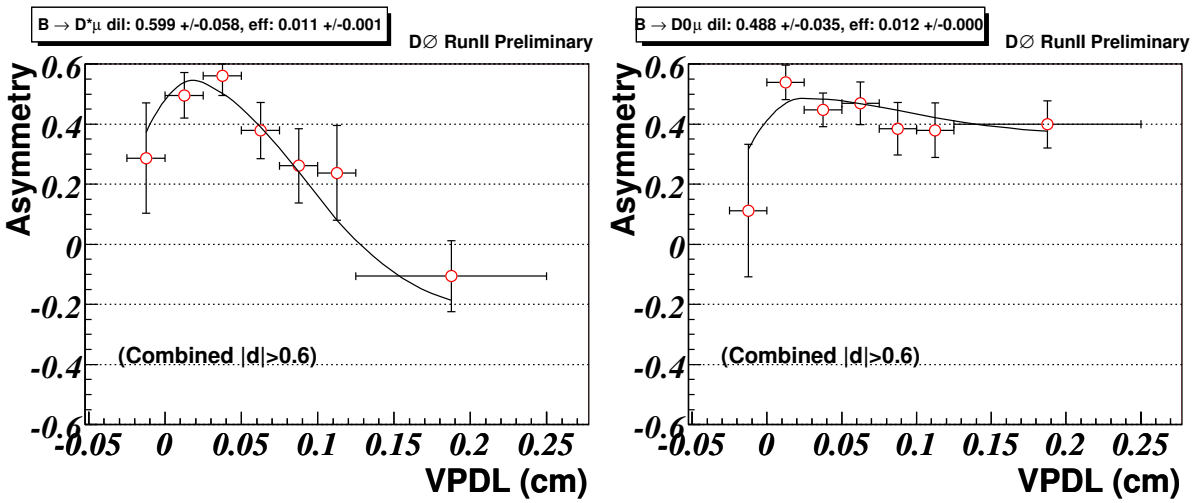

Figure 4.18: The asymmetries obtained in the D^* and D^0 sample with the combined tagger for bin $|d| > 0.6$. The result of the fit is superimposed

results were obtained:

$$\begin{aligned} \varepsilon\mathcal{D}_d^2 &= (2.19 \pm 0.22)(\%) \\ \Delta m_d &= 0.513 \pm 0.023 \\ f_{c\bar{c}} &= (3.3 \pm 1.3)(\%) \end{aligned} \tag{4.23}$$

Tagger	$\varepsilon(\%)$	$\mathcal{D}_d$	$\varepsilon\mathcal{D}_d^2(\%)$
Muon ($\|d\| > 0.3$)	6.61 ± 0.12	0.473 ± 0.027	1.48 ± 0.17
Electron ($\|d\| > 0.3$)	1.83 ± 0.07	0.341 ± 0.058	0.21 ± 0.07
SVCharge ($\|d\| > 0.3$)	2.77 ± 0.08	0.424 ± 0.048	0.50 ± 0.11
Combined ($\|d\| > 0.3$)	11.14 ± 0.15	0.443 ± 0.022	2.19 ± 0.22
Multidim ($\|d\| > 0.37$)	10.98 ± 0.15	0.395 ± 0.022	1.71 ± 0.19
Combined($0.10 < \|d\| < 0.20$)	4.63 ± 0.10	0.084 ± 0.031	0.03 ± 0.02
Combined($0.20 < \|d\| < 0.30$)	5.94 ± 0.12	0.236 ± 0.027	0.33 ± 0.08
Combined($0.30 < \|d\| < 0.45$)	3.89 ± 0.09	0.385 ± 0.034	0.58 ± 0.10
Combined($0.45 < \|d\| < 0.60$)	4.36 ± 0.10	0.512 ± 0.032	1.14 ± 0.14
Combined($0.60 < \|d\| < 1.00$)	1.13 ± 0.05	0.597 ± 0.058	0.40 ± 0.08

Table 4.7: Tagging performance for events with recosntructed B^0 for different taggers and subsamples.

One of the goals of this measurement is to verify the assumption of independence

Tagger	$\varepsilon(\%)$	$\mathcal{D}_u$	$\varepsilon\mathcal{D}_u^2(\%)$	$\mathcal{D}'_d$
Muon ($\|d\| > 0.3$)	7.10 ± 0.09	0.444 ± 0.015	1.400 ± 0.096	0.463 ± 0.028
Electron ($\|d\| > 0.3$)	1.88 ± 0.05	0.445 ± 0.032	0.372 ± 0.054	0.324 ± 0.060
SVCharge ($\|d\| > 0.3$)	2.81 ± 0.06	0.338 ± 0.026	0.320 ± 0.050	0.421 ± 0.049
Combined ($\|d\| > 0.3$)	11.74 ± 0.11	0.419 ± 0.012	2.058 ± 0.121	0.434 ± 0.023
Multidim ($\|d\| > 0.37$)	11.67 ± 0.11	0.363 ± 0.012	1.540 ± 0.106	0.384 ± 0.023
Combined($0.10 < \|d\| < 0.20$)	4.59 ± 0.08	0.104 ± 0.017	0.050 ± 0.016	0.079 ± 0.029
Combined($0.20 < \|d\| < 0.30$)	6.10 ± 0.09	0.234 ± 0.014	0.335 ± 0.042	0.212 ± 0.024
Combined($0.30 < \|d\| < 0.45$)	3.98 ± 0.07	0.361 ± 0.018	0.519 ± 0.052	0.364 ± 0.032
Combined($0.45 < \|d\| < 0.60$)	4.77 ± 0.07	0.504 ± 0.016	1.211 ± 0.077	0.489 ± 0.030
Combined($0.60 < \|d\| < 1.00$)	1.17 ± 0.04	0.498 ± 0.031	0.290 ± 0.038	0.572 ± 0.056

Table 4.8:
Tagging performance for events with recosntructed B^+ for different taggers and subsamples. For comparison, the dilution $\mathcal{D}'_d$ measured in the D^* sample with addition of wrong sign $\mu^+\nu\bar{D}^0\pi^+$ events is also shown.

Tagger	Δm_d	$f_{c\bar{x}}$
Muon	0.502 ± 0.028	0.013 ± 0.010
Electron	0.481 ± 0.067	0.058 ± 0.045
SV Charge	0.553 ± 0.053	0.096 ± 0.050
Multidim	0.502 ± 0.026	0.031 ± 0.014
Combined($\|d\| > 0.3$)	0.513 ± 0.023	0.033 ± 0.013
Combined($0.10 < \|d\| < 0.20$)	0.506 ± 0.209	0.495 ± 0.505
Combined($0.20 < \|d\| < 0.35$)	0.523 ± 0.064	0.021 ± 0.025
Combined($0.35 < \|d\| < 0.45$)	0.531 ± 0.042	0.063 ± 0.038
Combined($0.45 < \|d\| < 0.60$)	0.510 ± 0.032	0.010 ± 0.010
Combined($0.60 < \|d\| < 1.00$)	0.456 ± 0.049	0.032 ± 0.026

Table 4.9: Measured value of Δm_d and $f_{c\bar{c}}$ for different taggers and subsamples.

of the opposite-side flavor tagging on the type of the reconstructed B meson. It can be seen from Tables 4.7,4.8 that the measured flavor tagging performance for B^0 events is slightly better than for B^+ events, both for individual and combined taggers. This difference can be explained by a better selection of $\mu^+\nu\mathrm{D}^{*-}$ events due to an additional requirement of the charge correlation between muon and pion from $\mathrm{D}^{*-} \to D^0\pi^-$ decay. The D^0sample can contain events with a wrongly selected muon. Since the charge of the muon determines the flavor asymmetry, such a background can reduce the measured B^+ dilution. The charge correlation between the muon and the pion can suppress this background and result in a better measurement of the tagging performance.

To test this hypothesis, a special sample of events satisfying all conditions for D^* sample, except the requirement of the charge correlation between the muon and the pion, was selected. The dilution $\mathcal{D}'_d$ for such sample is shown in Table 4.8. It can be seen that $\mathcal{D}'_d$ is statistically compatible with $\mathcal{D}_u$for all samples and all taggers. The χ^2 for the difference in dilutions is found to be 1.06 to be compared to 1.27 in the case where only RS events are considered for the D^* sample.

This result confirms the assumption of the same performance of the opposite-side flavor tagging for B^+ and B^0 events. It also shows that unaccounted contribution of background in the D^0 sample reduces the measured dilution for B^+ events. This background is suppressed by the requirement of the charge correlation between the muon and the pion. Thus, the dilution measured in the D^* sample can be used for the B_s mixing measurement, where a similar charge correlation between the muon and D_s is required.

By construction of the combined tagging, the dilution for any event should strongly depend on the magnitude of the variable d. This property becomes important in the B_s mixing measurement, since in this case the dilution of each event can be estimated using the value of d and can be included in the likelihood function, improving the

sensitivity of the measurement. To test the dependence of dilution on d, all tagged events were divided into subsamples with $0.1 < |d| < 0.2$, $0.2 < |d| < 0.35$, $0.35 < |d| < 0.45$, $0.45 < |d| < 0.6$, and $|d| > 0.6$. The overall efficiency of this sample is $(19.95 \pm 0.21)(\%)$. The obtained dilutions are shown in Table 4.7. Their strong dependence on the value of the tagging variable is clearly seen. The overall tagging power, computed as the sum of tagging powers of all subsamples is:

$$\varepsilon \mathcal{D}_d^2 = (2.48 \pm 0.21)(\%) \tag{4.24}$$

The measured oscillation parameter Δm_d for all considered taggers and subsamples is given in Table 4.9. It is compatible with the world average value $\Delta m_d = 0.509 \pm 0.004$ ps^{-1}.

Finally, the mixing parameter Δm_d was obtained from the simultaneous fit of the flavor asymmetry in the above defined subsamples. The fraction $f_{c\bar{c}}$ was constrained to be the same for all subsamples. The obtained result is:

$$\begin{aligned} \Delta m_d &= 0.506 \pm 0.020 \\ f_{c\bar{c}} &= (2.2 \pm 0.9)(\%) \end{aligned} \tag{4.25}$$

The statistical precision of Δm_d from the simultaneous fit is about 10% better than that from the fit of events with $|d| > 0.3$. This improvement is directly related with a better overall tagging power (4.24) for the sum of subsamples as compared to the result (4.23) for the sample with $|d| > 0.3$.

4.15 Conclusions

A study of the likelihood-based opposite-side tagging algorithm in B^0 and B^+ samples was performed. The dilutions $\mathcal{D}(B^+)$ and $\mathcal{D}(B^0)$ are consistent within their statistical

errors.

Splitting the sample into bins, according to the tagging variable $|d|$ and measuring the tagging power as the sum of individual tagging power in all bins we obtained

$$\varepsilon\mathcal{D}^2 = (2.48 \pm 0.21 \text{ (stat.)}^{+0.08}_{-0.06} \text{ (syst)}) \text{ (\%)}$$

From a simultaneous fit to events in all $|d|$ bins we measured the mixing parameter Δm_d parameter: $\Delta m_d = 0.506 \pm 0.020 \text{ (stat)} \pm 0.016 \text{ (syst) ps}^{-1}$ which is in good agreement with the world average value of $\Delta m_d = 0.509 \pm 0.004 \text{ ps}^{-1}$ [49].

Chapter 5

B_s^0 Mixing Analysis

5.1 Introduction

In this chapter, we discuss the mixing analysis done in $B_s^0 \to D_s^- \mu^+ X$ with D_s decaying to $D_s^- \to K^{*0} K^-$ ($K^{*0} \to K^+ \pi^-$) final state with ~ 1.2 fb^{-1} of data collected with the DØ detector during Run II of the Fermilab Tevatron [51, 52]. At DØ, we already have set a two sided bound on the mixing parameter using our large semileptonic data sample which was later confirmed by the CDF experiment. The recent double sided bound on B_s mixing by the $D\emptyset$ collaboration [16] and its confirmation later by CDF collaboration [17] has led to a lot of excitement and enthusiasm in the Flavor Physics sector. This has provided a very good opportunity to these experiments to measure the B_s oscillations as precisely as possible before the LHC comes into operation. $D\emptyset$ put a double sided bound on the B_s mixing oscillation between $17.0 < \Delta m_s < 21.0$ ps^{-1} at the 90% confidence level with a most probable value of $\Delta m_s = 19$ ps^{-1}. CDF measures this oscillation as $\Delta m_s = 17.31^{+0.33}_{-0.18}(stat.) \pm 0.07(sys)$ ps^{-1}. It is an important test of the CKM formalism of the Standard Model, and combining it with a measurement of Δm$_{\rm d}$ will allow us to reduce the theoretical error on the CKM matrix element V_{td}. If the Standard Model is correct, then Δm$_{\rm s} = 18.3^{+6.5}_{-1.5}$ ps^{-1} from global fits to the unitarity triangle

if the current experimental limits on Δm_s are included in the fit. If information from B_s^0 oscillations limits are not included, global fits give $\Delta m_s = 20.9^{+4.5}_{-4.2}$ ps^{-1} [50]. The current measurements indicate a value well within the SM allowed range and small enough to allow us to measure Δm_s with semileptonic decays.

5.2 Event Selection

All tracks in an event were clustered into jets using the DURHAM clustering algorithm [53] with the cutoff parameter of 15 GeV/c. The following requirements were made to identify the $B_s^0 \to D_s^- \mu^+ X$, $D_s^- \to K^{*0} K^-$, $K^{*0} \to K^+ \pi^-$ decay chain. The muon was identified using the standard DØ algorithm [54]. It was required to have $p_T > 2$ GeV/c and $p > 3$ GeV/c, to have hits in both the CFT and SMT and to have at least 2 measurements in the muon chambers. Particles were assigned the masses of kaons (K_1 and K_2) and pion requiring the charge combination $\mu^+ K_1^+ K_2^- \pi^-$ or its charge conjugate. For the $D_s \to K^* K$ channel, transverse momenta were required to be: $p_T(K_1) > 0.9$ GeV/c, $p_T(K_2) > 1.8$ GeV/c and $p_T(\pi) > 0.5$ GeV/c, assuming that K_1 comes from the $K^{*0} \to K^+ \pi^-$ decay.

For each particle, the transverse[1] ϵ_T and longitudinal[2] ϵ_L projections of track impact parameter with respect to the primary vertex together with the corresponding errors ($\sigma(\epsilon_T)$, $\sigma(\epsilon_L)$) were computed. The combined significance $(\epsilon_T/\sigma(\epsilon_T))^2 + (\epsilon_L/\sigma(\epsilon_L))^2$ was required to be greater than 4 for K_1 and K_2, while there was no cut on the significance of the pion.

Three charged particles were required to come from the same D_s^- vertex with the χ^2 of the vertex fit satisfying $\chi^2 < 16$. The D_s^- candidate produced by their combination was required to have a common B vertex with the muon with the χ^2 of the vertex fit such that $\chi^2 < 9$. The mass of the $\mu^+ D_s^-$ system was required to be

[1] in the plane perpendicular to the beam direction.
[2] parallel to the beam direction.

$2.6 < M(\mu^+ D_s^-) < 5.4$ GeV/c^2. The distance d_T^D in the axial plane between the D_s^- vertex and the primary interaction point was required to satisfy $d_T^D/\sigma(d_T^D) > 4$. The angle α_T^D between the momentum direction of the D_s^- candidate and the direction from the primary to the D_s^- vertex in the axial plane was required to fulfill the condition: $\cos(\alpha_T^D) > 0.9$.

If the distance d_T^B between the primary and B_s^0 vertex in the axial plane exceeded $4 \cdot \sigma(d_T^B)$, the angle α_T^B between the B_s^0 momentum and the direction from the primary to B_s^0 vertex in the axial plane was required to satisfy the condition: $\cos(\alpha_T^B) > 0.95$. The distance d_T^B was allowed to be greater than d_T^D, provided that the distance between the B_s^0 and D_s^- vertices d_T^{BD} was less than $2 \cdot \sigma(d_T^{BD})$.

Additionally, for the $D_s^- \to K^{*0} K^-$ channel, the condition $0.82 < M(K_1\pi) < 0.95$ was applied. The final event samples were selected using the likelihood ratio method, described below.

It is assumed that a set of discriminating variables $x_1, ...x_n$ can be constructed for a given event. It is also assumed that the probability density functions $f^s(x_i)$ for the signal and $f^b(x_i)$ for the background can be built for each variable x_i. The combined tagging variable y is defined as:

$$y = \prod_{i=1}^{n} y_i; \quad y_i = \frac{f_i^b(x_i)}{f_i^s(x_i)}. \tag{5.1}$$

The selection of the signal is obtained by applying the cut on $y < y_0$. For uncorrelated variables $x_1, ...x_n$, the selection using the combined variable y gives the best possible tagging performance, i.e., maximal signal efficiency for a given background efficiency.

The following discriminating variables were used:

- Helicity angle, defined as the angle between the D_s^- and K_1 momenta in the $(K_1\pi)$ center of mass system,

- Isolation, computed as $Iso = p^{tot}(\mu D_s)/(p^{tot}(\mu D_s) + \sum p_i^{tot})$. The sum $\sum p_i^{tot}$

was taken over all charged particles in the cone $\sqrt{(\Delta\phi)^2 + (\Delta\eta)^2} < 0.5$, where $\Delta\eta$ and $\Delta\phi$ are the pseudorapidity and the azimuthal angle with respect to the (μD_s) direction. The μ^+, K_1, K_2 and π^- were not included in the sum,

- $p_T(K_2)$,
- Invariant mass, $M(\mu^+ D_s^-)$,
- χ^2 of the D_s^- vertex fit,
- $M(K_1\pi)$.

The probability density functions were constructed using real data events. For each channel, three bands B_1, B_2 and S were defined as:

$$\begin{aligned} B_1 &: 1.75 < M(D_s^-) < 1.79 \text{ GeV}/c^2 \\ B_2 &: 2.13 < M(D_s^-) < 2.17 \text{ GeV}/c^2 \\ S &: 1.92 < M(D_s^-) < 2.00 \text{ GeV}/c^2 \end{aligned}$$

The background probability density function for each variable was constructed using events from the B_1 and B_2 bands. The signal probability density function was constructed by subtracting the background, obtained as a sum of distributions in the B_1 and B_2 bands, from the distribution of events in band S. The final selection of events for the analysis was done by applying a cut on the combined variable $\log_{10} y < 0.16$. This cut was selected by requiring the maximal value of $S/\sqrt{S + B_1 + B_2}$.

Figure 5.1 shows the $K^{*0}K^-$ invariant mass distribution after all the selection cuts. Distributions for both the "right-sign" $D_s^-\mu^+$ combinations $(Q_\mu * Q_\pi < 0)$ and the "wrong-sign" $D_s^-\mu^-$ combinations $(Q_\mu * Q_\pi > 0)$ are shown.

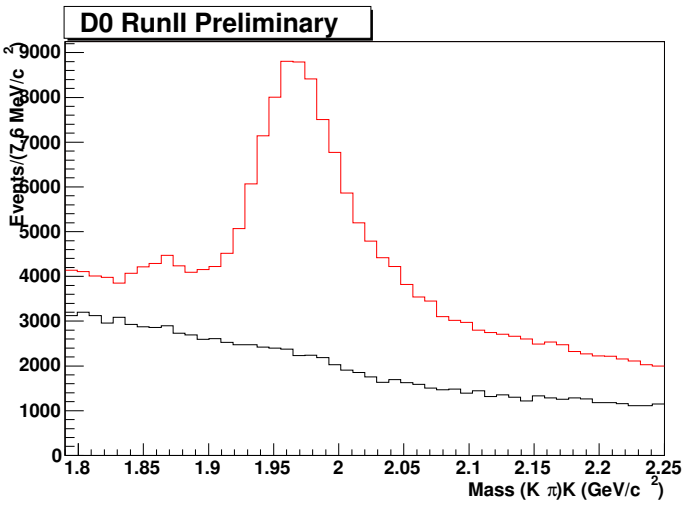

Figure 5.1: Distribution of the mass of $D_s^- \to K^{*0}K^-$ candidates. Both "right-sign" (red) and "wrong-sign" (black) combinations are shown.

5.3 Mass Fitting Procedure

In the decays $D^- \to K^+\pi^-\pi^-$, when the pion is mis-identified as a kaon it peaks right under the $D_s^- \to K^{*0}K^-$ signal peak and this peak strongly overlaps. The final state $KK\pi$ mass spectrum could be a mixture of many different decays so the shape of reflection $D^- \to K^+\pi^-\pi^-$ strongly depends on kinematical properties of events and changes for different selections. Due to large reflections coming from the mis-identification of pion track as a kaon track, extracting the signal becomes very difficult in $D_s^- \to K^{*0}K^-$ decays. In order to separate the signal from the large reflection we developed an event-by-event fit based on the kinematic properties of the events. The details of the unbinned mass fitting procedure is as follows:

Consider the decay $D^- \to K^+\pi^-\pi^-$. The mass of $K\pi\pi$ system is given as:

$$M_D^2 = (E_{K\pi} + E_\pi)^2 - (\vec{P}_{K\pi} + \vec{P}_\pi)^2 \tag{5.2}$$

where $E_{K\pi}$ is the energy of $(K^-\pi^+)$ and E_π, P_π is the energy and momentum of the

second pion respectively. $E_\pi = \sqrt{P_{Tr}^2 + M_\pi^2}$, is the energy of track assuming the pion mass hypothesis,

When this pion is assigned the mass of Kaon, the shifted mass of $K\pi$"K" system is

$$M_R^2 = (E_{K\pi} + E_K)^2 - (\vec{P}_{K\pi} + \vec{P}_K)^2 \tag{5.3}$$

$$\vec{P}_K = \vec{P}_\pi = \vec{P}_{Tr} \tag{5.4}$$

where, $E_K = \sqrt{P_{Tr}^2 + M_K^2}$ is the energy of the track assuming the kaon mass hypothesis.

We can express M_R as:

$$M_R^2 = M_D^2 + (E_{K\pi} + E_K)^2 - (E_{K\pi} + E_\pi)^2 \tag{5.5}$$

$$M_R^2 = M_D^2 + (M_K^2 - M_\pi^2) + 2E_{K\pi}(E_K - E_\pi) \tag{5.6}$$

$$M_R^2 = M_D^2 + (1 + 2R)(M_K^2 - M_\pi^2) \tag{5.7}$$

where,

$$R = \frac{E_{K\pi}(E_K - E_\pi)}{(M_K^2 - M_\pi^2)} \tag{5.8}$$

is the reflection variable.

A similar equation can be written for reflection due to $\Lambda_c \rightarrow K^+\pi^-P^+$, where the proton can be mis-identified as kaon. From equation 5.8, we see that the shifted mass depends on kinematic properties of the events but for a given $E_{K\pi}$ and P_{Tr}, the shift is constant. Also, for a given $E_{K\pi}$ and P_{Tr} the mass distribution of the reflection is determined only by the detector resolution and can be approximated by a Gaussian. Figure 5.2 shows the distribution of the R variable for signal and reflection MC samples. From the figure we can see that the shape of R variable for signal and reflection are very similar. Figure 5.3 shows the distribution of $(K\pi)K$ mass system

in different bins of R variable. From these plots, it can be seen that the shape of the combinatoric background changes significantly with R.

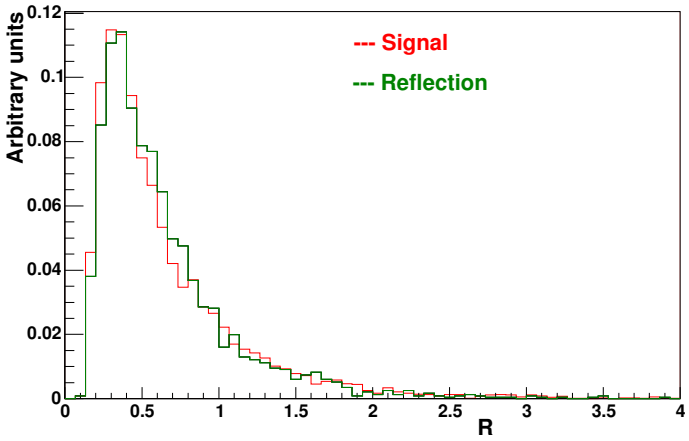

Figure 5.2: Distribution of the reflection variable R for both signal (red) and D^+ reflection (green) MC.

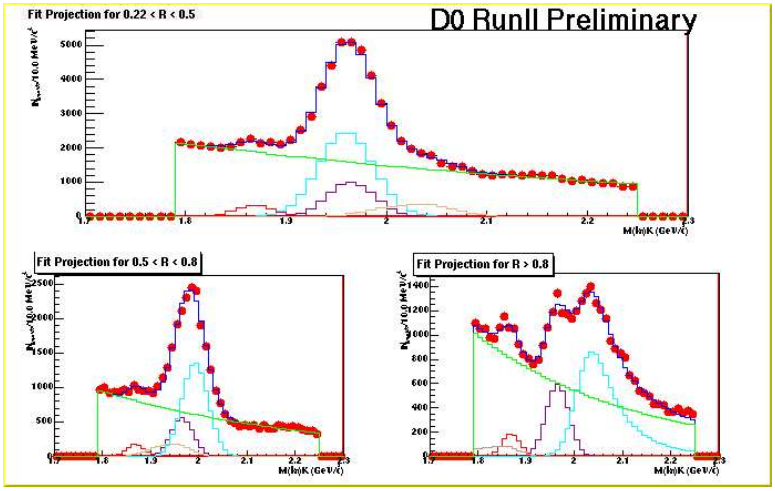

Figure 5.3: Distribution of $(K\pi)K$ mass in three different bins of the variable R with the fit results overlayed. The individual histograms at the bottom show the different components separately.

The $(K\pi)K$ mass range of $M_{min} = 1.79$ GeV to $M_{max} = 2.25$ GeV was chosen for fit. Four decay channels which include two signal and two physics background channels and combinatoric background were considered as follows:

- $D_s^- \rightarrow K^{*0}K^-$ (The signal) with fraction f_{sig}.

- $D^+ \to K\pi\pi$ or $D^+ \to K^{*0}\pi(K^{*0} \to K^+\pi^-)$ (Reflection) with fraction f_{Dr}.
- $\Lambda_c^+ \to K^+\pi^- P^+$ (Reflection) with fraction f_{Lr}.
- $D^+ \to K^{*0}K^+(K^{*0} \to K^+\pi^-)$ (Cabbibo suppressed decay) with fraction f_{Dp}.
- Combinatorial background with fraction $(1 - f_{sig} - f_{Dr} - f_{Lr} - f_{Dp})$.

For each event i with given value of R, the *pdf* of a given channel j is given as:

$$P_i^j(M) = \frac{1}{\sqrt{2\pi}\sigma_j} \cdot exp\left(-\frac{\left(M - M_i^j(R_i)\right)^2}{2\sigma_j^2}\right) \tag{5.9}$$

where M_i^j is the shifted mass defined in equation 5.7.
The fraction of each channel is given by

$$f_i^j = f_0^j \cdot C(R) \cdot N_i^j \tag{5.10}$$

We introduce the term C(R) to allow the change of channel fraction f_i^j with R. C(R) is parameterized as

$$C(R) = 1.0 + R \cdot p0 + R^2 \cdot p1 \tag{5.11}$$

Here p0 and p1 are parameters returned by the fit. See table 5.2 for the values of these parameters. The distribution of C(R) is given in Fig. 5.4. Normalization coefficient N_i^j takes into account that for a given event i and given channel j, a part of *pdf* P_i^j can be outside the selection range $1.79 < M(K\pi K) < 2.25$ and hence renormalizes the *pdf* as,

$$N_i^j = \int_{M_{min}}^{M_{max}} dM \; P_i^j(M). \tag{5.12}$$

The background *pdf* is given as exponential

$$P_{bkg}(M) = \frac{1}{N_{bkg}} \cdot exp\left(-\frac{M}{M_0(R)}\right) \tag{5.13}$$

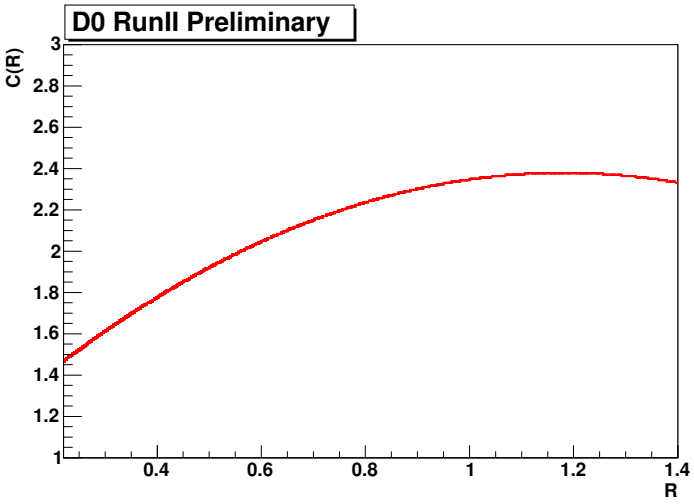

Figure 5.4: Distribution of C(R).

where we allow the slope $M_0(R)$ to change with R. Here N_{bkg} is the normalization constant. We parameterize this variation by a polynomial

$$M_0(R) = p2 \cdot (1.0 + R \cdot p3 + R^2 \cdot p4 + R^3 \cdot p5 + R^4 \cdot p6) \tag{5.14}$$

where, p2, p3, p4, p5 and p6 are the free parameters in the fit (see table 5.2 for the values of these parameters). The distribution of $M_0(R)$ is given in Fig. 5.5. The total

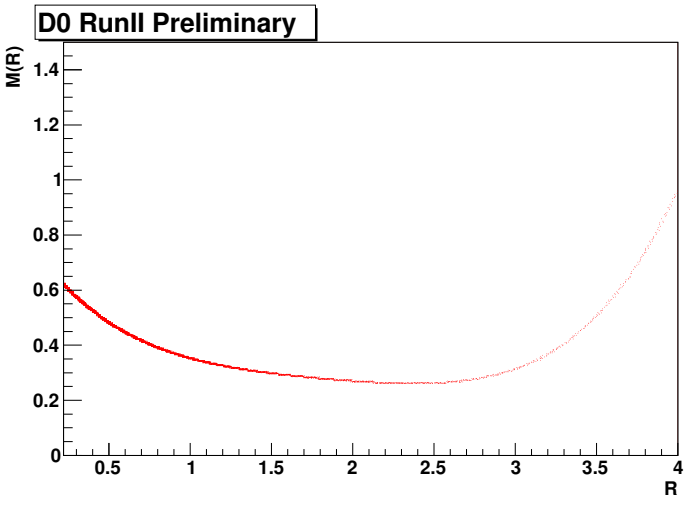

Figure 5.5: Distribution of $M_0(R)$.

likelihood is given as

$$L_n = \Pi_i \left(\sum_j f_i^j \cdot P_i^j + f_{bkg} \cdot P_{bkg} \right) \tag{5.15}$$

where,

$$f_{bkg} = (1 - \sum_j f_i^j) \tag{5.16}$$

The following form is being minimized using the MINUIT program:

$$\mathcal{L} = -2 \cdot \ln L_n. \tag{5.17}$$

For small values of R the kinematical threshold distort the shape of the background

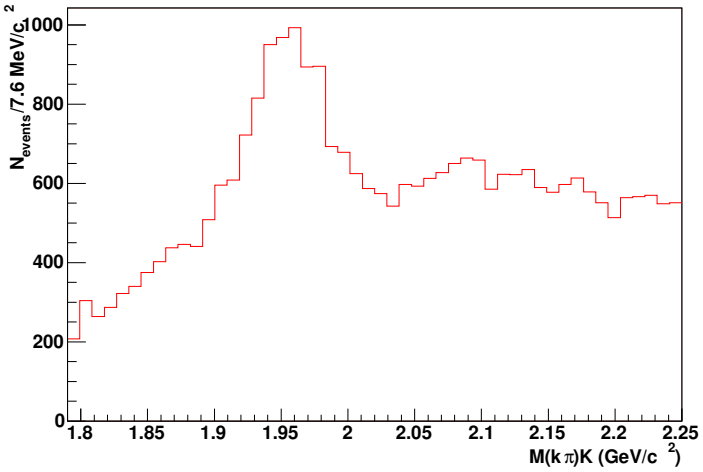

Figure 5.6: Distribution of $(K\pi)K$ mass for $R < 0.22$. The background shape is quite different in this region.

and it can not be described by an exponential any more as can be seen in Fig. 5.6. That is why in this analysis we use events with $R > 0.22$ only. We checked that for $R > 0.22$ the distortion of the background by threshold effects is negligible. Unless stated otherwise, all the figures sensitive to the R variable and final results in this analysis were obtained for $R > 0.22$.

The fitting program was run for all the untagged events and allowing all the parameters to float. The resulting fit can be seen in the Figure 5.7. We obtain 12647 ± 740 signal candidates, 35937 ± 1856 D^+ reflection candidates, 3232 ± 258 Cabbibo suppressed candidates and 5820 ± 397 Λ_c candidates. Once we obtained the yields for the total untagged sample we then fix all the parameters except the fraction of events in different components and parameter p2 in order to estimate the yields for the tagged, unmixed and mixed candidates. We observe that the ratio of events in Cabbibo suppressed decay to D^+ reflection is constant within errors for untagged, tagged, mixed and unmixed samples. This is another cross check of the validity of the fit as this ratio is supposed to be constant irrespective of the sample. We fix this ratio from the total untagged sample in the fit for the tagged sample. Table 5.1 shows the masses, widths and fractions obtained from the mass fit for the total untagged sample.

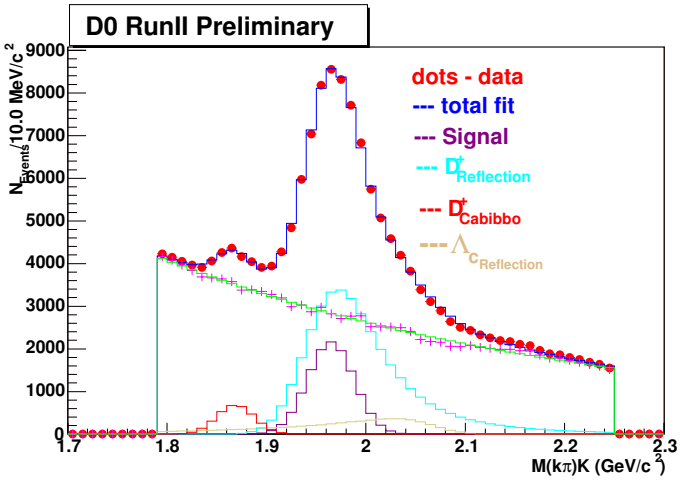

Figure 5.7: Fit to the total untagged sample, dots represents the data points and histogram is the fit result.In this plot, dark blue histogram shows the signal component, light blue is the $D^{\pm}$ reflection, magenta is the cabbibo $D^{\pm}$ decay and golden color is for the component due to Λ_c reflection. The red crosses are the signal subtracted background and the green line is the fit to the combinatoric background.

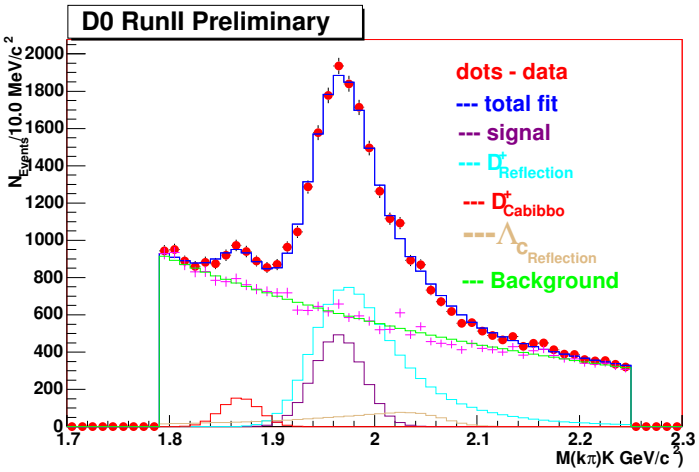

Figure 5.8: Fit to the total tagged sample, dots represents the data points and histogram is the fit result.

Table 5.1: Fit parameters from the mass fit

Decay Channel	Mass (GeV/c^2)	Width (MeV/c^2)	Fractions
$D_s^- \to K^{*0}K^-$	1.9647 ± 0.0006	25.76 ± 0.05	0.036 ± 0.0021
$D^+ \to K^+\pi^-\pi^+$	1.8603 ± 0.0002	23.34 ± 0.62	0.105 ± 0.0054
$D^+ \to K^{*0}K^+$	1.8688 ± 0.0013	18.77 ± 1.15	0.009 ± 0.0007
$\Lambda_c^+ \to K^+\pi^- P^+$	2.2779 ± 0.0009	22.81 ± 0.92	0.020 ± 0.0013

5.4 Initial State Flavor Tagging

In order to measure the mixing oscillations, we need to determine whether a B_s^0 has mixed or not. To know the initial flavor of the B_s^0 mesons, an Initial State Flavor Tagging technique was used as described in Chapter 4. The second B meson (or

Table 5.2: Parameters for background slope and signal fraction parameterization

Parameter	Value
P0	2.332 ± 0.279
p1	-0.987 ± 0.149
P2	0.781 ± 0.012
P3	-1.087 ± 0.006
P4	0.772 ± 0.003
P5	-0.270 ± 0.001
P6	0.037 ± 0.0005

baryon) in the event was used to tag the initial flavor of the reconstructed B^0 meson. The tagging technique utilized information from identified leptons (muons and electrons) and reconstructed secondary vertices. For reconstructed $B_s^0 \to D_s^- \mu^+ X$ decays both leptons having the same sign would indicate that one B hadron had oscillated while opposite signs would indicate that neither (or both) had oscillated. The flavor taggings discussed in Chapter 4 has been used for the B_s^0 mixing analysis and the details can be found in reference [57].

An important property of opposite-side tagging is the independence of its performance on the type of the reconstructed B meson, since the hadronization of the two b quarks is not correlated in $p\bar{p}$ interactions. Therefore, the flavor tagging algorithm can be calibrated in data by applying it to the events with the B^0 and B^+ decays. The measured performance can then be used in the study of B_s meson oscillations. This tagging method was tested and calibrated extensively on both Monte Carlo and real $B \to \mu^+ \nu \mathrm{D}^{*-}$ events, as discussed in Chapter 4. Fits to the asymmetry distribution, in various ranges of $|d|$ for these events show clear B_d oscillations with $\Delta \mathrm{m_d}$ values consistent with the world average value [1]. Figure 5.8 shows the fit for the total B_s^0 tagged sample. We obtain a total of 2997 ± 146 tagged signal candidates, 8208 ± 145 tagged D^+ reflection candidates, 1261 ± 89 tagged Λ_c events and and 732 Cabbibo suppressed candidates.

5.5 Unbinned Likelihood Fit Method

An event-by-event fit was developed to perform the B_s amplitude scan analysis. For the details of the unbinned method, see [56]. All tagged events in the mass range of $1.79 < M_{(KK)\pi} < 2.25$ GeV/c^2 were used in the unbinned likelihood fitting procedure.

The likelihood for an event to arise from a specific source in the sample depends on the x^M, its error (σ_{x^M}), the mass of the $\mathrm{D_s^-}$meson candidate (m) and the predicted

dilution (d_{pr}). All these quantities are known on an event-by-event basis. The *pdf* for each source can be expressed by the following formula:

$$f_i = P_i^{x^M}(x^M, \sigma_{x^M}, d_{pr}) P_i^{\sigma_{x^M}} P_i^m P_i^{d_{pr}} P_i^y. \tag{5.18}$$

The function $P_i^{\sigma_{x^M}}$ is the *pdf* for Visible Proper Decay Length (VPDL) uncertainty, P_i^m is the mass *pdf* obtained from the mass fitting procedure, $P_i^{d_{pr}}$ is the *pdf* for the dilution and P_i^y is the selection variable y *pdf*. The function $P_i^{x^M}(x^M, \sigma_{x^M}, d_{pr})$ will be defined later.

The following sources were considered for the entire mass region:

- $\mu D_s(\rightarrow K^{*0}K)$ signal with fraction $Fr_{\mu D_s}$.
- $\mu D^{\pm}(\rightarrow K^{*0}K)$ signal with fraction $Fr_{\mu D^{\pm}}$.
- $\mu D^{\pm}(\rightarrow K\pi\pi)$ reflection with fraction $Fr_{\mu D^{\pm}_{refl}}$.
- $\mu\Lambda^{\pm}(\rightarrow K\pi P)$ reflection with fraction $Fr_{\mu\Lambda^{\pm}_{refl}}$.
- Combinatorial background with fraction $(1 - Fr_{\mu D_s} - Fr_{\mu D^{\pm}} - Fr_{\mu D^{\pm}_{refl}} - Fr_{\mu\Lambda^{\pm}_{refl}})$.

The fractions $Fr_{\mu D_s}$, $Fr_{\mu D^{\pm}}$, $Fr_{\mu D^{\pm}_{refl}}$ and $Fr_{\mu\Lambda^{\pm}_{refl}}$ were determined from the mass fit (see Fig. 5.8). The total *pdf* for a B candidate has the form:

$$\begin{aligned} F_n = Fr_{\mu D_s} f_{\mu D_s} + Fr_{\mu D^{\pm}} f_{\mu D^{\pm}} + Fr_{\mu D^{\pm}_{refl}} f_{\mu D^{\pm}_{refl}} + Fr_{\mu\Lambda^{\pm}_{refl}} f_{\mu\Lambda^{\pm}_{refl}} + \\ \left(1 - Fr_{\mu D_s} - Fr_{\mu D^{\pm}} - Fr_{\mu D^{\pm}_{refl}} - Fr_{\mu\Lambda^{\pm}_{refl}}\right) f_{bkg} \end{aligned} \tag{5.19}$$

The following form is being minimized using the MINUIT program:

$$\mathcal{L} = -2 \sum_{n=1}^{N_{candidates}} \ln F_n \tag{5.20}$$

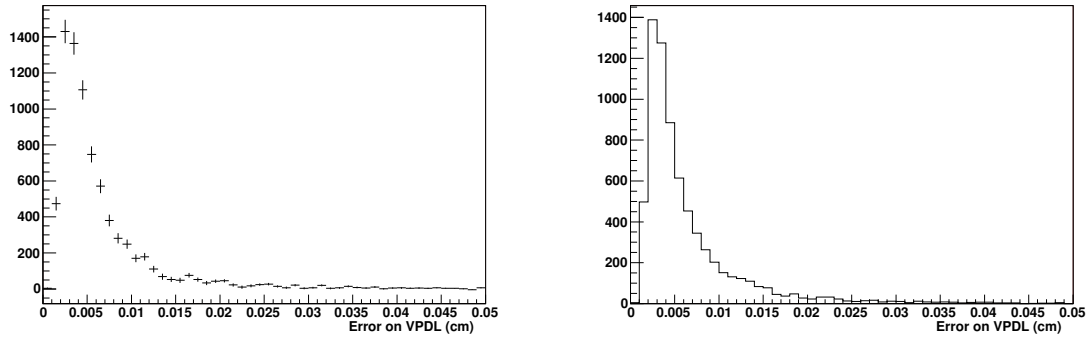

Figure 5.9: Distributions of VPDL errors for signal and combinatorial background.

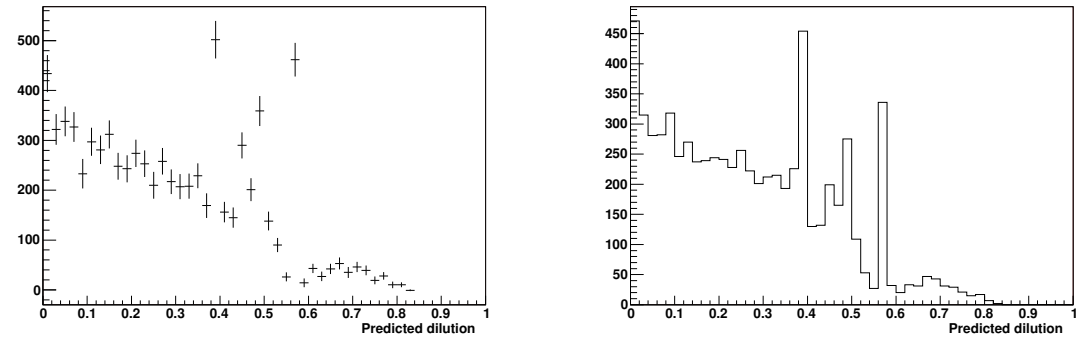

Figure 5.10: Distributions of predicted dilution for signal and combinatorial background.

The distributions for the VPDL error, (Fig. 5.9), mass (Fig. 5.8), dilution (Fig. 5.10) and Ctag (Fig. 5.11) are taken from experimental data (here, Ctag is the selection variable y defined in equation 5.1). The *pdf*s for these quantities were obtained by normalizing the above distributions. The signal *pdf*s were also used for the $\mu D^{\pm}(\rightarrow K\pi\pi)$

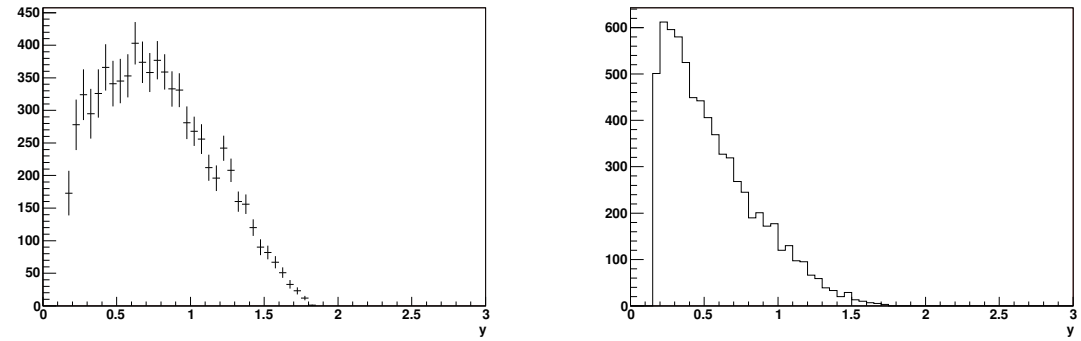

Figure 5.11: Distributions of selection variable for signal and combinatorial background.

signal, the $\mu D^{\pm}(\rightarrow K\pi\pi)$ reflection and $\mu\Lambda_c^{\pm} \rightarrow (K\pi P)$ reflection.

5.5.1 *pdf* for μD_s Signal

The μD_s sample is composed mostly of $\mathrm{B_s^0}$ mesons with some contributions from B_u and B_d mesons. Different species of B mesons behave differently with respect to oscillations. Neutral B_d and B_s mesons do oscillate (with different frequencies) while charged B_u mesons do not.

For a given type of B hadron (i.e., d, u, s) or b-baryon, the distribution of the visible proper decay length x is given by:

$$p_s^{nos}(x,K,d_{pr}) = \frac{K}{c\tau_{B_s}}\exp(-\frac{Kx}{c\tau_{B_s}})\cdot 0.5\cdot(1+\mathcal{D}(d_{pr})\cos(\Delta m_s\cdot Kx/c)) \tag{5.21}$$

$$p_s^{osc}(x,K,d_{pr}) = \frac{K}{c\tau_{B_s}}\exp(-\frac{Kx}{c\tau_{B_s}})\cdot 0.5\cdot(1-\mathcal{D}(d_{pr})\cos(\Delta m_s\cdot Kx/c)) \tag{5.22}$$

$$p_{DsDs}^{osc}(x,K) = \frac{K}{c\tau_{B_s}}\exp(-\frac{Kx}{c\tau_{B_s}})\cdot 0.5 \tag{5.23}$$

$$p_{DsDs}^{nos}(x,K) = \frac{K}{c\tau_{B_s}}\exp(-\frac{Kx}{c\tau_{B_s}})\cdot 0.5 \tag{5.24}$$

$$p_u^{nos}(x,K,d_{pr}) = \frac{K}{c\tau_{B_u}}\exp(-\frac{Kx}{c\tau_{B_u}})\cdot 0.5\cdot(1-\mathcal{D}(d_{pr})) \tag{5.25}$$

$$p_u^{osc}(x,K,d_{pr}) = \frac{K}{c\tau_{B_u}}\exp(-\frac{Kx}{c\tau_{B_u}})\cdot 0.5\cdot(1+\mathcal{D}(d_{pr})) \tag{5.26}$$

$$p_d^{nos}(x,K,d_{pr}) = \frac{K}{c\tau_{B_d}}\exp(-\frac{Kx}{c\tau_{B_d}})\cdot 0.5\cdot(1-\mathcal{D}(d_{pr})\cos(\Delta m_d\cdot Kx/c)) \tag{5.27}$$

$$p_d^{osc}(x,K,d_{pr}) = \frac{K}{c\tau_{B_d}}\exp(-\frac{Kx}{c\tau_{B_d}})\cdot 0.5\cdot(1+\mathcal{D}(d_{pr})\cos(\Delta m_d\cdot Kx/c)) \tag{5.28}$$

$$p_\Lambda^{nos}(x,K,d_{pr}) = \frac{K}{c\tau_{\Lambda}}\exp(-\frac{Kx}{c\tau_{\Lambda}})\cdot 0.5\cdot(1-\mathcal{D}(d_{pr})) \tag{5.29}$$

$$p_\Lambda^{osc}(x,K,d_{pr}) = \frac{K}{c\tau_{\Lambda}}\exp(-\frac{Kx}{c\tau_{\Lambda}})\cdot 0.5\cdot(1+\mathcal{D}(d_{pr})) \tag{5.30}$$

where
$$K = P_T^{\mu \mathrm{D_s^-}} / P_T^B, \tag{5.31}$$

$$\mathcal{D}(d_{pr})\Big|_{d_{pr}<0.6} = 0.457 \cdot |d_{pr}| + 2.349 \cdot |d_{pr}|^2 - 2.498 \cdot |d_{pr}|^3, \tag{5.32}$$

$$\mathcal{D}(d_{pr})\Big|_{d_{pr}>0.6} = 0.6 \text{ (see Fig. 5.12).}$$

Here τ is the lifetime of the B hadron and or b baryon and K is the Kfactor, which

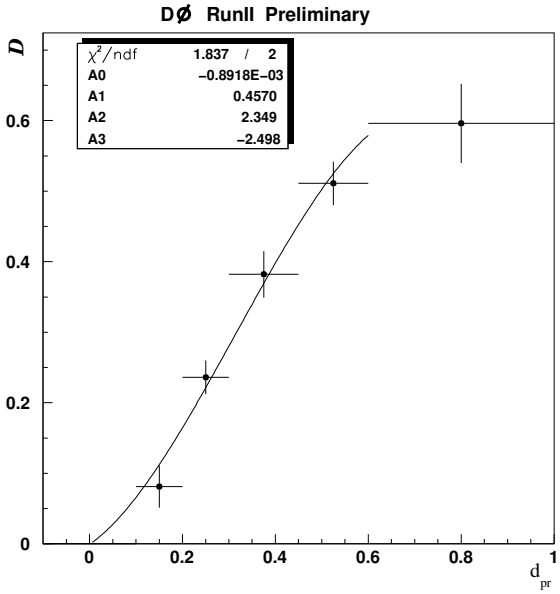

Figure 5.12: Dilution calibration.

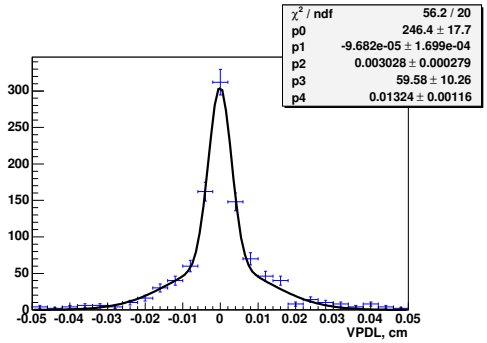

Figure 5.13: VPDL distribution for the peaking background.

reflects the difference between the observable and true momenta of the B-hadron. Note that there is a sign swap in Eq. 5.25–5.28 with respect to 5.21 and 5.22 due to anti-correlation of charge for muons from $B \to DD_s$; $D \to \mu X$ processes.

The translation to the measured VPDL, x^M is achieved by a convolution of the K factors and resolution functions as specified below.

$$P^{osc,\ nos}_{(d,u,s,\Lambda),\ j}(x^M, \sigma_{x^M}, d_{pr}) = \int_{K_{min}}^{K_{max}} dK\ D_j(K) \cdot \frac{Eff_j(x^M)}{N_j(K, \sigma_{x^M}, d_{pr})} \int_0^\infty dx\ G(x - x^M, \sigma_{x^M}) \cdot p^{osc,\ nos}_{(d,u,s,\Lambda),\ j}(x, K, d_{pr}). \tag{5.33}$$

$$\text{Here } G(x - x^M, \sigma_{x^M}) = \frac{1}{\sqrt{2\pi}\sigma_{x^M}} \exp\left(-\frac{(x - x^M)^2}{2\sigma^2_{x^M}}\right) \tag{5.34}$$

is the detector resolution of the VPDL and σ_{x^M} is given as

$$\sigma_{x^M} = (fg_1 \cdot SF_1 \cdot \sigma_{x^M} + (1 - fg_1) \cdot SF_2 \cdot \sigma_{x^M}) \tag{5.35}$$

where fg_1 is the number of events in the first Gaussian, SF_1 and SF_2 are the resolution scale factors for first and second Gaussians respectively as discussed in Section 5.6.4. $Eff_j(x)$ is the reconstruction efficiency for a given decay channel j of this type of B meson as a function of VPDL. The function $D_j(K)$ gives the normalized distribution of the K-factor in a given channel j. The normalization factor N_j is calculated by integration over the entire VPDL region:

$$\begin{aligned} N_j(K, \sigma_{x^M}, d_{pr}) = \int_{-\infty}^{\infty} dx^M \; Eff_j(x^M) \int_0^{\infty} dx \; G(x - x^M, \sigma_{x^M}) \\ \cdot \left(p^{osc}_{(d,u,s,\Lambda),\ j}(x, K, d_{pr}) + p^{nos}_{(d,u,s,\Lambda),\ j}(x, K, d_{pr}) \right) \end{aligned} \tag{5.36}$$

The total VPDL *pdf* for the μD_s signal is a sum of all the contributions which give the D_s mass peak:

$$\begin{aligned} P^{osc,\ nos}_{\mu D_s}(x^M, \sigma_{x^M}, d_{pr}) = \Bigg(\sum_j Br_j \cdot P^{osc,\ nos}_{d,\ j}(x^M, \sigma_{x^M}, d_{pr}) \\ + \sum_j Br_j \cdot P^{osc,\ nos}_{u,\ j}(x^M, \sigma_{x^M}, d_{pr}) \\ + \sum_j Br_j \cdot P^{osc,\ nos}_{s,\ j}(x^M, \sigma_{x^M}, d_{pr}) \\ + \sum_j Br_j \cdot P^{osc,\ nos}_{\Lambda,\ j}(x^M, \sigma_{x^M}, d_{pr}) \Bigg) \\ \cdot (1 - Fr_{c\bar{c}}) + Fr_{c\bar{c}} \cdot P^{osc,\ nos}_{c\bar{c}}(x^M) \end{aligned} \tag{5.37}$$

where,

$$P^{osc,\ nos}_{c\bar{c}}(x^M) = \frac{1}{N} \cdot \left(exp\left(-\frac{x^{M^2}}{2\sigma_1^2} \right) + exp\left(-\frac{x^{M^2}}{2\sigma_2^2} \right) \right), \tag{5.38}$$

is the *pdf* for the $c\bar{c}$ peaking background. σ_1 and σ_2 are the widths of the Gaussians fitted to the $c\bar{c}$ distribution. The sum $\sum_j$ is taken over all decay channels $B \to \mu^+\nu \mathrm{D}_\mathrm{s}^- X$ and the Br_j is the sample composition for a given channel j. In addition to the long-lived B candidates, there is a contribution of the "peaking background" which consists of combinations of D_s meson and muon originating from different c or b quarks. The direct c production gives the largest contribution to this background therefore the function $P_{c\bar{c}}^{osc,\ nos}(x^M)$ was determined from $c\bar{c}$ MC (see Fig. 5.13). We assume that this background is not sensitive to opposite-side tagging.

The branching rates Br_j were taken from the PDG [1]. The functions $D_j(K)$ were taken from the MC simulation and is in the form of histograms as an input to the fit. Uncertainties in all these inputs will contribute to the systematic uncertainties.

The B meson lifetimes and efficiencies $Eff_j(x)$ are highly correlated. The efficiencies determined using MC do not take into account the trigger selection and therefore measurements of the B meson lifetimes with such efficiencies give biased results. It is necessary to mention that the lifetime does not directly influence the measurements of the B_s oscillation frequency though error on oscillation frequency can be sensitive to the modeling of the background. Therefore, the B_s lifetime was determined from data using the efficiencies measured in MC. Deviation of the B_s lifetime from the PDG value is included into the systematic error. As a cross-check we also determine the efficiency from the data by fixing the B_s lifetime and releasing the efficiency parameters.

5.5.2 *pdf* for $\mu D^\pm$ $(D^\pm \to K^{*0}K^\pm)$ Signal

The $\mu D^\pm$ signal which forms a small peak on the left of the signal peak, See section 5.3, were also considered in the final fit. This peak is mainly due to decays from B_d

and has been modeled with the *pdf*

$$p_{B_d}^{osc/nos}(x^M, \sigma_{x^M}, d_{pr}) = \frac{Eff(x^M)}{N} \int_0^\infty dx\; G(x - x^M, s_{B_d}\sigma_{x^M}) \cdot exp\left(-\frac{Kx}{c\tau_{B_d}}\right) \cdot(1 \pm \mathcal{D}(d_{pr}) \cos(\Delta m_d \cdot Kx/c)) \quad (5.39)$$

where, τ_{B_d} is the lifetime of the B_d meson, $G(x - x^M, s_{B_d}\sigma_{x^M})$ is the detector resolution defined in equation 5.34 and $Eff(x^M)$ is the reconstruction efficiency for $B_d^0 \rightarrow \mu D^{\pm} X$ decay as a function of VPDL.

5.5.3 *pdf* for Combinatorial Background

The following contributions into the combinatorial background were considered:

1. Prompt background with the μD_s vertex coinciding with the PV (described as a Gaussian with width determined by resolution; fraction in the background: $\mathcal{F}_0$).

2. Background with quasi-vertices distributed around the PV (described as a Gaussian with constant width $\sigma_{c\bar{c}}$; fraction in the background: $\mathcal{F}_{c\bar{c}}$).

3. Long-lived background (exponential with constant decay length $c\tau_{long}$ convoluted with resolution; Fraction in the background: $\mathcal{F}_{long}$).

4. A negative exponential to take into account the outliers at negative tail. Fraction in the background: Fr_{NegExp}.

5. A positive exponential convoluted with resolution with constant decay length $c\tau_{PosExp}$ to take into account the outliers on positive tail.

The Long-lived background was further divided into three subsamples:

1. insensitive to the tagging (fraction in the long-lived background: $(1 - \mathcal{F}_{tsens})$);

2. sensitive to the tagging and non-oscillating (fraction in the background sensitive to the tagging: $(1-\mathcal{F}_{osc})$);

3. sensitive to the tagging and oscillating with frequency Δm_d (fraction in the background sensitive to the tagging: $\mathcal{F}_{osc}$).

The fractions of these contributions and their parameters were determined from the data sample. It was expected that the combinatorial background had a constant mixed/unmixed asymmetry d_{bkg}. The background *pdf* was expressed in the following form:

$$P_{bkg}(x^M,\sigma_{x^M},d_{pr}) = \mathcal{F}_{c\bar{c}}G(0-x^M,\sigma_{c\bar{c}}) + \mathcal{F}_{NegExp}\cdot\frac{-1}{c\tau_{NegExp}}exp\left(-\frac{x}{c\tau_{NegExp}}\right) \quad (5.40)$$
$$+(1-\mathcal{F}_{c\bar{c}}-\mathcal{F}_{NegExp})\cdot P^{res}_{bkg}(x^M,\sigma_{x^M}),$$

$$P^{res}_{bkg}(x^M,\sigma_{x^M},d_{pr}) = \frac{Eff(x^M)}{N}\int_0^\infty dx\,\Big(\mathcal{F}_0 G(x-x^M,s_{bkg}\sigma_{x^M})\delta(x) + \quad (5.41)$$
$$(1-\mathcal{F}_0)\cdot G(x-x^M,\sigma_{x^M})\left(\mathcal{F}_{long}\cdot p^{long}_{bkg} + (1-\mathcal{F}_{long})\cdot\frac{1}{c\tau_{long}}exp\left(-\frac{x}{c\tau_{long}}\right)\right),$$

$$p^{long,osc/nos}_{bkg}(x,d_{pr}) = \frac{1}{c\tau_{bkg}}\exp\left(-\frac{x}{c\tau_{bkg}}\right)((1-\mathcal{F}_{tsens}) + \mathcal{F}_{tsens}\,((1\pm\mathcal{D})(1-\mathcal{F}_{osc}) \quad (5.42)$$
$$+(1\pm\mathcal{D}\cos(\Delta m_d\cdot x/c))\cdot\mathcal{F}_{osc},$$

where N is the normalization constant and the fit parameters are $\mathcal{F}_{c\bar{c}}$, $\sigma_{c\bar{c}}$, $\mathcal{F}_0$, $\mathcal{F}_{tsens}$, $\mathcal{F}_{long}$, $\mathcal{F}_{NegExp}$, $\mathcal{F}_{osc}$, $c\tau_{Neg}$, $c\tau_{long}$ and $c\tau_{bkg}$. As an efficiency $Eff(x^M)$, the efficiency for the $B^0_d \to D^-\mu^+\nu X$ channel was used.

5.6 Inputs to the Fit

5.6.1 Sample Composition

To determine the composition of the selected μD_s sample, the following decay channels of B mesons were considered :

- $\mathrm{B_s^0} \to \mu^+ \nu \mathrm{D_s^-}$;
- $\mathrm{B_s^0} \to \mu^+ \nu \mathrm{D_s^{-*}} \to \mu^+ \nu \mathrm{D_s^-}$;
- $\mathrm{B_s^0} \to \mu^+ \nu D_{s0}^{*-} \to \mu^+ \nu \mathrm{D_s^-}$;
- $\mathrm{B_s^0} \to \mu^+ \nu D_{s1}^{'-} \to \mu^+ \nu \mathrm{D_s^-}$;
- $\mathrm{B_s^0} \to \tau^+ \nu \mathrm{D_s^-} X, \tau \to \mu \nu X$;
- $\mathrm{B_s^0} \to \mathrm{D_s^+ D_s^-} X; \mathrm{D_s^-} \to \mu \nu X$;
- $\mathrm{B_s^0} \to D_s D X; D \to \mu \nu X$;
- $B^+ \to D \mathrm{D_s^-} X; D \to \mu \nu X$;
- $B^0 \to D \mathrm{D_s^-} X; D \to \mu \nu X$;

The latest PDG values[1] were used to determine the branching fractions of decays contributing to the $\mathrm{D_s^-}$ sample. EvtGen [59] inputs were used for the branching fractions which are not given in PDG.

- $\mathrm{Br}(\mathrm{B_s^0} \to \mu^+ \nu \mathrm{D_s^-} X) = (7.9 \pm 2.4)\%$, total semileptonic Br was taken from PDG, fractions of exclusive channels were taken from EvtGen;
  - $\mathrm{Br}(\mathrm{B_s^0} \to \mu^+ \nu \mathrm{D_s^-}) = 2.0\%$;
  - $\mathrm{Br}(\mathrm{B_s^0} \to \mu^+ \nu \mathrm{D_s^{-*}}) = 5.3\%$;
  - $\mathrm{Br}(\mathrm{B_s^0} \to \mu^+ \nu D_{s0}^{*-}) = 0.19\%$;

- $\mathrm{Br}(\mathrm{B_s^0} \to \mu^+ \nu D_{s1}^{'-}) = 0.35\%$;

- $\mathrm{Br}(\mathrm{B_s^0} \to \tau^+ \nu \mathrm{D_s^-} X) = 2.9\%$, from Evtgen;
- $\mathrm{Br}(\tau^+ \to \mu\nu\nu) = (17.36 \pm 0.06)\%$, from PDG;
- $\mathrm{Br}(\mathrm{B_s^0} \to \mathrm{D_s^+ D_s^-} X) = 23^{+21}_{-13}\%$, from PDG;
- $\mathrm{Br}(\mathrm{B_s^0} \to D\mathrm{D_s^-} X) = 15.4\%$, from EvtGen;
- $\mathrm{Br}(B^+ \to D\mathrm{D_s^-} X) = 10.5 \pm 2.6\%$, from PDG;
- $\mathrm{Br}(B^0 \to D\mathrm{D_s^-} X) = 10.5 \pm 2.6\%$, from PDG;
- $\mathrm{Br}(\mathrm{D_s^{-*}} \to \mathrm{D_s^-} X) = 100\%$;
- $\mathrm{Br}(D_{s0}^{*-} \to \mathrm{D_s^-} X) = 100\%$;
- $\mathrm{Br}(D_{s1}^{'-} \to \mathrm{D_s^-} X) = 100\%$;
- $\mathrm{Br}(\mathrm{D_s^-} \to \mu\nu X) = (6.3 \pm 0.8)\%$, from PDG, assuming the same partial width as for D^0 and D^+;
- $\mathrm{Br}(D^0 \to \mu\nu X) = (6.5 \pm 0.8)\%$, from PDG;
- $\mathrm{Br}(D^+ \to \mu\nu X) = (17.2 \pm 1.9)\%$, from PDG;
- $\mathrm{Br}(\bar{b} \to B^0) = 39.7 \pm 1.0\%$, from PDG;
- $\mathrm{Br}(\bar{b} \to B^+) = 39.7 \pm 1.0\%$, from PDG;
- $\mathrm{Br}(\bar{b} \to \mathrm{B_s^0}) = 10.7 \pm 1.1\%$, from PDG;

To determine the uncertainties, we varied the branching fractions used as inputs by their corresponding uncertainties one by one and used the maximum deviation as an estimate of the sample composition uncertainty. The MC statistical uncertainty

Table 5.3: Sample composition.

Process	pt muon > 2 GeV	pt muon > 6 GeV
$B_s^0 \to \mu^+\nu D_s^-$	$(19.35 \pm 1.37)\%$	19.64%
$B_s^0 \to \mu^+\nu D_s^{-*} \to \mu^+\nu D_s^- X$	$(59.00 \pm 4.19)\%$	63.57%
$B_s^0 \to \mu^+\nu D_{s0}^{*-} \to \mu^+\nu D_s^- X$	$(1.97 \pm 0.14)\%$	1.87%
$B_s^0 \to \mu^+\nu D_{s1}^{'-} \to \mu^+\nu D_s^- X$	$(2.16 \pm 0.36)\%$	2.00%
$B_s^0 \to \tau^+\nu D_s^- \to \mu^+\nu D_s^- X$	$(2.01 \pm 0.41)\%$	1.75%
$B_s^0 \to D_s^+ D_s^- X; D_s^- \to \mu\nu X$	$(2.04^{+1.07}_{-2.54})\%$	0.76%
$B_s^0 \to D D_s^- X; D \to \mu\nu X$	$(0.90 \pm 0.3)\%$	0.697%
$B^+ \to D D_s^- X; D \to \mu\nu X$	$(6.03 \pm 2.02)\%$	4.79%
$B^0 \to D D_s^- X; D \to \mu\nu X$	$(6.48 \pm 2.18)\%$	4.88%

was not taken into account. For the DD branching fractions estimated from the EvtGen generator, we used 25% relative uncertainty.

The relative fractions of the signal $B_s^0 \to \mu^+\nu D_s^- X$ were not varied for the sample composition since this contribution to the systematic error is taken into account by the variation of the corresponding K factors. The $B_s^0 \to D D_s^- X; D \to \mu\nu X$ branching fraction was varied from its PDG value (23%) to its EvtGen value (4.5%). For most of the contributions, the maximum deviation occurs when the signal Br is varied within its uncertainty $(7.9 \pm 2.4)\%$. The reconstruction efficiency did not include any lifetime cuts at this point.

To determine how sensitive the sample composition was to the muon p_T cut we increased the cut from 2 GeV/c to 6 GeV/c and recalculated the sample composition, see table 5.3. The total contribution of the signal (sum of the first four channels) increased from 82.54% to 87.10%. This was expected as the muon p_T spectra of the processes where the muon originates from a secondary decay are softer and therefore take an additional hit after the harder p_T cut.

5.6.2 K Factor

Semileptonic B decays necessarily have an undetected neutrino present in the decay chain, making a precise determination of the B meson kinematics impossible. In

addition, other neutral or non-reconstructed charged particles can be present in the decay chain of the B meson. This leads to a bias towards smaller values of the momentum of the B meson calculated using reconstructed particles only. A common practice to correct this bias is to scale the measured momentum of the B meson by a K factor, which takes into account the effect of the neutrino and other lost (or unreconstructed) particles. The K factor was estimated from the MC simulation. For this analysis, it was defined as

$$K = p_T(\mu \mathrm{D_s^-})/p_T(B), \tag{5.43}$$

where p_T denotes the absolute value of the transverse momentum.

For the computation of p_T, the generator level information was used. We also checked that using the reconstructed values for p_T did not cause any bias. Following the definition (5.43), the K factors for $\mathrm{B_s^0} \to \mu^+\nu\mathrm{D_s^-}$ and $\mathrm{B_s^0} \to \mu^+\nu D_s^{*-} \to \mu^+\nu\mathrm{D_s^-}$ decays were calculated after the lifetime cuts. Addition of the lifetime cuts does not bias the K factors.

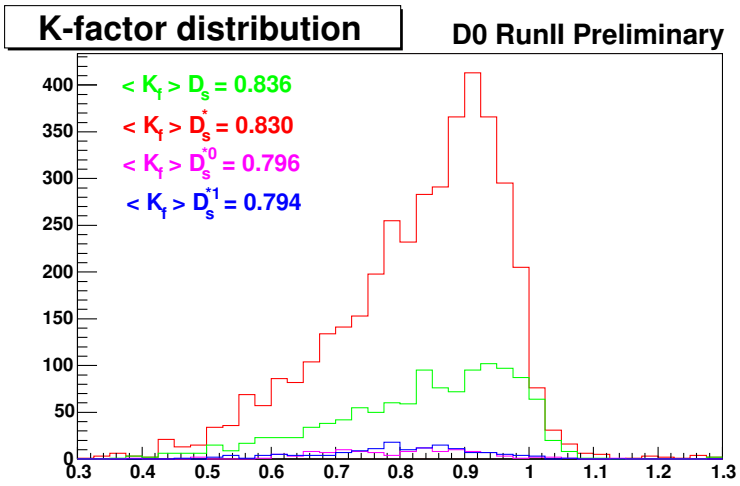

Figure 5.14: K factors for $\mathrm{B_s^0} \to \mu^+\nu\mathrm{D_s^-}$ and $\mathrm{B_s^0} \to \mu^+\nu D_s^{*-} \to \mu^+\nu\mathrm{D_s^-}$ processes.

Figure 5.14 shows the distributions of the K factors for the semileptonic decays $\mathrm{B_s^0} \to \mu^+\nu\mathrm{D_s^-}$ and $\mathrm{B_s^0} \to \mu^+\nu D_s^{*-} \to \mu^+\nu\mathrm{D_s^-}$. As expected, the K factor for D_s^{*-}

decays had a lower mean value because more decay products are missing. Note that since the K factors in (5.43) were defined as the ratio of transverse momenta, they can exceed 1.

The K factor distributions are divided into four mass($D_s^-\mu$) bins for the likelihood fit. The mass bins are: mass($D_s^-\mu$) < 3.5 GeV/c^2, $3.5 <$ mass($D_s^-\mu$) < 4.0 GeV/c^2, $4.0 <$ mass($D_s^-\mu$) < 4.5 GeV/c^2, and mass($D_s^-\mu$) > 4.5 GeV/c^2. The K factor distributions for the four mass($D_s^-\mu$) bins for $B_s^0 \to \mu^+\nu D_s^-$ decays are shown in Fig. 5.15. Figure 5.16 shows the distributions for $B_s^0 \to \mu^+\nu D_s^{*-} \to \mu^+\nu D_s^-$ decays.

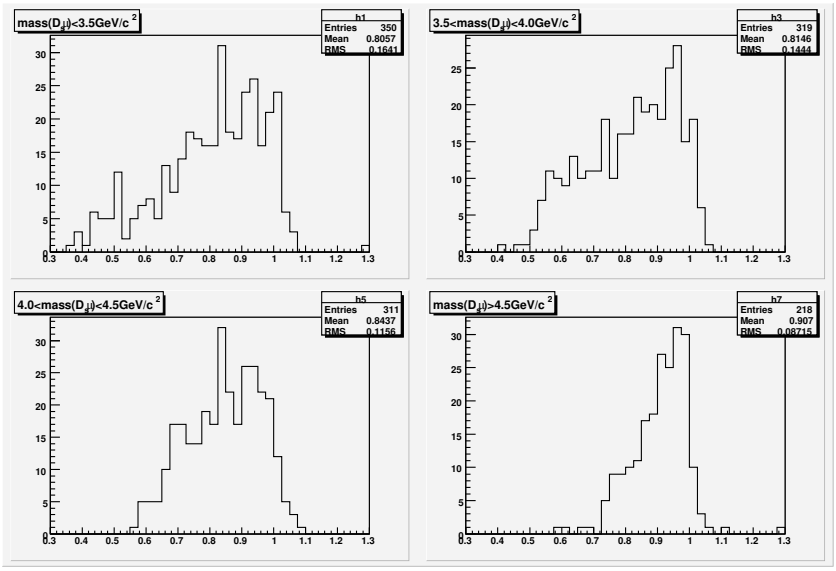

Figure 5.15: K factor versus mass($D_s^-\mu$) for $B_s^0 \to \mu^+\nu D_s^-$ decays.

These K factor distributions were used in the equation 5.33 in the form of histograms.

5.6.3 Reconstruction Efficiencies

The reconstruction efficiency of different modes contributing to the B_s was determined using the MC simulations. The efficiency strongly depends on the decay length due to the lifetime biased selections for the sample. We determined the efficiency as a

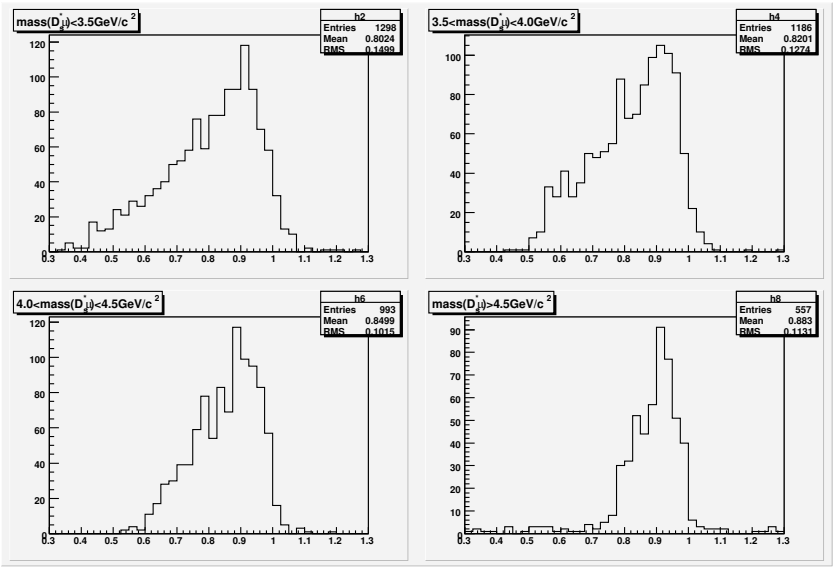

Figure 5.16: K factor versus mass($\mathrm{D_s^-}\mu$) for $\mathrm{B_s^0} \to \mu^+\nu D_s^{*-} \to \mu^+\nu \mathrm{D_s^-}$ decays.

function of the reconstructed VPDL. The fit function is

$$Eff(x^M) = p_0 \cdot (1 - (p_2 + p_3 \cdot x^M + p_4 \cdot (x^M)^2 + p_5 \cdot (x^M)^3) \cdot exp(-(x^M)^2/p_1)); \quad (5.44)$$

This function was selected because it allows analytical calculation of the normalization integral (see Eq. 5.37).

Figure 5.17 shows the efficiency as function of VPDL for the decay $B_s \to \mu^+\nu \mathrm{D_s^-} X$. All semileptonic modes were considered together.

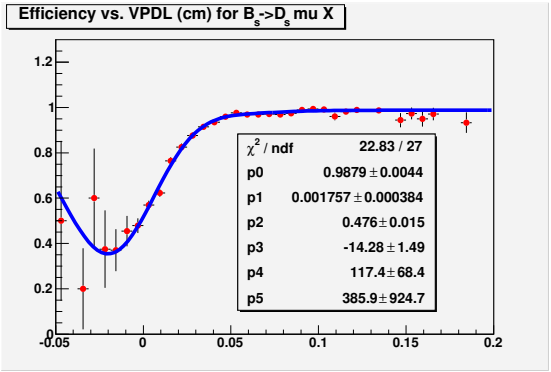

Figure 5.17: Efficiency as function of VPDL for $B_s \to \mu^+\nu \mathrm{D_s^-} X$.

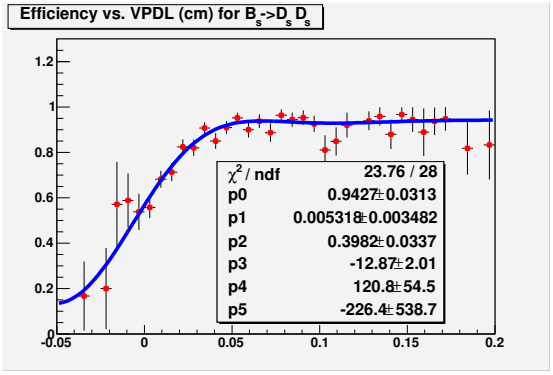

Figure 5.18: Efficiency as function of VPDL for $B_s \to D_s^+ \mathrm{D_s^-} X$.

Figure 5.18 shows the efficiency as function of VPDL for the decay $B_s \to D_s^+ \mathrm{D}_\mathrm{s}^- X, \mathrm{D}_\mathrm{s}^- \to \mu\nu X$.

Figure 5.19 shows the efficiency as function of VPDL for the decay $B_s \to D\mathrm{D}_\mathrm{s}^- X; D \to \mu\nu X$.

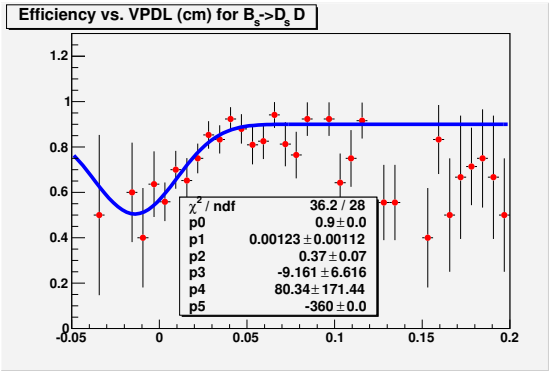

Figure 5.19: Efficiency as function of VPDL for $B_s \to D\mathrm{D}_\mathrm{s}^- X; D \to \mu\nu X$.

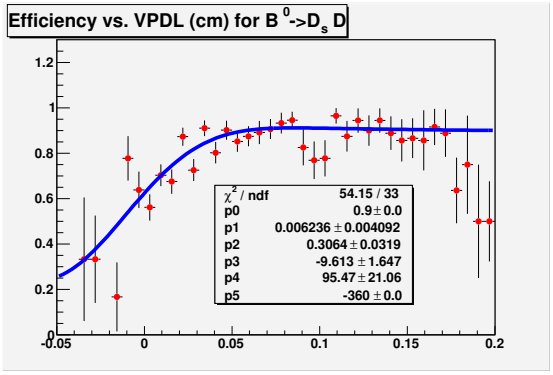

Figure 5.20: Efficiency as function of VPDL for $B^0 \to D\mathrm{D}_\mathrm{s}^- X; D \to \mu\nu X$.

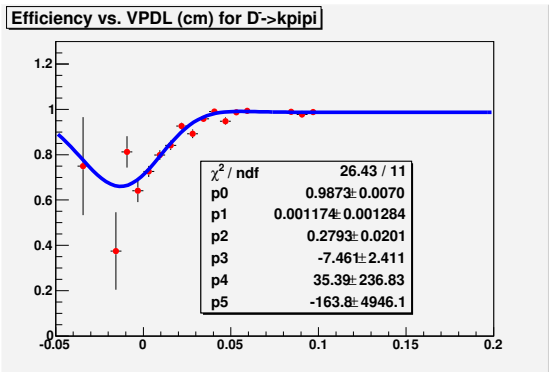

Figure 5.21: Efficiency as function of VPDL for $D^+ \to K^+\pi^-\pi^+$.

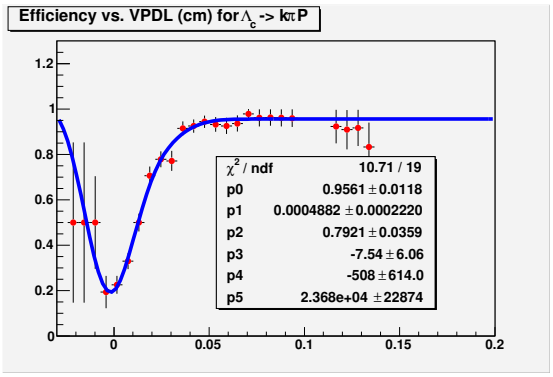

Figure 5.22: Efficiency as function of VPDL for $\Lambda_c^+ \to K^+\pi^- p^+$.

Figure 5.20 shows the efficiency as function of VPDL for the decay $B^0 \to D\mathrm{D}_\mathrm{s}^- X; D \to \mu\nu X$.

Figure 5.21 shows the efficiency as function of VPDL for the decay $D^+ \to K^+\pi^-\pi^+$.

Figure 5.22 shows the efficiency as function of VPDL for the decay $\Lambda_c^+ \to K^+\pi^- p^+$.

Figure 5.23 shows the efficiency as function of VPDL for the decay $B^- \to D\mathrm{D}_\mathrm{s}^- X; D \to \mu\nu X$.

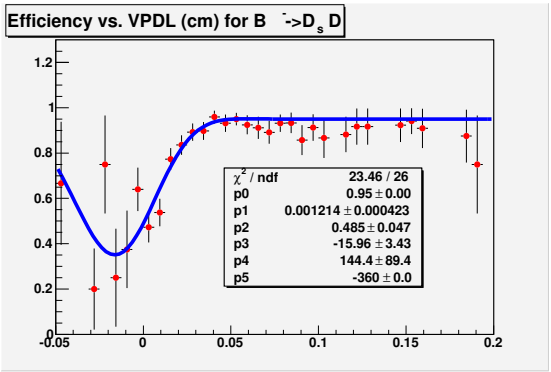

Figure 5.23: Efficiency as function of VPDL for $B^- \to D\mathrm{D}_s^- X; D \to \mu\nu X$.

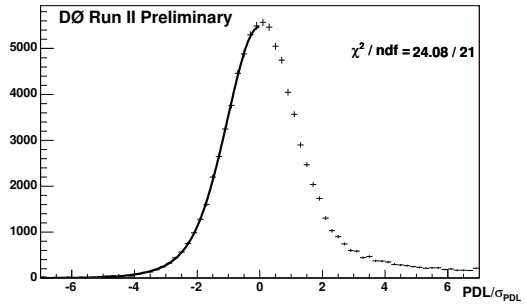

Figure 5.24: Pull of J/ψ vertex distribution with respect to the Primary Vertex.

5.6.4 Resolution Scale Factor

The VPDL error was estimated by the vertex fitting procedure. A resolution scale factor SF was introduced to take into account a possible bias. The SF was determined using the J/ψ sample (see Fig. 5.24). The negative tail of the pull of J/ψ vertex distribution with respect to the PV should be a Gaussian with a sigma of 1 if errors assigned to the vertex coordinates were correct. For this J/ψ decay muons from the PV were excluded . The positive side of the pull distribution was ignored as that tends to be biased towards the larger value due to J/ψ mesons from the real B meson decays. It is known that the scale factor depends on track transverse momenta, therefore, the scale factor was also determined for J/ψ candidates with the leading muon $p_{t_{\mu_1}} > 6$ GeV/c to estimate the contribution to the systematic error. The corresponding scale factor increased by 2.5%.

The resulting pull distribution was fitted with a double Gaussian. The fit returns a narrow Gaussian with width $\sigma_{narrow} = 0.998$ comprising 72% of the events, and a wide Gaussian with $\sigma_{wide} = 1.775$ comprising the rest of the events (28%).

5.7 Results of the Lifetime Fit

The total tagged data sample was used to determine the parameters: $\mathcal{F}_{c\bar{c}} = 0.023 \pm 0.003$, $\sigma_{c\bar{c}} = 120 \pm 9$ μm, $\mathcal{F}_0 = 0.067 \pm 0.002$, $c\tau_{long} = 549 \pm 10$ μm, $\mathcal{F}_{long} = 0.91 \pm 0.013$, $\mathcal{F}_{NegExp} = 0.062 \pm 0.002$, $\mathcal{F}_{tsens} = 0.51 \pm 0.085$, $\mathcal{F}_{osc} = 0.66 \pm 0.096$, $c\tau_{PosExp} = 662 \pm 9$ μm, $c\tau_{NegExp} = -53 \pm 2$ μm, $c\tau_{B_s} = 407 \pm 22$ μm and scale factor of 1.91 ± 0.034. Figure 5.25 and 5.26 show distributions of events on VPDL with optimal fit parameters in the fitting function. Only VPDL *pdf*s were used to plot the projection of the fit. In the sideband data, only VPDL *pdf* was used to perform the fit, therefore fit projection for sidebands looks better. This reflects the fact that we understand our background. For signal, not all the *pdf*s were used to visualize the fit projection so fit plot may not look perfect and other *pdf*s needed to be taken into account for the perfect plot.

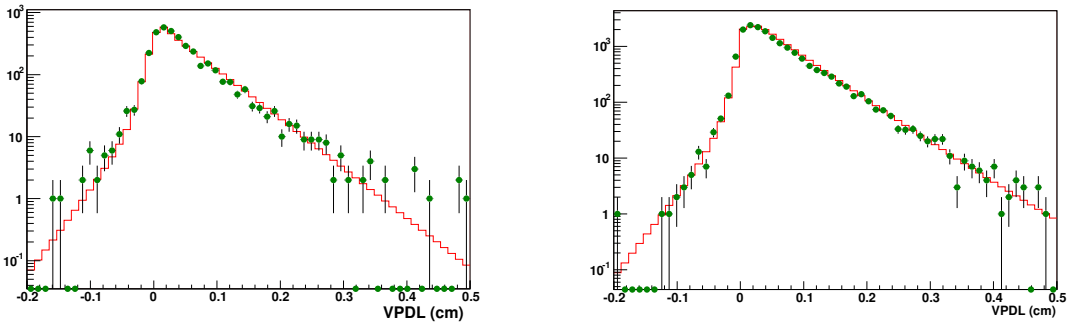

Figure 5.25: Distribution of events on VPDL in right band region ($2.15 < M_{D_s} < 2.25$ GeV)(left plot) and signal peak region ($1.91 < M_{D_s} < 2.03$ GeV)(right plot) on log scale. Points represent experimental data and histogram — fitting function.

5.8 Fitting Procedure for Δm_s Limit

Amplitude fit method [20] was used to scan for the Δm_s and to set the limit on the B_s^0 oscillations.

For a given type of B hadron (i.e. d, u, s), the distribution of the VPDL is given

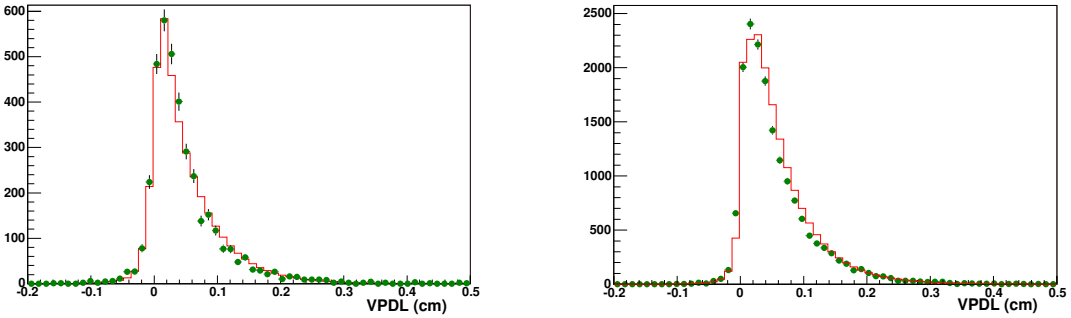

Figure 5.26: Distribution of events on VPDL in right band region ($2.15 < M_{D_s} < 2.25$ GeV)(left plot) and signal peak region ($1.91 < M_{D_s} < 2.03$ GeV) (right plot) on linear scale.Points represent experimental data and histogram — fitting function.

by:

$$p_s^{nos}(x) = \frac{K}{c\tau_{B_s}} \exp(-\frac{Kx}{c\tau_{B_s}}) \cdot 0.5 \cdot (1 + \mathcal{A} \cdot \mathcal{D} \cos(\Delta m_s \cdot Kx/c)) \tag{5.45}$$

$$p_s^{osc}(x) = \frac{K}{c\tau_{B_s}} \exp(-\frac{Kx}{c\tau_{B_s}}) \cdot 0.5 \cdot (1 - \mathcal{A} \cdot \mathcal{D} \cos(\Delta m_s \cdot Kx/c)) \tag{5.46}$$

where τ is the lifetime of B hadron, K is the K factor and $\mathcal{A}$ is a fit parameter. Different choices of Δm_s are used as input and the fitted value of $\mathcal{A}$ is returned. By plotting the fitted value of $\mathcal{A}$ as a function of the input value of Δm_s, one searches for a peak of $\mathcal{A}$=1 to obtain a measurement of Δm_s. For any value of Δm_s not equal to the "true" value of B_s oscillation frequency, the amplitude $\mathcal{A}$ should be zero. If no peak is found, limits can easily be set on Δm_s using this method. The sensitivity of a measurement is determined by calculating the probability that at a non-"true"value of Δm_s, the amplitude could fluctuate to $\mathcal{A}$=1. This occurs at the lowest value of Δm_s for which $1.645\ \sigma_{\Delta m_s} = 1$ for a 95% CL, where $\sigma_{\Delta m_s}$ is the uncertainty on the value of $\mathcal{A}$ at the point Δm_s. The limit is determined by calculating the probability that a fitted value of $\mathcal{A}$ could fluctuate to $\mathcal{A} = 1$. This occurs at the lowest value of Δm_s for which $\mathcal{A}_{dms} + 1.645\sigma_{dms} = 1$.

5.9 Results

Figure 5.27 shows the dependence of the parameter $\mathcal{A}$ and its error on the Δm_s. A 95% confidence level limit on the oscillation frequency $\Delta m_s > 9.3\ ps^{-1}$ and sensitivity 11.7 ps^{-1} were obtained.

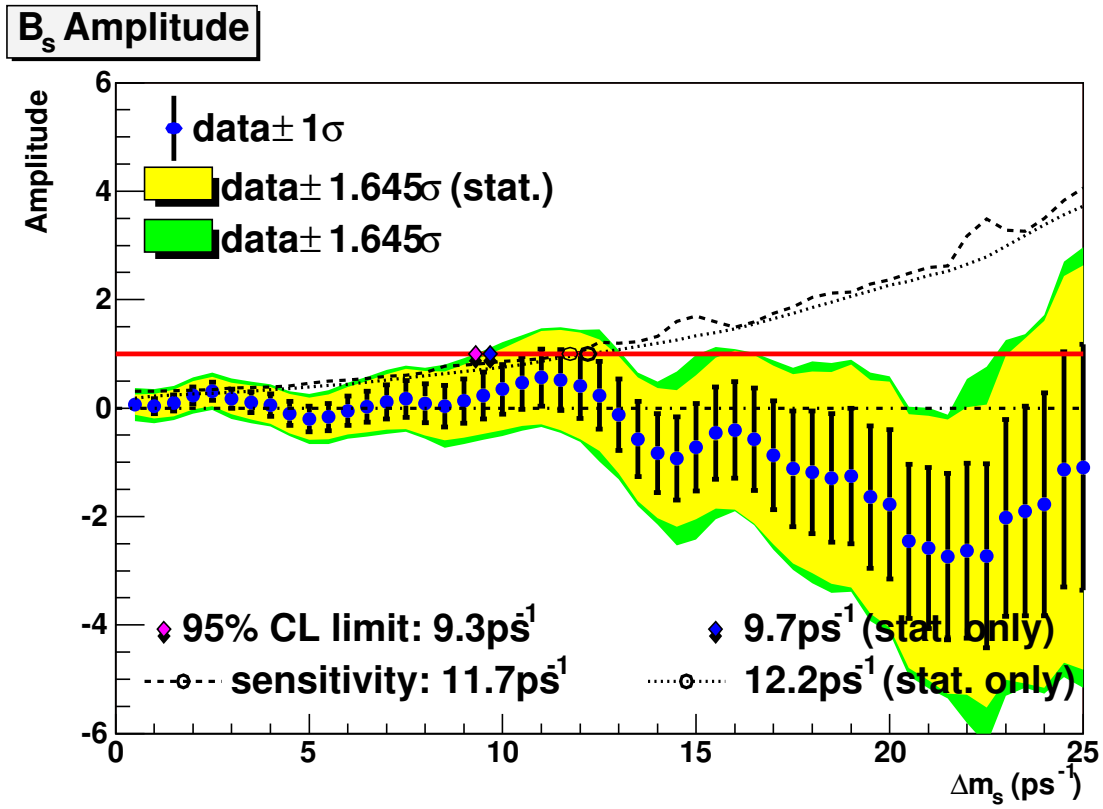

Figure 5.27: B_s^0 oscillation amplitude with statistical and systematic errors.

5.10 Cross Checks and Systematics

We expect the following to contribute to the systematic uncertainty of the limit:

- Dilution
- Mass fitting procedure
- Resolution

- Sample composition
- K factor
- Efficiency

The contribution to the systematic error from the uncertainties of the input fit parameters can be estimated using the formula [20]:

$$\sigma_{\mathcal{A}}^{sys} = \Delta\mathcal{A} + (1 - \mathcal{A})\frac{\Delta\sigma_{\mathcal{A}}}{\sigma_{\mathcal{A}}} \tag{5.47}$$

5.10.1 Dilution

A test of the flavor tagger performance was done using $\mu D^{\pm}$ events from the reflection peak in the $(K\pi)K$ mass spectrum (see Fig. 5.8) which originates mainly from the decays $B_d \to X\mu D^{\pm}$. Using these events a scan was performed for ΔM_d as a cross check. This scan is more sensitive to the description of the combinatorial background and, therefore, the original description has been changed to take into account oscillations in the B_d contribution. The resulting amplitude scan is shown in Figures 5.28 and 5.29. The amplitude at $\Delta M_d = 0.5$ ps^{-1} is in agreement with 1, which confirms that the dilution calibration was performed correctly. This cross-check also shows the ability of the method to detect an oscillation signal.

5.10.2 Mass fitting procedure

As a cross check for mass fitting procedure we fit the $M(K\pi)K$ distribution for $M(K\pi) > 1$ GeV. It is expected that for this cut all the $D_s^- \to K^{*0}K^-$ signal would be rejected and what is left would all be $D^+ \to K\pi\pi$ reflection. We apply the fitting technique to this distribution and the fit returns almost zero $D_s^- \to K^{*0}K^-$ signal candidates and rest everything is coming from $D^{\pm}$ reflection in the peak, fit is shown in Fig. 5.30.

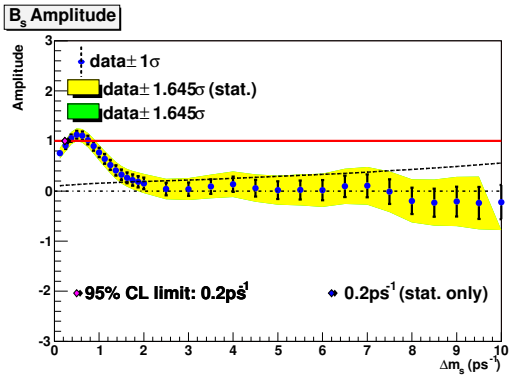

Figure 5.28: $B_d - \bar{B}_d$ oscillation amplitude.

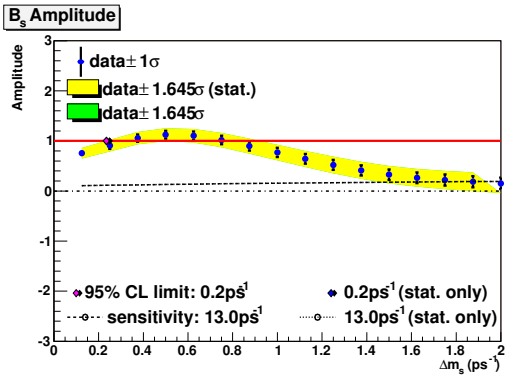

Figure 5.29: $B_d - \bar{B}_d$ oscillation amplitude (detailed view of the B_d oscillation region).

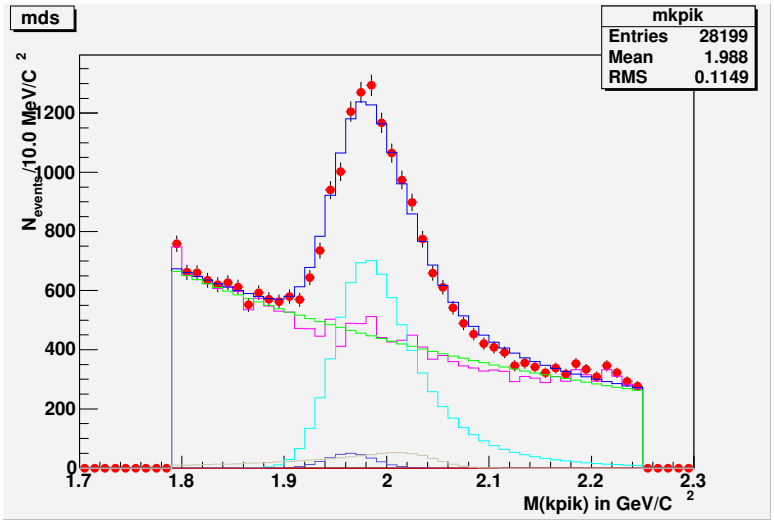

Figure 5.30: Fit to the $M(K\pi)K$ distribution for $M(K\pi) > 1\ GeV$. Tiny blue histogram at the bottom is the $D_s^- \to K^{*0}K^-$ signal, light blue is the $D^\pm$ reflection, golden color is the $\Lambda_c^\pm$ reflection and green curve is the fit to the combinatoric background.

Since this channel is dominated by the reflection from the $D^\pm$ decays so in order to take the effect due to modeling of the mass fitting procedure we increased the fraction of the $D^\pm$ reflection by 1σ and fixed it. We then re-did the entire mass fitting procedure for the tagged sample and obtained the fractions of the signal, Cabbibo $D^\pm$ and Λ_c reflection fractions. We used these new fractions to estimate the systematic error due to mass fitting procedure. Also, the masses of the $D^\pm$ and D_s were varied by one σ and found to be within the uncertainty on the fractions obtained from the

above stated procedure hence a separate systematics were not estimated for this.

5.10.3 Resolution

We use $SF = 1.205$ to estimate systematic errors. This value of the scale factor was motivated by the scale factor obtained by applying a 6 GeV cut on the P_T of the muon to account for the trigger efficiencies as described in section 5.6.4. After this cut, though the scale factor increases only by about 2.5% but to be conservative we vary the scale factor by 3.5%.

5.10.4 Sample Composition

The $B_s \to D_s D_s$ branching ratio was changed from 10% to 4.7% (EvtGen value) and 23% (PDG value). The branching ratio $B_s \to D_s \mu X$ was also changed from 7.9% to 5.5% (PDG uncertainty). The variation of the branching ratio $B_s \to D_s \mu X$ gives the largest change in the signal fraction. Other systematics for sample composition is listed in the systematics table 5.4.

The sample composition was also determined with the muon p_T cut 6 GeV/c (see Section 5.6.1). The corresponding contribution to the systematic error was determined and assigned to the MC efficiency uncertainty.

5.10.5 K factor

Four additional sets of K-factor distributions were generated to estimate contributions to the systematic error.

In one set, the K factor defined in Eqn. 5.43 was scaled up by 2% (i.e., multiplied by 1.02). In the second set of K-factor distributions, the K factor was scaled down by 2% (i.e., multiplied by 0.98). In the third set, the distributions were smoothed using the ROOT function "Smooth" (with argument 1, which applies the smoothing

algorithm once). The final set of histograms was generated using the definition

$$K = p_T^{reco}(\mu \mathrm{D_s^-})/p_T^{MC}(B). \tag{5.48}$$

The resulting systematic errors were obtained using the formula (5.47) and summed in quadrature. The result is shown on the Figure 5.27.

5.11 Conclusions

Using a signal of 12.6k $\mathrm{B_s^0} \to \mu^+ \nu \mathrm{D_s^-} X$ decays where $D_s^- \to K^{*0} K^-$, $K^{*0} \to K^+ \pi^-$ and an opposite side flavor tagging algorithm we performed a search for $\mathrm{B_s^0} - \bar{\mathrm{B}}_\mathrm{s}^0$ oscillations. We obtained a 95% confidence level limit on the oscillation frequency $\Delta \mathrm{m_s} > 9.3$ ps^{-1} and a sensitivity of 11.7 ps^{-1}.

Table 5.4: Systematic uncertainties on the amplitude. The shifts of both the measured amplitude, $\Delta\mathcal{A}$, and its statistical uncertainty, $\Delta\sigma$, are listed

Osc. frequency		1 ps^{-1}	2 ps^{-1}	3 ps^{-1}	4 ps^{-1}	5 ps^{-1}	6 ps^{-1}	7 ps^{-1}	8 ps^{-1}	9 ps^{-1}	10 ps^{-1}	11 ps^{-1}	12 ps^{-1}	13 ps^{-1}
$\mathcal{A}$		0.035	0.235	0.174	0.053	−0.199	−0.049	0.115	0.089	0.129	0.346	0.563	0.409	−0.120
Stat. uncertainty		0.137	0.158	0.176	0.207	0.236	0.268	0.313	0.362	0.411	0.456	0.525	0.595	0.658
$PDG\ c\tau_{B_s}$	$\Delta\mathcal{A}$	−0.020	−0.006	−0.004	+0.002	−0.011	+0.003	+0.011	+0.003	+0.007	+0.012	+0.027	+0.021	+0.002
	$\Delta\sigma$	+0.001	+0.002	+0.002	+0.004	+0.005	+0.006	+0.008	+0.009	+0.011	+0.013	+0.016	+0.019	+0.021
Signal SF variation	$\Delta\mathcal{A}$	+0.002	+0.003	+0.001	+0.002	−0.003	−0.001	+0.005	+0.009	+0.017	+0.031	+0.036	+0.030	+0.015
by 3.5%	$\Delta\sigma$	+0.000	+0.001	+0.001	+0.002	+0.003	+0.005	+0.006	+0.008	+0.010	+0.012	+0.015	+0.018	+0.022
D^+_{Refl} fraction	$\Delta\mathcal{A}$	−0.011	+0.006	+0.007	+0.001	−0.006	−0.006	+0.000	+0.005	+0.004	+0.008	+0.017	+0.016	+0.003
+ 1σ	$\Delta\sigma$	+0.002	+0.002	+0.003	+0.003	+0.004	+0.004	+0.005	+0.005	+0.006	+0.006	+0.008	+0.009	+0.010
D^+_{Refl} fraction	$\Delta\mathcal{A}$	+0.037	−0.020	−0.023	−0.007	+0.015	+0.010	−0.009	−0.019	−0.017	−0.028	−0.052	−0.046	−0.012
- 1σ	$\Delta\sigma$	−0.007	−0.008	−0.009	−0.010	−0.012	−0.013	−0.015	−0.018	−0.020	−0.022	−0.025	−0.030	−0.032
D_s signal	$\Delta\mathcal{A}$	−0.018	+0.011	+0.011	+0.005	−0.003	+0.003	+0.013	+0.014	+0.010	+0.013	+0.020	+0.021	+0.009
- 1σ	$\Delta\sigma$	+0.004	+0.004	+0.004	+0.005	+0.006	+0.007	+0.008	+0.010	+0.011	+0.012	+0.015	+0.017	+0.019
Signal $c\bar{c}$ fraction changed	$\Delta\mathcal{A}$	+0.024	+0.039	+0.032	+0.026	+0.008	+0.015	+0.029	+0.028	+0.029	+0.043	+0.064	+0.055	+0.002
to 6%	$\Delta\sigma$	+0.004	+0.004	+0.005	+0.006	+0.008	+0.009	+0.012	+0.015	+0.018	+0.021	+0.027	+0.033	+0.037
$Br(D_sD_s) = 4.7\%$	$\Delta\mathcal{A}$	+0.001	−0.003	−0.002	−0.001	+0.002	+0.000	−0.002	−0.001	−0.002	−0.004	−0.006	−0.005	+0.001
	$\Delta\sigma$	−0.001	−0.002	−0.002	−0.002	−0.002	−0.003	−0.003	−0.004	−0.004	−0.005	−0.006	−0.006	−0.007
K-factor decreased	$\Delta\mathcal{A}$	+0.003	−0.012	+0.017	+0.021	+0.010	−0.027	−0.032	+0.034	−0.045	−0.028	−0.043	+0.037	+0.176
by 2%	$\Delta\sigma$	−0.001	−0.000	−0.001	−0.002	−0.003	−0.003	−0.006	−0.007	−0.008	−0.008	−0.017	−0.014	−0.015
Br(μD_s) = 5.5%	$\Delta\mathcal{A}$	+0.022	+0.005	+0.004	−0.009	−0.021	−0.015	−0.005	−0.006	+0.001	+0.013	+0.026	+0.025	−0.005
	$\Delta\sigma$	+0.008	+0.009	+0.011	+0.012	+0.014	+0.016	+0.019	+0.022	+0.026	+0.028	+0.032	+0.037	+0.041
Oscillated and Mixed fraction	$\Delta\mathcal{A}$	+0.033	−0.000	−0.009	−0.012	−0.012	−0.011	−0.011	−0.012	−0.010	−0.009	−0.008	−0.006	−0.008
varied in bkg	$\Delta\sigma$	+0.000	+0.000	+0.000	+0.000	+0.000	+0.000	+0.000	+0.000	+0.000	+0.000	+0.000	+0.000	+0.000
Br(μDs) = 10.8%	$\Delta\mathcal{A}$	−0.011	−0.003	−0.003	+0.004	+0.011	+0.008	+0.002	+0.003	−0.001	−0.008	−0.015	−0.015	+0.003
	$\Delta\sigma$	−0.005	−0.005	−0.006	−0.007	−0.008	−0.009	−0.011	−0.013	−0.014	−0.016	−0.018	−0.021	−0.023
$Br(D_sD_s) = 23\%$	$\Delta\mathcal{A}$	−0.002	+0.007	+0.006	+0.003	−0.004	−0.001	+0.004	+0.003	+0.004	+0.010	+0.016	+0.012	−0.003
	$\Delta\sigma$	+0.004	+0.004	+0.005	+0.005	+0.006	+0.007	+0.008	+0.009	+0.011	+0.012	+0.014	+0.016	+0.017
K-factor increased	$\Delta\mathcal{A}$	+0.011	+0.011	+0.018	−0.042	+0.012	+0.023	+0.019	−0.052	+0.088	+0.149	−0.006	−0.158	−0.310
by 2%	$\Delta\sigma$	+0.002	+0.004	+0.008	+0.012	+0.017	+0.021	+0.028	+0.034	+0.039	+0.048	+0.055	+0.057	+0.067
Bkg SF changed	$\Delta\mathcal{A}$	+0.001	+0.001	−0.000	−0.001	−0.001	−0.002	−0.003	−0.003	−0.004	−0.004	−0.004	−0.005	−0.004
to 2.0	$\Delta\sigma$	−0.000	−0.000	−0.000	−0.000	−0.000	−0.000	−0.000	−0.000	−0.000	−0.000	−0.000	−0.000	−0.000
Bkg $c\bar{c}$ changed	$\Delta\mathcal{A}$	+0.018	+0.009	+0.007	+0.004	−0.001	−0.005	−0.011	−0.014	−0.011	−0.001	+0.009	+0.001	−0.018
to 10.23%	$\Delta\sigma$	−0.000	−0.000	−0.001	−0.001	−0.000	−0.000	+0.000	+0.001	+0.002	+0.002	+0.003	+0.005	+0.005
$P_T(\mu)$	$\Delta\mathcal{A}$	−0.014	−0.005	−0.005	+0.005	+0.014	+0.009	+0.001	+0.004	−0.002	−0.012	−0.021	−0.019	+0.007
> 6 GeV	$\Delta\sigma$	−0.006	−0.007	−0.008	−0.009	−0.011	−0.012	−0.014	−0.017	−0.019	−0.022	−0.025	−0.028	−0.031
Generator level	$\Delta\mathcal{A}$	+0.004	+0.011	+0.014	−0.019	−0.006	−0.002	+0.001	+0.023	+0.030	−0.018	−0.013	−0.010	+0.014
K factor	$\Delta\sigma$	+0.001	+0.002	+0.003	+0.005	+0.006	+0.009	+0.011	+0.014	+0.017	+0.020	+0.023	+0.026	+0.032
Smoothed K factor	$\Delta\mathcal{A}$	+0.004	+0.013	+0.014	−0.016	−0.004	−0.001	+0.003	+0.028	+0.031	−0.020	−0.005	−0.012	−0.005
	$\Delta\sigma$	+0.001	+0.002	+0.004	+0.006	+0.008	+0.010	+0.012	+0.015	+0.018	+0.022	+0.025	+0.028	+0.034
Total syst.	σ^{sys}_{tot}	0.132	0.128	0.141	0.116	0.152	0.164	0.175	0.164	0.247	0.263	0.173	0.198	0.304
Total	σ_{tot}	0.191	0.203	0.226	0.237	0.280	0.314	0.359	0.398	0.479	0.526	0.552	0.627	0.725

Table 5.5: Systematic uncertainties on the amplitude. The shifts of both the measured amplitude, $\Delta\mathcal{A}$, and its statistical uncertainty, $\Delta\sigma$, are listed (cont'd)

Osc. frequency		14 ps^{-1}	15 ps^{-1}	16 ps^{-1}	17 ps^{-1}	18 ps^{-1}	19 ps^{-1}	20 ps^{-1}	21 ps^{-1}	22 ps^{-1}	23 ps^{-1}	24 ps^{-1}	25 ps^{-1}
$\mathcal{A}$		−0.828	−0.721	−0.405	−0.865	−1.185	−1.252	−1.777	−2.581	−2.634	−2.024	−1.774	−1.093
Stat. uncertainty		0.729	0.809	0.890	1.004	1.130	1.251	1.377	1.484	1.613	1.817	2.058	2.266
$PDG\ c\tau_{B_s}$	$\Delta\mathcal{A}$	−0.033	−0.025	+0.005	−0.004	−0.022	+0.007	−0.039	−0.094	−0.090	+0.001	−0.065	+0.011
	$\Delta\sigma$	+0.024	+0.028	+0.030	+0.036	+0.043	+0.047	+0.055	+0.059	+0.062	+0.070	+0.081	+0.087
Signal SF variation	$\Delta\mathcal{A}$	−0.019	−0.021	−0.030	−0.057	−0.072	−0.051	−0.063	−0.112	−0.164	−0.219	−0.273	−0.314
by 3.5%	$\Delta\sigma$	+0.026	+0.031	+0.036	+0.043	+0.052	+0.061	+0.071	+0.080	+0.091	+0.106	+0.124	+0.144
D^+_{Refl} fraction	$\Delta\mathcal{A}$	−0.012	−0.008	−0.001	+0.005	+0.018	+0.030	+0.024	+0.010	+0.018	+0.031	+0.046	+0.059
+ 1σ	$\Delta\sigma$	+0.011	+0.011	+0.012	+0.013	+0.016	+0.018	+0.019	+0.020	+0.021	+0.024	+0.027	+0.030
D^+_{Refl} fraction	$\Delta\mathcal{A}$	+0.035	+0.027	+0.002	−0.008	−0.033	−0.055	−0.027	+0.020	−0.007	−0.053	−0.091	−0.129
- 1σ	$\Delta\sigma$	−0.036	−0.039	−0.041	−0.047	−0.054	−0.061	−0.067	−0.070	−0.074	−0.083	−0.094	−0.105
D_s signal	$\Delta\mathcal{A}$	−0.014	−0.013	+0.002	−0.005	−0.013	−0.019	−0.046	−0.083	−0.073	−0.046	−0.035	−0.012
- 1σ	$\Delta\sigma$	+0.021	+0.023	+0.026	+0.030	+0.035	+0.039	+0.044	+0.047	+0.049	+0.054	+0.062	+0.067
Signal $c\bar{c}$ fraction changed	$\Delta\mathcal{A}$	−0.081	−0.074	−0.034	−0.098	−0.153	−0.168	−0.267	−0.424	−0.444	−0.355	−0.342	−0.213
to 6%	$\Delta\sigma$	+0.044	+0.051	+0.057	+0.071	+0.087	+0.101	+0.118	+0.133	+0.148	+0.176	+0.219	+0.245
$Br(D_sD_s) = 4.7\%$	$\Delta\mathcal{A}$	+0.009	+0.007	+0.004	+0.009	+0.012	+0.013	+0.020	+0.028	+0.029	+0.022	+0.019	+0.012
	$\Delta\sigma$	−0.008	−0.009	−0.010	−0.011	−0.012	−0.014	−0.015	−0.016	−0.017	−0.020	−0.022	−0.025
K-factor decreased	$\Delta\mathcal{A}$	+0.125	−0.151	−0.011	+0.201	+0.160	−0.017	+0.266	+0.158	+0.004	−0.508	−0.033	−0.547
by 2%	$\Delta\sigma$	−0.018	−0.023	−0.025	−0.036	−0.040	−0.043	−0.041	−0.038	−0.053	−0.095	−0.104	−0.081
Br($muDs$) = 5.5%	$\Delta\mathcal{A}$	−0.050	−0.055	−0.040	−0.070	−0.087	−0.092	−0.110	−0.164	−0.176	−0.148	−0.135	−0.137
	$\Delta\sigma$	+0.046	+0.050	+0.054	+0.060	+0.067	+0.075	+0.083	+0.088	+0.096	+0.109	+0.122	+0.134
Oscillated and Mixed fraction	$\Delta\mathcal{A}$	−0.011	−0.012	−0.011	−0.010	−0.007	−0.004	+0.000	+0.001	−0.006	−0.012	−0.013	−0.014
varied in bkg	$\Delta\sigma$	+0.000	+0.000	−0.000	−0.001	−0.001	−0.002	−0.002	−0.003	−0.002	−0.001	−0.001	−0.001
Br(μD_s) = 10.8%	$\Delta\mathcal{A}$	+0.029	+0.031	+0.022	+0.040	+0.049	+0.051	+0.062	+0.094	+0.101	+0.083	+0.074	+0.075
	$\Delta\sigma$	−0.026	−0.028	−0.031	−0.034	−0.038	−0.043	−0.047	−0.050	−0.055	−0.062	−0.069	−0.076
$Br(D_sD_s) = 23\%$	$\Delta\mathcal{A}$	−0.021	−0.018	−0.008	−0.021	−0.029	−0.032	−0.048	−0.070	−0.070	−0.054	−0.046	−0.028
	$\Delta\sigma$	+0.019	+0.021	+0.023	+0.027	+0.030	+0.033	+0.037	+0.039	+0.043	+0.048	+0.055	+0.060
K-factor increased	$\Delta\mathcal{A}$	−0.003	+0.412	−0.211	−0.235	−0.685	−0.352	−0.557	−0.126	+0.461	−0.023	+0.121	−0.344
by 2%	$\Delta\sigma$	+0.073	+0.085	+0.110	+0.119	+0.107	+0.143	+0.133	+0.143	+0.219	+0.235	+0.212	+0.226
Bkg SF chnaged	$\Delta\mathcal{A}$	−0.003	−0.004	−0.004	−0.004	−0.004	−0.004	−0.003	−0.001	−0.001	−0.003	−0.004	−0.007
to 2.0	$\Delta\sigma$	−0.001	−0.001	−0.001	−0.001	−0.001	−0.001	−0.002	−0.002	−0.003	−0.003	−0.003	−0.003
Bkg $c\bar{c}$ changed	$\Delta\mathcal{A}$	−0.038	−0.023	−0.012	−0.031	−0.041	−0.040	−0.061	−0.099	−0.108	−0.094	−0.104	−0.079
to 10.23%	$\Delta\sigma$	+0.007	+0.008	+0.010	+0.012	+0.015	+0.017	+0.019	+0.020	+0.022	+0.027	+0.033	+0.036
$P_T(\mu)$	$\Delta\mathcal{A}$	+0.042	+0.038	+0.027	+0.048	+0.070	+0.074	+0.084	+0.124	+0.135	+0.112	+0.103	+0.088
$>$ 6 GeV	$\Delta\sigma$	−0.035	−0.038	−0.042	−0.046	−0.052	−0.058	−0.064	−0.068	−0.074	−0.085	−0.095	−0.105
Generator level	$\Delta\mathcal{A}$	+0.085	−0.028	−0.160	+0.125	−0.132	−0.280	−0.144	+0.112	+0.086	−0.275	−0.095	−0.492
K factor	$\Delta\sigma$	+0.033	+0.037	+0.045	+0.050	+0.050	+0.056	+0.060	+0.074	+0.089	+0.087	+0.092	+0.096
Smoothed K factor	$\Delta\mathcal{A}$	+0.076	−0.018	−0.132	+0.064	−0.088	−0.279	−0.163	+0.099	−0.002	−0.252	−0.182	−0.634
	$\Delta\sigma$	+0.036	+0.040	+0.049	+0.054	+0.055	+0.061	+0.066	+0.079	+0.093	+0.097	+0.102	+0.106
Total syst.	σ^{sys}_{tot}	0.335	0.644	0.181	0.341	0.520	0.359	0.413	0.524	1.054	0.820	0.526	0.981
Total	σ_{tot}	0.802	1.034	0.909	1.060	1.244	1.302	1.438	1.574	1.926	1.994	2.124	2.469

Chapter 6

Combination and Results

6.1 Introduction

Besides $D_s^- \to K^{*0}K^-$ channel there are other two channels used to search for the B_s^0 mixing oscillations. Therefore, we produced results on $\mathrm{B_s^0} - \mathrm{\bar{B}_s^0}$ oscillations using three $\mathrm{B_s^0}$ decay modes [60]:

- $B_s^0 \to D_s^- \mu^+ \nu X$, $D_s^- \to K^* K^-$ [51] (Fig. 6.1).
- $B_s^0 \to D_s^- \mu^+ \nu X$, $D_s^- \to \phi\pi^-$ [16] (Fig. 6.2).
- $B_s^0 \to D_s^- e^+ \nu X$, $D_s^- \to \phi\pi^-$ [61] (Fig. 6.3).

6.2 Combination

The program "combos" [62] developed at LEP to combine the results with statistical and systematic uncertainties with different correlations has been used to perform the combination of different decay modes. Figures 6.4, 6.5, 6.6 show combinations of $\mu\phi\pi$ and $\mu K^* K$; $\mu\phi\pi$ and $e\phi\pi$; and all three decay modes. Uncertainties in the following parameters were considered as correlated:

- $Br(B_s \to X\mu D_s)$.

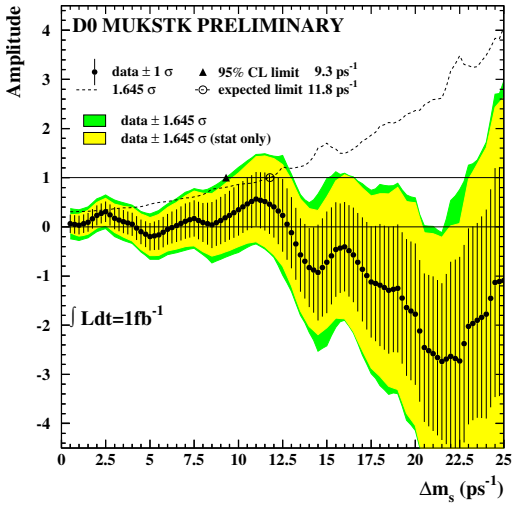

Figure 6.1: B_s^0 oscillation amplitude with statistical and systematic errors for $B_s^0 \to D_s^- \mu^+ \nu X$, $(D_s^- \to K^* K^-)$ decay mode.

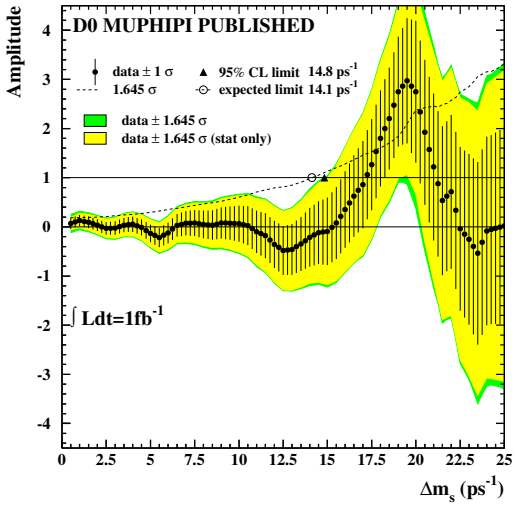

Figure 6.2: B_s^0 oscillation amplitude with statistical and systematic errors for $B_s^0 \to D_s^- \mu^+ \nu X$, $(D_s^- \to \phi \pi^-)$ decay mode.

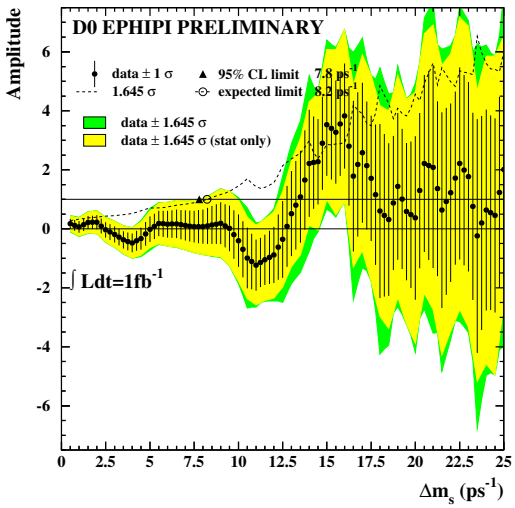

Figure 6.3: B_s^0 oscillation amplitude with statistical and systematic errors for $B_s^0 \to D_s^- e^+ \nu X$, $(D_s^- \to \phi \pi^-)$ decay mode.

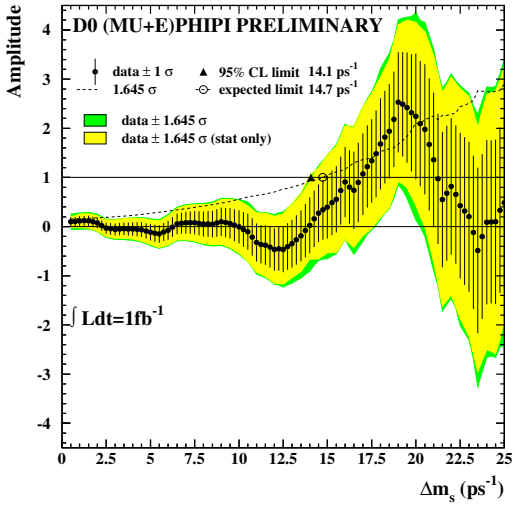

Figure 6.4: B_s^0 oscillation amplitude with statistical and systematic errors for $B_s^0 \to D_s^- e^+ \nu X$ and $B_s^0 \to D_s^- \mu^+ \nu X$ $(D_s^- \to \phi \pi^-)$ decay modes.

- $Br(B_s \to X D_s D_s)$.

- Signal decay length resolution for $\mu \phi \pi$ and $\mu K^* K$ decay modes.

- $\Delta\Gamma/\Gamma$.

Although some degree of correlation is expected between the systematic uncertainty due to dilution uncertainty of the different channels, the way this systematic is currently assessed makes it difficult to quantify the correlation. Tests including or excluding this systematic uncertainty in individual channels indicate that ignoring this one correlation leads to negligible differences in the combined results.

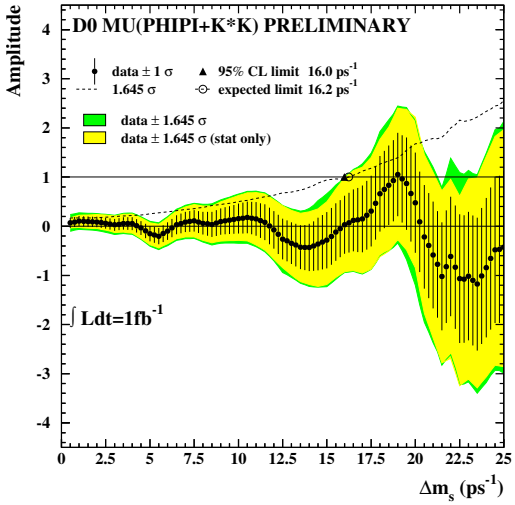

Figure 6.5: B_s^0 oscillation amplitude with statistical and systematic errors for $B_s^0 \to D_s^- \mu^+ \nu X$ ($D_s^- \to \phi\pi^-$ and $D_s^- \to K^*K^-$) decay modes.

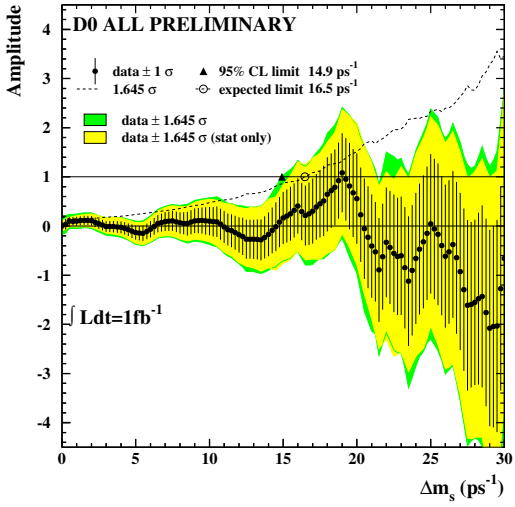

Figure 6.6: B_s^0 oscillation amplitude with statistical and systematic errors for $B_s^0 \to D_s^- e^+ \nu X$ ($D_s^- \to \phi\pi^-$) and $B_s^0 \to D_s^- \mu^+ \nu X$ ($D_s^- \to \phi\pi^-$ and $D_s^- \to K^*K^-$) decay modes.

6.3 Log Likelihood Scan

An amplitude scan can be transformed to a log likelihood scan using the following formula [20, 63]:

$$-\Delta \log(L) = \left(\frac{1}{2} \left(\frac{1 - \bar{\mathcal{A}}}{\sigma_{\mathcal{A}}} \right)^2 - \frac{1}{2} \left(\frac{\bar{\mathcal{A}}}{\sigma_{\mathcal{A}}} \right)^2 \right) \tag{6.1}$$

This formula can be tested using the $B_s^0 \to D_s^- \mu^+ \nu X$, $D_s^- \to \phi\pi^-$ decay mode where the log likelihood scan was obtained directly from the fitting procedure. Figures 6.7

and 6.8 show the log likelihood scans obtained in two different ways.

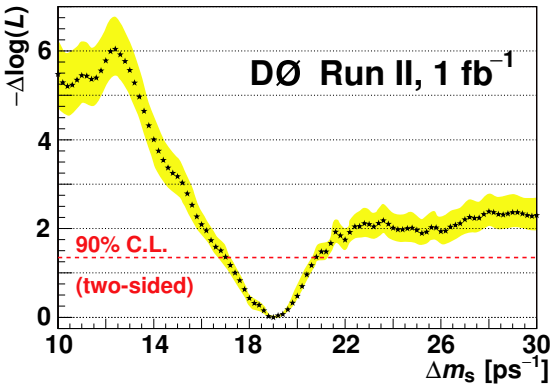

Figure 6.7: Log likelihood scan for $B_s^0 \to D_s^- \mu^+ \nu X$ $(D_s^- \to \phi\pi^-)$ decay mode obtained from the fitting procedure.

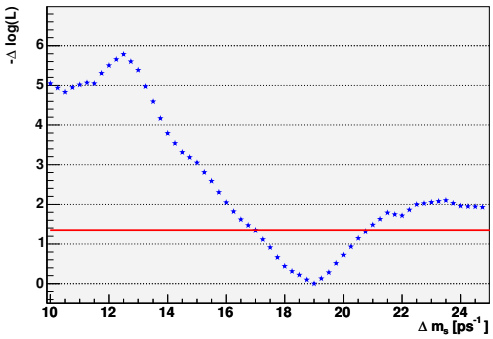

Figure 6.8: Log likelihood scan for $B_s^0 \to D_s^- \mu^+ \nu X$ $(D_s^- \to \phi\pi^-)$ decay mode obtained from the amplitude scan using the total errors (stat. $\bigoplus$ syst.).

A log likelihood scan obtained from the combined amplitude scan (Fig. 6.6) is shown in Fig. 6.9. The combined likelihood curve has a preferred value of the oscillation frequency $\Delta m_s = 19$ ps^{-1}, with a 90% confidence level interval of $17 < \Delta m_s < 21$ ps^{-1}, assuming Gaussian uncertainties.

In the previous analysis [16], the probability of a background fluctuation to give a minimum of equal or greater depth in this interval was determined to be 5% using ensemble tests. Comparing the change in likelihood at $\Delta m_s = 19$ ps^{-1} and the likelihood at $\Delta m_s = \infty$ [63] also yields a 5% expectation for a background fluctuation. For the current combined result, comparison of the change in likelihood between $\Delta m_s = 19$ ps^{-1} and $\Delta m_s = \infty$ yields an 8% expectation for a background fluctuation.

6.4 Conclusion

The combined amplitude scan allows the setting of a 95% C.L. limit on the $B_s^0 - \bar{B}_s^0$ oscillation frequency $\Delta m_s > 14.9$ ps^{-1} with the corresponding expected limit at 16.5 ps^{-1}. The combined likelihood curve has a preferred value of $\Delta m_s = 19$ ps^{-1},

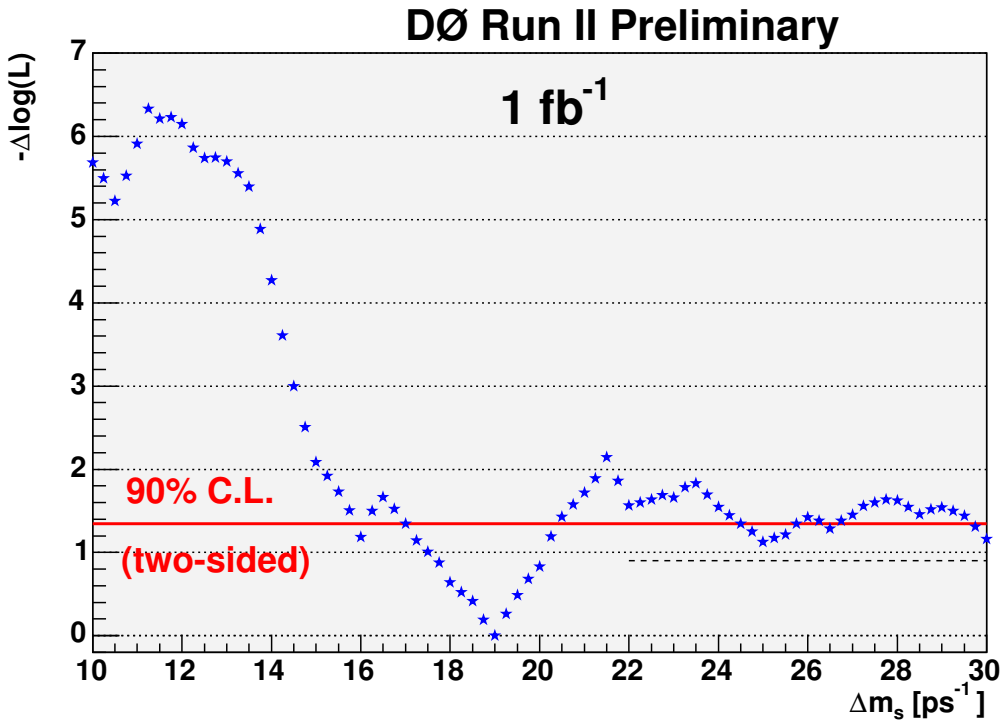

Figure 6.9: Log likelihood scan obtained from the combined amplitude scan using the total errors. The horizontal solid line indicates the 90% C.L. (two-sided) log likelihood difference. The horizontal dashed line indicates the value of $\Delta \log \mathcal{L}$ at $\Delta m_s = \infty$.

with a 90% confidence level interval of $17 < \Delta m_s < 21$ ps^{-1}, assuming Gaussian uncertainties. The probability for a background fluctuation to give a similar dip in the same interval is estimated to be approximately 8%. The effect of these results on CKM fit can be seen in Fig. 6.10.

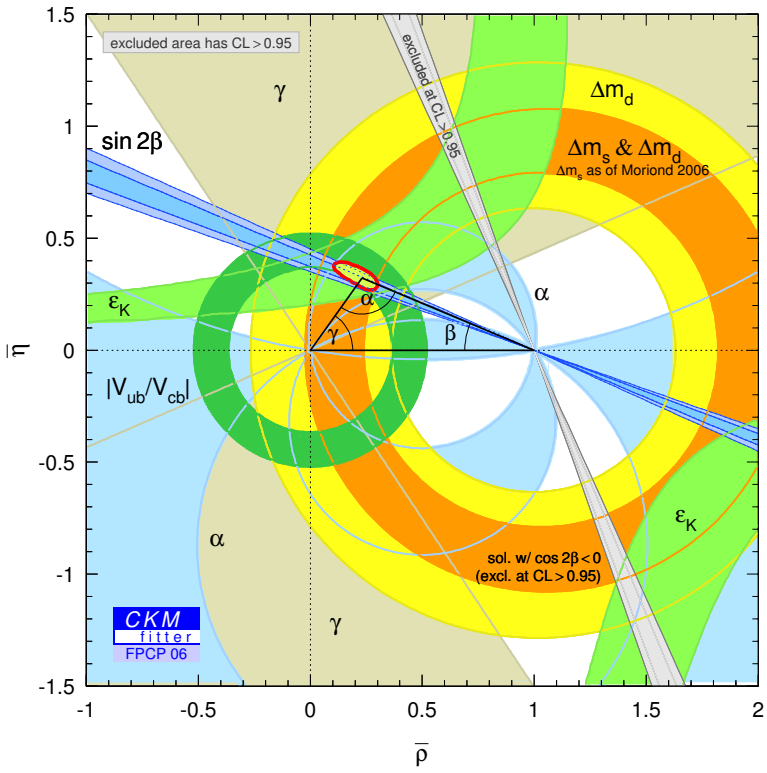

Figure 6.10: The effect on CKM triangle. The reduced uncertainty in the band due to Δm_s and Δm_d can be seen in this fit.

Bibliography

[1] S. Eidelman *et al.*, Phys. Lett. **B592**, 1 (2004).

[2] S.L. Glashow, Murray Gell-Mann, Gauge theories of Vector Particles, Annals Phys. **15** 437-460, (1961).

[3] Gauge theories of elementary interactions, A. Salam and J.C. ward, Phys. Rev. **136**, B763-768 (1964).

[4] A. Eienstein, The foundation of the General Theory of Relativity, Annalen Phys. **14**, 517-571 (1905); Annalen Phys. **49**, 769-822 (1916).

[5] Observation of a Dimuon Resonance at 9.5 GeV in 400-GeV Proton-Nucleus Collisions, S.W. Herb, *et al.*, Phys. Rev. Lett. **39**, 252-255 (1977).

[6] K. Lande, *et al.*, Phys. Rev. **103** 1901 (1956).

[7] M. Gell-Mann, A. Pais, Phys. Rev. **97**, 1387 (1955).

[8] N.Cabibbo, Phys. Rev. Lett. **10**, 531 (1963).

[9] S.L. Glashow, J. Iliopoulos, and L. Maiani, Phys. Rev. **D2** 1585 (1970).

[10] M. Kobayashi and T. Maskawa, Progr. Theor. Phys. **49** 652 (1973).

[11] L.L. Chau and W.Y. Keung, Phys. Rev. Lett. **53** 1802 (1984).

[12] L. Wolfenstein, Phys. Rev. Lett. **51** 1945 (1983).

[13] R.M. Barnett *et al.*, Review of Particle Properties, Phys. Rev. **D54** 1 (1996).

[14] C. Albajar, *et al.*, (UA1 Collaboration) Phys. Lett. **B187**, 247 (1987).

[15] H. Albrecht, *et al.*, (ARGUS Collaboration) Phys. Lett. **B192**, 245 (1987)

[16] V. Abazov, *et al*, Phys.Rev.Lett. **97** 021802 (2006).

[17] [CDF Collaboration] Measurement of B_s^0- Anti-B_s^0 Oscillation Frequency, Submitted in Physical Review Letters, arXiv:hep-ex/0606027.

[18] M. Beneke, G. Buchalla, I. Dunietz, Phys. Rev. **D54** 4419 (1996).

[19] I. Stewart, QCD effects in Weak Decays, Plenary talk at the 22nd International Symposium on Lepton-Photon Interactions at High Energy (LP 2005), Uppsala, Sweden (2005).

[20] H.-G. Moser and A. Roussarie,*Nucl. Instrum. Methods* A **384**, 1997 (491).

[21] DØ Collaboration, "Observation of the Top Quark", *Phys. Rev. Lett.* **74**, 2632 (1995).

[22] C. W. Schmidt, *The Fermilab 400 − MeV Linac upgrade*, FERMILAB-CONF-93-111 (1993).

[23] Fermilab Beams Division, *Run II Handbook*, http://www-bd.fnal.gov/runII/index.html

[24] J. Marriner, *stochastic Cooling Overview*, FERMILAB-CONF-03-158 (2003).

[25] G.L. Budkar, *Atomnaya Energiya*, **22**, 346-8 (1996).

[26] DØ Collaboration, The upgraded DØ detector, *Accepted in NIM*.

[27] R. Ruchti, Ann. Rev. Nucl. Part. Sci. **46** (1996) 281.

[28] P. Baringer, *et al.*, *Nucl. Instrum. Methods* A **469**, 2001 (295)

[29] S. Abachi et al., *The DØ Collaboration* : *The DØ detector* , *Nucl. Instrum. Methods* A **338**, 1994 (185).

[30] Md. Naimuddin, *et al.*, *DØ Note 4713*, B-Flavor Tagging with Soft electrons.

[31] Md. Naimuddin, *et al.*, *DØ Note 4848*, B-Flavor Tagging with Soft electrons.

[32] Reconstruction of B Hadron Signals at *DØ*, Guennadi Borissov, Sergey Burdin, Eduard de la Cruz-Burelo, Vivek Jain, Andrei Nomerotski, Pedro Podesta-Lerma, Rick Van Kooten, June 24 2004.

[33] http://www-d0.fnal.gov/Run2Physics/ckm/d0_private/computing/new_data_files_onDISK.htr

[34] http://www-d0.fnal.gov/Run2Physics/ckm/d0_private/computing/mc_files.html

[35] Z. Ligetti "Introduction to heavy meson decays and CP asymmetries", hep-ph/0302031.

[36] E. Berger *et al.,* Phys. Rev. Lett. **86**, 4231 (2001).

[37] DØ Collaboration, "Flavor oscillations in B_d^0 mesons with opposite-side muon tags". D0 Note 4370, Mar, 2004.

[38] S. Abachi *et al.*,NIMA **338**, 1994 (185).

[39] S. Catani *et al.*, Phys. Lett. **B269** (1991) 432.

[40] F. Beaudette and J.-F. Grivaz, "The Road Method (an algorithm for the identification of electrons in jets)", DØ Note 3976, Nov 4 2002.

[41] Reconstruction of B hadron signals at D0: http://www-d0.fnal.gov/Run2Physics/WWW/results/prelim/B/B00/B00.pdf.

[42] DELPHI Collab., b$-$*tagging in DELPHI at LEP*, Eur. Phys. J. **C32** (2004), 185-208.

[43] P. Abreu *et al.*, DELPHI Collaboration, Phys. Lett. B **475**, 407 (2000).

[44] DELPHI Collab., Euro. Phys. J. **C35**, 35 (2004).

[45] D. Scora and N. Isgur, Phys. Rev. D **52**, 2783 (1995).

[46] M. Neubert, Phys. Rep. **245**, 259 (1994).

[47] G. Borrisov, *et al.*, *DØ Note 4828*, B_d Mixing measurement using semileptonic sample and combined opposite side tagging.

[48] C. Ay, *et al.*, *DØ Note 5029*, B_d mixing measurement using Opposite-side Flavor Tagging.

[49] Heavy Flavor Averaging Group, *http://www.slac.stanford.edu/xorg/hfag/index.html*

[50] CKM Fitter Group, *http* : *//www.slac.stanford.edu/xorg/ckmfitter/ckm_welcome.html*

[51] B. Abbott *et al.*, *DØ Note 5149*, B_s^0 mixing studies in Semileptonic B_s^0 decays with $D_s^- \to K^{*0}K^-$ and Unibinned fit.

[52] B. Abbott *et al.*, *DØ Note 5172*, B_s^0 mixing studies in Semileptonic B_s^0 decays with $D_s^- \to K^{*0}K^-$ and Unibinned fit.

[53] S. Catani, Yu.L. Dokshitzer, M. Olsson, G. Turnock, B.R. Webber, Phys. Lett. **B269** (1991) 432.

[54] *http://www-d0.fnal.gov/computing/algorithms/muon/muon_algo.html*.

[55] B. Abbott *et al.*, *DØ Note 4842*, B_s mixing in semileptonic Bs decays using Ds to Phi Pi decay mode.

[56] M. Anzelc *et al.*, *DØ Note 5017*, B_s mixing in semileptonic Bs decays using Ds to Phi Pi decay mode.

[57] G. Borissov *et al., DØ Note 4991*, Bd mixing measurement using Opposite-side Flavor Tagging.

[58] T. Sjöstrand *et al.,* arXiv:hep-ph/0108264.

[59] D.J. Lange,*Nucl. Instrum. Methods* A **462**, 2001 (152); for details see *http://www.slac.stanford.edu/˜ lange/EvtGen*.

[60] G. Borrisov *et al.*, *D0Note 4701*, A combination of B_s^0 Oscillations Results from DØ.

[61] The DØ Collaboration, *DØ Note 5174*, "B_s mixing in $B_s \to D_s e\nu X$, $D_s \to \phi\pi$ decay mode"

[62] http://lepbosc.web.cern.ch/LEPBOSC/combos/.

[63] D. Abbaneo, G. Boix, JHEP **08** (1999) 004.